

Self-affine time series: applications and models

Jon D. Pelletier and Donald L. Turcotte

Department of Geological Sciences, Snee Hall, Cornell University

Ithaca, NY 14853

Table of Contents

1. Introduction
2. Natural variability of climate
 - 2.1. Temperature spectra
 - 2.2. River discharge and tree ring spectra
 - 2.3. Stochastic diffusion model
 - 2.4. Variations in solar luminosity
 - 2.5. Drought hazard assessment
3. Variations in sedimentation
 - 3.1. Introduction
 - 3.2. Surface growth model
 - 3.3. Observations
 - 3.4. Completeness of the sedimentary record
 - 3.5. Bed thicknesses
4. Variability of the earth's magnetic field
 - 4.1. Variations of the dipole moment
 - 4.2. Reversal record
 - 4.3. Inclination and declination data
 - 4.4. Model for geomagnetic variations
5. Other applications

I. INTRODUCTION

In the previous paper [*Malamud and Turcotte, 1997*, hereafter referred to as MT] the authors considered various theoretical aspects of self-affine time series. Several techniques for generating synthetic, self-affine time series were discussed and alternative methods for analyzing time series were presented. A primary means of identifying a self-affine time series is in terms of its Fourier spectrum. For self-affinity the power spectrum or power-spectral density, S , must have a power-law dependence on frequency, f : $S \propto f^{-\beta}$ (MT equation 2.4).

When considering self-similar processes in nature there are generally upper and lower limits to the validity of power-law statistics. An example is a power-law distribution for the frequency-size distribution of fragments. There will always be a largest and a smallest fragment. In many cases power-law statistics will be applicable over a limited range of sizes. In other cases two power-law regimes are found with different slopes. There are also upper and lower limits to the self-affine behavior of naturally occurring time series. In some cases two or more power-law regimes are found with different values of β . In this paper we consider several applications of self-affine time series in geophysics. The coverage of topics is not meant to be complete. Instead, we consider three examples in some detail and present applicable models.

The first application we consider is time-series data for local atmospheric temperature. The spectral behavior for time scales between 200 kyr and 500 yr is obtained from Deuterium concentrations in the Vostok ice core. Historical temperature records are analyzed to give the spectral behavior between time scales of 100 yr and 1 day. The obvious daily and annual periodicities are removed and we focus on the stochastic content of the time series. We find that self-affine behavior is applicable over well-defined frequency bands. The self-affine behavior is associated with interactions between the atmosphere, the space above (through the radiation of heat), and the oceans and continents below. Solutions to a stochastic diffusion equation for a layer with a substrate reproduce the observed statistics. The results are virtually identical to those for heat diffusion through a metallic film over a substrate and

to variations of solar luminosity. We have also carried out power-spectral analyses of mean river discharges and tree ring thicknesses. Both exhibit self-affine behavior with $\beta \approx 0.5$. This corresponds to a Hurst exponent $Hu \approx 0.7$, consistent with the previous results as discussed by MT (Section 5.2). The implications of a self-affine river discharge time series for drought assessment is also considered.

In our second application we consider porosity variations in sedimentary basins. A model developed for the growth of atomic surface layers is modified so that it is applicable to the spatial and temporal variations in deposition and erosion. Self-affine variability is found with $\beta = 2$ in space and $\beta = 1.5$ in time. The spatial variability is a Brownian walk. This has been widely observed as the spectral behavior of topography. We show that this variability is also consistent with the spatial distribution of oil pools in sedimentary basins. The temporal variability of sedimentation is associated with the vertical variability of porosity. Self-affine spectra with $\beta \approx 1.5$ are good approximations to observed data. The vertical variability of sedimentation and erosion can also be used to model the completeness of the sedimentary record. It has been observed that the rate of sedimentation, R , has a power-law dependence on the time period of sedimentation, T , with $R \propto T^{-0.76}$. A self-affine spectrum with $\beta = 1.5$ gives $R \propto T^{-0.75}$.

Our third application considers the variability of the earth's magnetic field. We argue that intensity variations and reversals of the magnetic field are a natural consequence of the inherent variability generated by dynamo action and magnetic diffusion in the core. The field exhibits a binormal behavior and when a fluctuation crosses the zero intensity value a reversal occurs. The spectral behavior of the field on time scales of 100 yr to 4 Myr has been obtained from paleomagnetic data. Over this range it is well approximated by a $1/f$ ($\beta = 1$) self-affine time series. Synthetic $1/f$ time series have been used to generate reversal statistics and these are found to be in good agreement with observations. The reversal statistics are sensitive to the values of β and we conclude that the agreement is strong support for $1/f$ behavior over the entire record of reversals. A model that generates the observed $1/f$ behavior is a two-dimensional stochastic diffusion equation.

II. NATURAL VARIABILITY OF CLIMATE

A. Temperature spectra

Understanding the natural variability of climate is one of the most important tasks facing climatologists. The *Intergovernmental Panel on Climate Change* [1995] concluded that the “balance of evidence suggests a discernible human impact on the climate system.” This conclusion is based, however, on comparisons with the variability exhibited by general circulation models (GCM). Model runs often exhibit significantly lower variability, by a factor of two to five, and a different frequency dependence on time than paleoclimatic data [*Intergovernmental Panel on Climate Change*, 1995]. Other model results give natural variability comparable in magnitude to that observed in the last 100 years [*Barnett, et al.* 1992].

In this section we consider the power spectrum of temporal variations in atmospheric temperature on time scales of 200 kyr to 1 day. We will show that at frequencies smaller than $f \approx 1/(40 \text{ kyr})$ the power spectrum is flat (white noise). At frequencies between $f \approx 1/(40 \text{ kyr})$ and $f \approx 1/(2 \text{ kyr})$ the power spectrum is proportional to f^{-2} (a Brownian walk). At frequencies greater than $f \approx 1/(2 \text{ kyr})$ the power spectrum is proportional to $f^{-\frac{1}{2}}$. At very high frequencies (above $f \approx 1/(1 \text{ month})$) the spectrum varies as $f^{-\frac{3}{2}}$ for continental stations and remains proportional to $f^{-\frac{1}{2}}$ for maritime stations. Thus we find a sequence of self-affine spectra, each with a characteristic values of β , over different frequency bands.

We will further show that the observed power spectrum of atmospheric temperature is identical to the power spectrum of variations due to the stochastic diffusion of heat in a metallic film that is in thermal equilibrium with a substrate [*Van Vliet et al.*, 1980]. Temperature variations in the film and substrate occur as a result of fluctuations in the heat transport by electrons undergoing Brownian motion. The top of the film absorbs and emits blackbody radiation. In our analogy we associate the atmosphere with the metallic film and the oceans with the substrate. Turbulent eddies in the atmosphere and oceans are analagous to the electrons undergoing Brownian motion in a metallic film in contact with a

substrate.

We first consider the spectral behavior of the Deuterium concentrations in the Vostok (East Antarctica) ice core. A 220 kyr record of temperature fluctuations is obtained using the conversion $5.6 \delta D(\%) = 1^\circ\text{K}$ [Jouzel *et al.*, 1987]. The plot of variations in temperature versus age is given in Figure 2.1. Jouzel and Merlivat [1983] have concluded that the Vostok Deuterium record is a proxy for local atmospheric temperature. Because the data are unevenly sampled we utilized the Lomb Periodogram [Press *et al.*, 1992] to estimate the power spectrum. The results are given in Figure 2.2. We associate the power spectrum with three regions of different self-affine behavior. The first region, at frequencies less than $f \approx 1/(40 \text{ kyr})$, is a white noise ($\beta \approx 0$). The second region, between $f \approx 1/(40 \text{ kyr})$ and $f \approx 1/(2 \text{ kyr})$ is a Brownian walk ($\beta \approx 2$). In the third region, with frequencies greater than $f \approx 1/(2 \text{ kyr})$, there is a change to a lower value of β . This change is associated with rapid variations in the Vostok core. This is also observed in ice cores from Greenland [Yiou *et al.*, 1995]. Details of this analysis have been given by Pelletier [1997a].

In order to extend our analyses to higher frequencies we have carried out power-spectral analyses on data for atmospheric temperature variations from weather stations. One of the longest available records is for the average monthly temperature in Central England, 1659-1973. The data is tabulated in Manley [1974]. The yearly periodicity was removed from this data by subtracting from each value the average temperature of that month for the entire record. The resulting time series is given in Figure 2.3. The time series exhibits rapid fluctuations from year to year superimposed on more gradual, lower frequency variations. The power spectrum estimated as the square of the coefficients of the Fast Fourier Transform (FFT) is presented in Figure 2.4 along with a least-square power-law fit to the data with $\beta = -0.47$. We have also determined the average power spectrum of the time series of monthly mean temperatures from 94 stations worldwide with the yearly trend removed. We obtained the power spectra $S(f)$ of all complete temperature series of length greater than or equal to 1024 months from the climatological database compiled by Vose *et al.* [1992]. The yearly trend was removed by subtracting from each monthly data point the average temperature

for that month in the 86 year record for each station. All of the power spectra were then averaged at equal frequency values. The results are given in Figure 2.5. The data yield a straight-line on a log-log plot with slope close to -0.5 indicating that $S(f) \propto f^{-\frac{1}{2}}$ in this frequency range.

Finally we consider the average power spectrum of time series of daily mean temperature (estimated by taking the average of the maximum and minimum temperature of each day) from 50 continental and 50 maritime stations over 4096 days. Maritime stations are sites on small islands far from any large land masses. Continental stations are well inland on large continents, far from any large bodies of water. We chose 50 stations at random from the complete records (those with greater than 4096 nearly consecutive days of data) provided by the Global Daily Summary database compiled by the *National Climatic Data Center* [1994]. Once again the yearly periodicities were removed. The results are given in Figure 2.6 and 2.7. Continental stations (Figure 2.6) correlate with a $f^{-\frac{3}{2}}$ high-frequency region. Maritime stations (Figure 2.7) correlate with a $f^{-\frac{1}{2}}$ scaling up to the highest frequency. The crossover frequency for the continental spectra is $f \approx 1/(1 \text{ month})$. The difference between continental and maritime stations results from the air mass above maritime stations exchanging heat with both the atmosphere above and the oceans below while the air mass above continental stations exchanges heat only with the atmosphere above it. The three spectra have been combined in Figure 2.8 to give a continuous spectral behavior of local atmospheric temperature from frequencies of 10^{-6} - 10^2 yr^{-1} .

B. River discharge and tree ring spectra

Before presenting a theoretical basis for the temperature time series spectra given above we will consider two related time series. We first give power-spectral analyses of hydrological time series. Figure 2.9 presents the results of power-spectral analyses of monthly mean river discharge data in the United States from the Hydro-Climatic Data Network compiled by *Slack and Landwehr* [1994]. The annual variabilities were removed and the power spectra

were computed in the same manner as for the temperature data. For the streamflow data we chose all complete records with a duration greater than or equal to 512 months and included 636 records in our analysis. Since river discharges can vary by orders of magnitude between river basins we normalized the variance of each series before averaging the spectra. A least-square fit to the data a β value of -0.50, consistent with the value observed for the temperature data in the same frequency range. We have taken advantage of the large number of available stations to investigate the possible regional variability of the power spectra. We have averaged the power spectra for each of the 18 hydrologic regions of the U.S. defined by the United States Geological Survey and given in *Wallis et al.* [1991]. All of the regions exhibit the same spectral dependence with an average β value of -0.52 and a standard deviation of 0.03, indicating little variation.

The second related time series we consider is the sequence of annual tree ring widths. We have performed spectral analyses of tree ring width chronologies in the western United States obtained from the International Tree Ring Database. Tree rings in the western U.S. are strongly correlated with precipitation [*Landwehr and Matalas, 1986*]. The chronologies are time series in which the nonstationarities in growth rates have been removed and spatial averaging has been performed in an attempt to isolate climatic effects. Tree ring series have the advantage of being much longer than most historical records. We obtained 43 chronologies in the western U.S. greater than 1024 years in length. The average normalized power spectrum of those records is presented in Figure 2.10. The least-square fit indicates that for tree ring time series, $S(f)$ is nearly proportional to $f^{-\frac{1}{2}}$.

In the frequency range $f \approx 1/(2 \text{ kyr})$ to $1/(1 \text{ month})$ the three data sets atmospheric temperature, river discharge, and tree ring widths all yield spectra with a slope $\beta \approx 1/2$. In Section 5.2 of MT the application of the rescaled-range technique was discussed. It was pointed out that *Hurst et al.* [1965] applied the rescaled-range method to time-series data for atmospheric temperature, river discharge, precipitation, tree ring widths, and other climatological time series. Good correlations were obtained with the Hurst relation (MT equation 5.5) taking $H_u=0.73$ on average. From the correlation between H_u and β given for

fractional Gaussian noises in MT Figure 5.3 we see that $Hu=0.73$ is entirely consistent with the observed value $\beta \approx 1/2$.

C. Stochastic diffusion model

To see how time series with power-law power spectra arise, we present the results from the simulation of a discrete, one-dimensional stochastic diffusion process. A discrete version of the diffusion equation for the density of particles on a one-dimensional grid of points is

$$n_i(t_{j+1}) - n_i(t_j) \propto n_{i+1}(t_j) - 2n_i(t_j) + n_{i-1}(t_j) \quad (1)$$

We establish a one-dimensional lattice of 32 sites with periodic boundary conditions at the ends of the lattice. At the beginning, we place 10 particles on each site of the lattice. At each timestep, a particle is chosen at random and moved to the left with probability $\frac{1}{2}$ and to the right if it does not move to the left. In this way, the average rate at which particles leave a site is proportional to the number of particles in the site. The average rate at which particles enter a site i is proportional to the number of particles on each side multiplied by one-half since the particles to the left and right of site i move into site i only half of the time. This is a stochastic model satisfying equation 2.1. The probabilistic nature of this model causes fluctuations to occur in the local density of random walkers. These fluctuations do not occur in a deterministic model of diffusion.

In Figure 2.7 we present the average of 50 power spectra, each spectrum from a time series of the number of particles in the central site of the 32-site lattice. The figure shows a power spectrum of the form $S(f) \propto f^{-\frac{1}{2}}$. In Figure 2.8 we plot the cumulative probability distribution of the time series produced by the stochastic diffusion model. The solid circles represent data. The curve represents the cumulative log-normal distribution fit to the data. A good fit is obtained.

Since the distribution of values in a hydrological time series is often log-normal, we have shown that a simple model of stochastic diffusion gives rise to both the power spectrum and the distribution observed for hydrological time series.

A stochastic diffusion process can be studied analytically by adding a noise term to the flux of a deterministic diffusion equation [*Van Kampen*, 1981]:

$$\rho c \frac{\partial \Delta T}{\partial t} = -\frac{\partial J}{\partial x} \quad (2)$$

$$J = -\sigma \frac{\partial \Delta T}{\partial x} + \eta(x, t) \quad (3)$$

where J is the heat flux, ΔT is the fluctuation in temperature from equilibrium, ρ is the density, c is the heat capacity per unit mass, σ is the conductivity, and η is Gaussian random noise in space and time.

Equation 2.2 is conservation of energy. Equation 2.3 is Fourier's law of heat transport with random advection of heat superimposed. The random advection term models the effects of local convective instabilities which randomly advect heat vertically in the atmosphere. *Novikov* [1963] has proposed this method for studying turbulent fluctuations.

We now determine the behavior of the stochastic diffusion model in terms of the power spectrum of temperature fluctuations in a layer of width $2l$ of an infinite, one-dimensional, homogeneous space. The presentation we give is similar to that of *Voss and Clarke* [1976]. The variations in total heat energy in the layer of width $2l$ is determined by the heat flow across the boundaries. Figure 2.9a illustrates the geometry of the layer exchanging thermal energy with diffusing regions above and below it. A diffusion process has a frequency-dependent correlation length $\lambda = (2D/f)^{1/2}$ [*Voss and Clarke*, 1976]. Two different situations arise as a consequence of the length scale, $2l$, of the geometry. For high frequencies $\lambda \ll 2l$ and the fluctuations in heat flow across the two boundaries are independent. For low frequencies $\lambda \gg 2l$ and the fluctuations in heat across the two boundaries are in phase.

First we consider high frequencies. Since the boundaries fluctuate independently, we can consider the flow across one boundary only. The flux of heat energy is given by equation 2.2. Its Fourier transform is given by

$$J(k, \omega) = \frac{i\omega\eta(k, \omega)}{\alpha k^2 + i\omega} \quad (4)$$

where $\alpha = \sigma/(\rho c)$ is the diffusivity. The flux of heat energy out of the layer at the boundary at $x = l$ (the other boundary is located at $x = -l$) is the rate of change of the total energy in the layer $E(t)$: $\frac{dE(t)}{dt} = J(l, t)$. The Fourier transform of this equation is

$$E(\omega) = -\frac{i}{(2\pi)^{\frac{1}{2}}\omega} \int_{-\infty}^{\infty} dk e^{ikl} J(k, \omega) \quad (5)$$

Therefore, the power spectrum of variations in $E(t)$, $S_E(\omega) = \langle |E(\omega)|^2 \rangle$, is

$$S_E(\omega) \propto \int_{-\infty}^{\infty} \frac{dk}{\alpha^2 k^4 + \omega^2} \propto \omega^{-\frac{3}{2}} \quad (6)$$

In the above expression, the noise term η does not appear because, since it is white noise in space and time, it's average amplitude is independent of ω and k , i.e. it is just a constant. Since $\Delta T \propto \Delta E$ the power spectrum of temperature has the same form as S_E and $S_T(\omega) \propto \omega^{-\frac{3}{2}}$.

If we include the heat flux out of both boundaries, the rate of change of energy in the layer will be given by the difference in heat flux: $\frac{dE(t)}{dt} = J(l, t) - J(-l, t)$. The Fourier transform of $E(t)$ is now

$$E(\omega) = \frac{1}{(2\pi)^{\frac{1}{2}}\omega} \int_{-\infty}^{\infty} dk \sin(kl) J(k, \omega) \quad (7)$$

Then,

$$\begin{aligned} S_T(\omega) \propto S_E(\omega) &\propto \int_{-\infty}^{\infty} \frac{dk \sin^2(kl)}{\alpha^2 k^4 + \omega^2} \\ &\propto \omega^{-\frac{3}{2}} (1 - e^{-\theta} (\sin \theta + \cos \theta)) \end{aligned} \quad (8)$$

where $\theta = (\omega/\omega_o)^{\frac{1}{2}}$ and $\omega_o = \alpha/2l^2$ is the frequency where the correlation length is equal to the width of the layer. When $\lambda \ll 2l$, the above expression reduces to $S_T(f) \propto f^{-\frac{3}{2}}$. When $\lambda \gg 2l$, $S_T(f) \propto f^{-\frac{1}{2}}$ [Voss and Clarke, 1976]. In this limit the boundaries fluctuate in phase and heat that enters into the region from one boundary can diffuse out of the other boundary. The result is a sequence of fluctuations which are less persistent (β is smaller) than the single boundary $f^{-\frac{3}{2}}$ case.

In Section 2.1 we presented evidence that continental stations exhibit a $f^{-\frac{3}{2}}$ high-frequency region and maritime stations exhibit $f^{-\frac{1}{2}}$ scaling up to the highest frequency

considered. This observation can be interpreted in terms of the diffusion model presented above. The power spectrum of temperature variations in an air mass exchanging heat by one-dimensional stochastic diffusion is proportional to $f^{-\frac{1}{2}}$ if the air mass is bounded by two diffusing regions and is proportional to $f^{-\frac{3}{2}}$ if it interacts with only one. The boundary conditions appropriate to maritime and continental stations are presented in Figure 2.13b and 2.13c, respectively. The maritime stations have a $f^{-\frac{1}{2}}$ power spectrum up to the highest frequency because the air mass above a maritime station exchanges heat with both the atmosphere above and the oceans below. In maritime stations, fluctuations in heat energy are readily absorbed by both the oceans below and the atmosphere above which can radiate heat into space. The fluctuation calculation appropriate for maritime stations is one in which the coherent fluctuations from two boundaries are considered as in the calculation of the $f^{-\frac{1}{2}}$ spectrum. The air mass above continental stations exchanges heat energy only with the atmosphere above it. The calculation appropriate for continental stations is the one-boundary model which predicts the observed $f^{-\frac{3}{2}}$ spectrum. At low frequencies, horizontal heat exchange between continental and maritime air masses limits the variance of the continental stations. This crossover should occur at the time scale when the air masses above continents and oceans become mixed. The time scale for one complete Hadley or Walker circulation which mixes the air masses is approximately 1 month, the same time scale as the observed crossover [Pelletier, 1997a].

Next we consider the stochastic diffusion model in a geometry appropriate for a coupled atmosphere-ocean model with an atmosphere of uniform density (equal to the density at sea level) in thermal contact with oceans of uniform density. The height of our model atmosphere is the scale height of the atmosphere (height at which the pressure falls by a factor of e from its value at sea level). Figure 2.14 illustrates the geometry and constants chosen with σ the vertical heat conductivity, ρ the density, c the specific heat per unit mass, α the vertical thermal diffusivity, and g the thermal conductance of heat out of the Earth by emission of radiation. Primed constants denote values for the oceans. The physical constants which enter the model are the density, specific heat, vertical thermal diffusivity, depths of the

oceans and atmosphere, and the thermal conductance by emission of radiation. The density and specific heat of air and water are well-known constants. We chose an ocean depth of 4 km and an atmospheric height equal to the scale height of 8 km as used by *Hoffert et al.* [1980] in their climate modeling studies. The eddy diffusivity we employ for the oceans is $6 \times 10^{-5} \text{ m}^2/\text{s}$. This value has been obtained from Tritium dispersion studies [*Garrett, 1984*]. The vertical eddy diffusivity for the atmosphere we use is $1 \text{ m}^2/\text{s}$, as quoted by *Pleune* [1990] and *Seinfeld* [1986] for stable air conditions. This eddy diffusivity implies an equilibration time of the tropospheric air column to be 2 years. This value is roughly consistent with the one year decay time of the Pinatubo and El Chichon aerosols [*Hofmann and Rosen, 1987; Rosen et al., 1994*].

Since the time scales of horizontal diffusion in the atmosphere and oceans are so much smaller than the time scales of vertical diffusion, the rate-limiting step for thermal equilibration is vertical transport. For this reason, we consider only the variations in local temperature resulting from heat exchange vertically in the atmosphere and oceans.

The equation for temperature fluctuations in space and time in the model from equations 2.2 to 2.5 is

$$\frac{\partial \Delta T(x, t)}{\partial t} - \alpha(x) \frac{\partial^2 \Delta T(x, t)}{\partial x^2} = - \frac{\partial \eta(x, t)}{\partial x} \quad (9)$$

The mean value of η is zero and the flux of heat is proportional to the temperature:

$$\langle \eta(x, t) \rangle = 0 \quad (10)$$

$$\langle \eta(x, t) \eta(x', t') \rangle \propto \sigma(x) \langle T(x) \rangle^2 \delta(x - x') \delta(t - t') \quad (11)$$

The delta functions indicate that the white noise term η is uncorrelated in space and time.

North and Cahalan [1981] analyzed a similar model of climate change with respect to predictability. They studied the diffusion equation in two dimensions as a model for heat transport horizontally in the atmosphere. They included a white noise term on the right side of the diffusion equation (they used $\eta(x, t)$ where we use $\frac{\partial \eta(x, t)}{\partial x}$) to represent variations in

heat transport by turbulent eddies. However, a noise term in the *flux* of temperature rather than in the temperature itself is more appropriate as a model for variations in turbulent heat transfer.

The boundary conditions are that no heat flows out of the bottoms of the oceans and continuity of temperature and heat flux at the atmosphere-ocean boundary:

$$\sigma' \frac{\partial T}{\partial x} \Big|_{x=w_2} = 0 \quad (12)$$

$$\Delta T(x = w_1^+) = \Delta T(x = w_1^-) \quad (13)$$

$$\sigma \frac{\partial \Delta T}{\partial x} \Big|_{x=w_1^-} = \sigma' \frac{\partial \Delta T}{\partial x} \Big|_{x=w_1^+} \quad (14)$$

At the top of the atmosphere we impose a blackbody radiation boundary condition. Most (65%) of the energy incident on the Earth is reradiated as long-wavelength blackbody radiation from the H₂O and CO₂ in the atmosphere [Peixoto and Oort, 1992]. This radiated energy depends on the temperature of the atmosphere at the point of emission according to the Stefan-Boltzmann law. It is common practice to assume that temperature variations about equilibrium are small. This is a good approximation since the global mean temperature has fluctuated by only about ten degrees Kelvin during the last glaciation as illustrated in Figure 2.1. With a linear approximation, the radiated energy will be proportional to the temperature difference from equilibrium [Ghil, 1983]. The boundary condition at the scale height of the atmosphere (which we take to be representative of the average elevation where radiation is emitted from the atmosphere) is then

$$\sigma \frac{\partial \Delta T}{\partial x} \Big|_{x=0} = g \Delta T(x = 0) \quad (15)$$

We will use the value $g = 1.7 \text{ W/m}^2\text{K}$ as used by Ghil [1983] and Harvey and Schneider [1985]. It is often assumed that a feedback exists between atmospheric or sea-surface temperature and cloud cover. If such a feedback existed, it might be necessary to parameterize radiated energy in terms of cloud cover or atmospheric water vapor. However, no evidence for such a feedback has been found [Arking and Ziskin, 1994].

The existence of two layers of different diffusivity makes the study of the two-layer model much more complex than for the one-layer models applied to the atmosphere above the continents and the oceans. *Van Vliet et al.* [1980] used Green's functions to solve this two-layer model. The Green's function of the Laplace-transformed diffusion equation is defined by

$$i\omega G(x, x', i\omega) - \alpha(x) \frac{\partial^2 G(x, x', i\omega)}{\partial x^2} = \delta(x - x') \quad (16)$$

where G is governed by the same boundary conditions as ΔT . This equation can be solved by separating G into two parts: G_a and G_b with $x < x'$ and $x > x'$, respectively. G_a and G_b satisfy the homogeneous (unforced) diffusion equation with a jump condition relating G_a and G_b :

$$\frac{\partial G_a}{\partial x} \Big|_{x=x'} - \frac{\partial G_b}{\partial x} \Big|_{x=x'} = \frac{1}{\alpha(x')} \quad (17)$$

The power spectrum of the average temperature in the atmosphere in terms of G is given by *Van Vliet et al.* [1980] as:

$$S_{\Delta T}(f) \propto \text{Re} \left(\int_0^{w_1} \int_0^{w_1} G_1(x, x', i\omega) dx dx' \right) \quad (18)$$

$$\begin{aligned} &\propto \text{Re} \left(\int_0^{w_1} \int_0^x G_{1b}(x, x', i\omega) dx dx' \right. \\ &\quad \left. + \int_0^{w_1} \int_x^{w_1} G_{1a}(x, x', i\omega) dx dx' \right) \end{aligned} \quad (19)$$

where G_1 stands for the solution to the differential equation for G where the source point is located in the atmosphere and Re denotes the real part of the complex expression. Two forms of G_{1a} and G_{1b} are necessary for x located above and below x' , respectively, due to the discontinuity in the derivative of G_1 created by the delta function. The solution of G_1 which satisfies the above differential equation and boundary conditions is

$$\begin{aligned} G_{1a} = & \frac{L}{\alpha K} \left(\frac{\sigma' L}{\sigma L'} \sinh\left(\frac{w_1 - x'}{L}\right) \sinh\left(\frac{w_2}{L'}\right) \right. \\ & \left. + \cosh\left(\frac{w_1 - x'}{L}\right) \cosh\left(\frac{w_2}{L'}\right) \right) \left(\sinh\left(\frac{x}{L}\right) + \frac{\sigma}{Lg} \cosh\left(\frac{x}{L}\right) \right) \end{aligned} \quad (20)$$

and

$$G_{1b} = G_{1a} + \frac{L}{\alpha} \sinh\left(\frac{x' - x}{L}\right) \quad (21)$$

where

$$\begin{aligned} K = & \left(\sinh\left(\frac{w_1}{L}\right) + \frac{\sigma}{Lg} \cosh\left(\frac{w_1}{L}\right)\right) \frac{\sigma' L}{\sigma L'} \sinh\left(\frac{w_2}{L'}\right) \\ & + \left(\cosh\left(\frac{w_1}{L}\right) + \frac{\sigma}{Lg} \sinh\left(\frac{w_1}{L}\right)\right) \cosh\left(\frac{w_2}{L'}\right) \end{aligned} \quad (22)$$

and $L = (\alpha/i\omega)^{\frac{1}{2}}$ and $L' = (\alpha'/i\omega)^{\frac{1}{2}}$. Performing the integration *van Vliet et al.* [1981] obtained

$$\begin{aligned} S_{\Delta T}(f) \propto & \operatorname{Re}\left(L^2 \left(\frac{\sigma' L}{\sigma L'} \tanh\left(\frac{w_2}{L}\right) \left(\frac{gw_1}{\sigma} - 1\right) \right. \right. \\ & \left. \left. \tanh\left(\frac{w_1}{L}\right) - \frac{2gL \cosh(w_1/L) - 1}{\sigma \cosh(w_1/L)} + \frac{w_2}{L}\right) \right. \\ & \left. + \left(\frac{gw_1}{\sigma} + \left(\frac{w_1}{L} - \frac{gL}{\sigma} \tanh\left(\frac{w_1}{L}\right)\right) \left(\tanh\left(\frac{w_1}{L}\right) + \frac{\sigma L}{g}\right) \right. \right. \\ & \left. \left. \frac{\sigma' L}{\sigma L'} \tanh\left(\frac{w_2}{L'}\right) + \left(1 + \frac{\sigma}{Lg} \tanh\left(\frac{w_1}{L}\right)\right)\right)^{-1} \right) \end{aligned} \quad (23)$$

For very low frequencies several approximations can be made:

$$\tanh\left(\frac{w_1}{L}\right) \approx \frac{w_1}{L}, \quad \tanh\left(\frac{w_2}{L'}\right) \approx \frac{w_2}{L'} \quad (24)$$

$$\frac{\cosh(w_1/L) - 1}{\cosh(w_1/L)} \approx \frac{1}{2} \frac{w_1^2}{L^2} \quad (25)$$

Reducing equation 2-26,

$$S_{\Delta T}(f) \propto \frac{1}{1 + \omega^2/\omega_0^2} \propto \frac{1}{f^2 + f_0^2} \quad (26)$$

This is the low-frequency Lorentzian spectrum observed in the Vostok data. The crossover frequency as a function of the constants chosen for the model is

$$f_0 = \frac{g}{w_1 c \rho + w_2 c' \rho' (1 + gw_1/\sigma)} \quad (27)$$

At higher frequencies the following approximations hold

$$\tanh\left(\frac{w_1}{L}\right) \approx \frac{w_1}{L}, \tanh\left(\frac{w_2}{L'}\right) \approx 1 \quad (28)$$

$$\frac{\cosh(w_1/L) - 1}{\cosh(w_1/L)} \approx \frac{1}{2} \frac{w_1^2}{L^2} \quad (29)$$

then

$$S_{T_{av}}(f) \propto \frac{1}{2} \left(\frac{2gw_1}{\sigma}\right)^{\frac{1}{2}} \left(\frac{c\rho\sigma}{c'\rho'\sigma'}\right)^{\frac{1}{2}} \left(\frac{g}{w_1\rho c f}\right)^{\frac{1}{2}} \propto f^{-\frac{1}{2}} \quad (30)$$

This is the broad $f^{-\frac{1}{2}}$ region observed in the power spectrum of the temperature data and predicted based on the simpler one-layer model exchanging heat with regions above and below. The high- and low-frequency spectra meet at

$$f_1 = \frac{g}{w_1\rho c} \left(\frac{\sigma}{2gw_1}\right)^{\frac{1}{3}} \left(\frac{c'\rho'\sigma'}{c\rho\sigma}\right)^{\frac{1}{3}} 4^{\frac{1}{3}} \left(\frac{c\rho w_1}{c'\rho' w_2}\right)^{\frac{4}{3}} \quad (31)$$

$$\approx 1/(10\text{kyr}) \quad (32)$$

This value agrees within an order of magnitude to that observed in the Vostok data ($f \approx 1/(2 \text{ kyr})$).

At time scales less than 2 kyr, fluctuations in heat energy input into air masses from the oceans or variations in emitted radiation can be absorbed by the other reservoir. At lower frequencies, the atmosphere and oceans are in thermal equilibrium. The oceans can no longer absorb thermal fluctuations input into the atmosphere from fluctuations in radiative emission at this time scale and vice versa. The variance in temperature of the atmosphere and oceans is then determined solely by the radiation boundary condition. The fluctuating temperature at the top of the atmosphere will result in a white noise flux out of the atmosphere-ocean system. The average temperature of the atmosphere and oceans will be given by the sum of a white noise, a Brownian walk. This is observed in the Vostok data. The Brownian walk behavior of the climate system flattens out at low frequencies as a result of a negative feedback mechanism: as the coupled atmosphere and oceans warm up (or cool down) due to nonstationary fluctuations of the random heat exchange from radiative emission, the system

will radiate, on average, more (less) radiation, limiting the variance at low frequencies. This interpretation depends on the conductivity being low compared to the time scale for radiative damping, $\tau = c'\rho'w_2/g$. If so, the rate-limiting step of radiative equilibrium is the conduction of heat from the oceans through the atmosphere. The time constant of this thermal discharge (analogous to the electrical discharge of an RC circuit) is then $\tau = \sigma/w_1w_2c'\rho'$. However, if the conductivity is high, the time scale of radiative equilibrium is determined by the time scale for radiative damping, $\tau = c'\rho'w_2/g$. Using the estimates for the thermal diffusion properties of the atmosphere and the oceans listed in Figure 2.14, the conductivity is large and the low-frequency portion of the spectrum is governed by the radiative damping constant. This is problematic, however, because the time scale of radiative equilibrium is then $\tau = c'\rho'w_2/g = 600$ yr. Such a short time scale implies that no f^{-2} spectral region should exist at all. An atmospheric vertical diffusivity of $0.1 \text{ m}^2/\text{s}$ is required in order for the model spectrum to be consistent with the spectrum of the Vostok data with the $f \approx 1/(40 \text{ kyr})$ crossover frequency. This is an order of magnitude smaller than the values quoted by *Pleune* [1990] and *Seinfeld* [1986].

Besides the frequency dependence of the power spectrum, the model we have presented predicts that the distribution of temperature variations from equilibrium obeys a Gaussian distribution. This is because the stochastic term obeys a Gaussian distribution function and the temperature fluctuations are related to the stochastic term through a linear transformation. By definition, the probability density function is only defined for time scales in which the temperature fluctuation time series are stationary. Gaussian time series with power-law power spectra of the form $S(f) \propto f^{-\beta}$ are stationary if $\beta < 1$ and non-stationary if $\beta \geq 1$ (MT section 5). Thus, a unique probability density function only exists for very long time scales (greater than 100 kyr) where the power spectrum is constant ($\beta = 0$) and for the range of time scales in which the power spectrum obeys $S(f) \propto f^{-\beta}$ with $\beta = \frac{1}{2}$. *Matteucci* [1990] has computed the probability distribution function for climatic variations at very long time scales with the SPECMAP stack. He obtained a Gaussian distribution. Similarly, *Janosi and Vattay* [1992] have obtained a Gaussian distribution with monthly temperature datasets

of several decades length with the annual variability removed.

Manabe and Stouffer [1996] have completed power-spectral analyses of variations in local atmospheric temperature in control runs of a coupled atmosphere-ocean-land surface model. They computed the power spectrum of temperature time series of each surface grid point and then averaged the power spectra at equal frequency values, as in our observational power-spectral analyses. Their results are presented in Figure 2.15. They found different spectra for continental and maritime gridpoints. Maritime gridpoints exhibited power-law power spectra from time scales of one month to several hundred years with an exponent of close to -0.25 . Continental gridpoints, however, showed flat spectra up to time scales of about 100 yr, in contrast to observations. Exploring the similarities and differences between the approach in this paper, GCM results such as those of *Manabe and Stouffer* [1996], and observations should enable us to learn more about this fundamental problem in Earth science.

Time-series analysis of paleoclimatic data often exhibit a dominant peak near 100 kyr. Although variations in the eccentricity of the Earth's orbit occur with this frequency, this variation is not expected to produce a linear influence on climate change since this orbital variation results in only a fraction of a percent change in the amount of radiation incident on the Earth [*Hays et al.*, 1976]. Although there are nonlinear models that predict a 100 kyr periodicity, it is generally agreed that the underlying mechanism for this peak is not well understood [*Kerr*, 1978]. The model presented in this section leaves the question open as it does not predict any periodicity. The only component of the system thought to have a characteristic time scale of 100 kyr is the cryosphere [*Mitchell*, 1976]. Perhaps the cryosphere can produce a 100 kyr peak in the power spectrum when forced by the background spectrum predicted by the model of this paper. Studies incorporating the cryosphere into our model are an important extension of our work that may lead to new insights into the nature of the 100 kyr periodicity.

D. Variations in solar luminosity

We have applied the same model presented in this Section 4.4 to variations in the solar luminosity from time scales of minutes to months [*Pelletier*, 1996]. In Figure 2.16 we present the power spectra estimated with the Lomb periodogram of ACRIM solar irradiance data sampled during 1987 and 1985 plotted as a function of the frequency in hours^{-1} . The same sequence of power-law behavior is observed in these data as are observed in the Vostok data. Large peaks appear at the orbital frequency of the satellite and its harmonics. These peaks are an artifact of the spectral estimation. A stochastic diffusion model of the turbulent heat transfer between the granulation layer of the sun, modeled as a homogeneous thin layer with a radiative boundary condition, and the rest of the convection zone, modeled as a homogeneous thick layer with thermal and diffusion constants appropriate to the lower convection zone, predicts the same spectral form observed in solar irradiance data. The time scales of thermal and radiative equilibrium of the solar convection zone based upon thermal and diffusion constants estimated from mixing-length theory match those observed in the ACRIM data. Further details are discussed in *Pelletier* [1996].

E. Drought hazard assessment

One of the principle applications of time-series analysis is to drought hazard assessment. A major question is whether “short-memory” models are adequate or whether “long-memory” models such as self-affine noises and walks are required [*Bras and Rodriguez-Iturbe*, 1985].

Since hydrologic droughts are phenomena requiring multiple years of low flow, the frequency of occurrence will be affected by correlations in the time series of discharge. We now illustrate how fractional noises can be used to estimate drought frequencies. The use of fractional noises that exhibit the Hurst phenomenon has been proposed by *Booy and Lye* [1989] for use in flood-frequency analysis. The goal of stochastic hydrology is to generate

synthetic time series of river discharge that accurately reproduce hydrological time series. Based on evidence for the applicability of a fractional noise with $\beta \approx 1/2$, we generated synthetic time series with two-parameter log-normal distributions that fit the historical records of river discharge. We first discuss the techniques and results of drought frequency analyses for series with different log-normal distributions. Then we discuss the results of a comparison between drought frequencies for the Colorado river based upon a fractional noise with exponent of $-1/2$ and a short-memory AR(1) model.

Techniques for generating synthetic log-normal fractional noises have been discussed by MT, Section 4.2. We utilize synthetic noises with $\beta = 1/2$ and $c_v = 0.2, 0.4,$ and 0.6 . There is no unique definition of a drought; several alternatives were discussed in a recent drought assessment of the southwestern U.S. by *Tarboton* [1994]. Perhaps the most straightforward definition is that proposed by *Yevjevich* [1967] and *Dracup et al.* [1980]. They defined a drought as any year or consecutive number of years during which average annual streamflow is continuously below the long-term mean annual runoff. The magnitude is the average deficit during the drought. The principal drawback to this definition is that two 5-year droughts separated by one wet year will only be recognized as 5-year droughts even though the succession of droughts results in ten or eleven years of critically low supply. In Figure 2.17 we present the results of drought frequency analyses based on this definition of a drought. Each part is a two-dimensional contour plot of the logarithm (base 10) of the recurrence interval of a drought of a given duration and magnitude, with the magnitude normalized to the mean flow. Figure 2.17 a, b, and c represent coefficients of variation 0.2, 0.4, and 0.6, respectively. To construct each figure we generated synthetic records of one million years in length and searched them for drought occurrences.

In order to assess the importance of long-range persistence on the likelihood of severe drought, we have completed a drought frequency analysis using an AR(1) model for the Colorado river at Lees Ferry [*Kendall and Dracup*, 1991] with a fractional noise model for the same location. The synthetic time series were one million years in length. We found that for droughts of ten years duration and small magnitude, 100-year events according to

the fractional noise model, the difference in recurrence interval for the two models is a factor of five. We conclude that the presence of long-range persistence has a significant effect on the likelihood of severe drought. The presence of long-range persistence does not, however, appear to improve the ability to predict future climatological and hydrological time series to any significant degree [Noakes *et al.*, 1988].

III. VARIATIONS IN SEDIMENTATION

A. Introduction

We now turn to porosity variations in sedimentary basins. We show that these variations are self-affine walks in both the horizontal and vertical directions. We show that the observed distributions can be reproduced using a standard model for surface growth. We will further show that this model is consistent with the observed variations and episodicity in sediment deposition.

In the past decade many studies have documented the scale-invariance of porosity and density variations in sedimentary basins. Power-law power spectra of vertical density and porosity well logs have been reported by *Hewett* [1986], *Walden and Hosken* [1985], *Pilkington and Todoschuck* [1990], *Todoschuck et al.* [1990], *Holliger* [1996], *Shiomi et al.* [1996], *Dolan et al.* [1996], and *Pelletier and Turcotte* [1996]. *Tubman and Crane* [1995] and *Deshpande et al.* [1996] have presented evidence for scale-invariant horizontal variations in density and porosity from well logs and seismic data. In addition, *Dunne et al.* [1995] presented evidence that the topography of alluvial plains along the channel strike is also scale-invariant. They performed spectral analyses on fluvial microtopographic transects of an alluvial plain in Kenya. They obtained power spectra with $S(k) \propto k^{-\beta}$ where k is the wave number and β ranges from 1.5 to 2. Based on his original observation, *Hewett* [1986] developed a fractal-based interpolation scheme for determining the three-dimensional porosity variations in sedimentary basins using available well logs. The validity of the

interpolated structure was subsequently verified in a variety of ways. This approach was applied to modeling ground water migration by *Molz and Boman* [1993].

B. Surface growth model

Before considering the observed spectra further, we present a model for surface growth which will be predictive of both vertical and horizontal porosity variations in sedimentary basins. At each time step, a site on a one-dimensional lattice is chosen at random. During that time step, a unit of sediment is deposited on that site or on one of its nearest neighbors, depending on which site has the lowest elevation. This is the simplest model combining randomness and the tendency for sediment to be deposited in low-lying areas of an alluvial plain. The model is illustrated in Figure 3.1. The cross-hatched block shows the unit of sediment being added to the surface. In each case, an arrow points towards the site upon which the unit of sediment will be deposited. In Figure 3.1a the chosen site has a lower elevation than either of its nearest neighbors, so the sediment is deposited at the chosen site. In Figure 3.1b one of the nearest neighboring sites has a lower elevation and the sediment is deposited at that lower site. In the case of a tie for the lowest elevation between two or three sites, the site on which the sediment is deposited is chosen randomly between the sites of the same elevation, as in Figure 3.1c. The local elevation is the total number of units of sediment that have been deposited at the site.

This model of surface growth was first analyzed by *Family* [1986] with applications to the growth of atomic surface layers. He reported the results of computer simulations which showed that the model produces scale-invariant variations of the surface in space and time. He found that the standard deviation, σ , of the surface follows the relation

$$\sigma(L, T) \propto L^{\frac{1}{2}} T^{\frac{1}{4}} \quad (1)$$

where L is a length scale and T is a time scale. Surfaces with scale-invariant standard deviations $\sigma(L, T) \propto L^{H_{ax}} T^{H_{at}}$ have a power-law dependence of the power-spectral density,

$S(k)$, on wave number k of the form $S(k) \propto k^{-2Ha_x-1}$ (i.e. $\propto k^{-2}$ for $Ha_x = 1/2$) and a power-law dependence on frequency of the form $S(f) \propto f^{-2Ha_t-1}$ (i.e. $\propto f^{-\frac{3}{2}}$ for $Ha_t = 1/4$).

An example of the surface elevation produced by the model with 1024 grid points is given in Figure 3.2. The average dependence of the power-spectral density on wave number from fifty independent simulations is given in Figure 3.3. The power spectrum is proportional to k^{-2} indicating that the surface is a Brownian walk. Other lattice sizes yield similar results. The synthetic topography given in Figure 3.2 is very similar to the one-dimensional transect of Kenyan topography obtained by *Dunne et al.* [1995] and plotted in Figure 3.4. *Hooke and Rohrer* [1979] have mapped the topographic profiles of alluvial fans perpendicular to the flow direction. The synthetic profile is also strikingly similar to their alluvial fan profiles.

In Figure 3.5 we plot the variations in surface elevation (subtracted from the mean height of the landscape) at the central site of our simulation after the simulation has reached a dynamic steady state. In Figure 3.6 we present the average power spectrum of the difference from the mean height of the central site produced in fifty simulations. The power spectrum is proportional to $f^{-\frac{3}{2}}$. If deposition and erosion took place independently, the variation of the local elevation relative to the mean with time would be a random walk with power spectrum $S(f) \propto f^{-2}$. The random-walk model has been analyzed as a model for sedimentary bed formation. The effect of the diffusion term is to preferentially fill low-lying areas of the alluvial plain. This results in an anticorrelated sequence of deposition and erosion: after an area has aggraded it has a higher elevation and a lower rate of future aggradation. Without the presence of the diffusion term, the surface would be white noise. The random-walk model, therefore, results in a very unrealistic alluvial plain topography.

We can also include the effects of erosion in our model. Although deposition generally occurs in topographic depressions, tending to smooth out the floodplain, erosion is less consistent. Erosion can downcut in a channel or, during a large flood, can lower alluvial ridges. We have modified our simulation to include the effects of erosion by choosing randomly at each timestep whether to deposit or erode sediment during that timestep. The probability of deposition must be greater than 0.5 in order to accumulate a sedimentary basin over time.

We have studied the above model assuming that erosion occurs preferentially on channel floors, randomly on the landscape, or preferentially on alluvial ridges. In the simulations in which we assumed erosion to occur preferentially on the channel floors, we have included an erosion rule that takes away rather than deposits a unit of sediment at a randomly chosen site or one of its nearest neighbors, depending on which has the lowest elevation. We have also investigated rules that remove a unit of sediment only from the chosen site (to simulate random erosion on the floodplain) and a rule that removes sediment from the chosen site or one of its nearest neighbors, depending on which site is highest, to simulate the preferential erosion of alluvial ridges. The exponents of the power-law power spectra obtained in the model without erosion are unchanged for any of these erosion models.

In the simplest version of the model which includes only deposition the probability that a particle is added to the site is proportional to two if both of a site's neighbors have a higher elevation, proportional to one if only one of the neighbors is higher, and zero if both neighbors are lower. The model may be described mathematically with a stochastic difference equation of the form

$$h_{i,t+1} - h_{i,t} \propto \Theta(h_{i+1,t}, h_{i,t}) + \Theta(h_{i-1,t}, h_{i,t}) \quad (2)$$

where $h_{i,t+1} - h_{i,t}$ represents the most probable growth rate of the surface and Θ is the Heavyside function defined by $\Theta(x, x_o) = 1$ if $x > x_o$ or 0 if $x < x_o$. Averaging this equation over a time long compared to the time required to grow a single layer of unit height of sediment, the equation for the average surface growth rate is

$$\langle h_{i,t+1} - h_{i,t} \rangle \propto \langle h_{i+1,t} - h_{i,t} \rangle + \langle h_{i-1,t} - h_{i,t} \rangle \quad (3)$$

$$\propto \langle h_{i+1,t} \rangle - 2\langle h_{i,t} \rangle + \langle h_{i-1,t} \rangle \quad (4)$$

This is a discrete version of the diffusion equation. Directing sediment to lower elevations smooths out the surface and is equivalent to a diffusion process. As recognized by *Family* [1986], a continuous version of the discrete model is provided by a one-dimensional diffusion equation with a Gaussian white noise term:

$$\frac{\partial h(x, t)}{\partial t} = D \frac{\partial^2 h(x, t)}{\partial x^2} + \eta(x, t) \quad (5)$$

The term $\eta(x, t)$ represents actual deposition and erosion. The assumed Gaussian white noise is characterized by a mean, $\bar{\eta}$, and a standard deviation σ . If $\bar{\eta} = 0$ there is no net deposition and sedimentation balances erosion. For $\bar{\eta} > 0$ there is net deposition and for $\bar{\eta} < 0$ there is net erosion. The ratio $\sigma/\bar{\eta}$ is a measure of the amplitude of fluctuations in the sedimentation process. The diffusion term in equation 3.5 introduces both spatial and temporal correlations in the sedimentation process not present in the random-walk model.

C. Observations

We will next consider some observed spectra of the vertical variations of porosity in sedimentary basins and compare them with the results we have obtained. Porosity as a function of depth is routinely measured at equal intervals in formation well logs [Hewett, 1986]. As a specific example we have considered porosity logs from 15 wells in the Gulf of Mexico. One of the logs is plotted in Figure 3.7. The wells are drilled in a deltaic sedimentary environment with a few large, nearly vertical faults [Alexander, 1995]. The power spectra for these wells are given in Figure 3.8. as a function of the wavenumber k in m^{-1} . At spatial scales larger than ≈ 3 m the power spectra are well approximated by a power law. Below this scale the power-spectral density decreases sharply in most of the wells. This decrease may be the result of a transition from second-order heterogeneities (dominated by variations in porosity within the larger genetic units) to third order heterogeneities which result from the geometrical arrangements of individual depositional units. The transition from second to third-order heterogeneities occurs at the scale of meters [Allen and Allen, 1990] and is consistent with the 3 m scale of the break observed in the power spectra. We estimate β from the slope of the least-square linear fits to the log-log plots at scales greater than 3 m. The values of β obtained exhibit considerable variability from well to well. However, the average $\beta = 1.4$ is close to the value 1.5 predicted by the model. The standard deviation is 0.2.

Dolan et al. [1996] reported ranges of values of β from time-series analyses of vertical density and porosity variations in well logs. They obtained average power spectral exponents $\beta = -1.50, -1.62,$ and -1.46 using three different numerical procedures for a cluster of ten wells in a fluvial sedimentary environment. These values are in excellent agreement with the ones we obtained and with our model. *Holliger* [1996] has reported values of β from 1.2 to 1.4, somewhat smaller, but roughly consistent with the values reported here.

We will next consider several observational studies relevant to the horizontal variations of porosity in sedimentary basins. Direct measurements of topography on relevant scales have been carried out by *Dunne et al.* [1995]. These authors have performed power spectral analyses of fluvial microtopographic transects perpendicular to the fall line from two hillslopes obtained with laser altimetry from scales of 0.1 to 100 m. Their work provides us with a direct test of our model for the topographic variations of an alluvial plain. They obtained power spectra with a power-law dependence on wave number as predicted. The exponents of the power spectra had an average of $\beta = 1.6$ with a standard deviation of 0.2, somewhat smaller than our model prediction of $\beta = 2$.

In addition to the power-spectral behavior of the surface in space and time discussed above, the stochastic diffusion model also predicts a Gaussian distribution of the surface elevation. This is true of any linear stochastic differential equation with Gaussian noise. The microtopographic transects obtained by *Dunne et al.* [1995] enable us to test this prediction. In Figure 3.9 we present the distribution of elevations from the 15 profiles published by the authors. The profiles were digitally scanned for the analysis. Also plotted in Figure 3.9 is the non-linear least-square fit to a Gaussian distribution. A good fit is obtained.

We will next show that the distribution of producing oil and gas wells is consistent with $\beta=2$ horizontal porosity variations. *Barton and Scholz* [1995] have presented the spatial distribution of drilled wells and wells showing hydrocarbons in the Denver and Powder River basins. These basins evolved from sediment deposition in a meandering alluvial environment [*Berg*, 1968]. Using the box counting technique, *Barton and Scholz* [1995] found that the fractal dimensions for the drilled wells in the two basins were 1.80 and 1.86 and that the

fractal dimensions of wells showing hydrocarbons were 1.43 and 1.49, respectively. After petroleum is generated and migrates from source rocks, it will move from sites of high potential energy to sites of low potential energy. Hydrocarbons are found in traps that are the crests of low-porosity caprock that have obstructed its upward migration [Allen and Allen, 1990]. The caprock will mimic the floodplain relief at the time of its deposition. This is consistent with the observation that hydrocarbons are often found in geometries which mimic the topography of the alluvial plain at the time of deposition in a variety of fluvial depositional environments such as meandering [Curry and Curry, 1972], deltaic [Coleman and Prior, 1982], and submarine fans [Garcia, 1981; Wilde et al., 1978]. A simple model for the horizontal spatial distribution of hydrocarbons in a reservoir is one in which hydrocarbons are assumed to be accumulated in all of the crests of the caprock above a certain elevation.

The spatial distribution of wells showing hydrocarbons in the Powder River and Denver basins are given in Figure 3.10. We have set the width of each basin to be 128 units so as to facilitate comparisons with a synthetic reservoir constructed on a 128 x 128 grid. We analyzed the data with the pair-correlation function which we believe to be a better estimator of correlations for point processes than box counting.

The two-dimensional pair-correlation function $C(r)$ is defined as the number of pairs of wells whose separation is between r and $r + \Delta r$, per unit area [Vicsek, 1992]. The pairs are binned in logarithmically spaced intervals Δr . For a data set with scale invariant clustering, $C(r) \propto r^{-\alpha}$ where α is related to the fractal dimension through $D = 2 - \alpha$ in two dimensions [Vicsek, 1992]. The pair-correlation function is commonly employed in the analysis of diffusion-limited-aggregation. However, studies incorporating it in the earth sciences are rare. Kagan and Knopoff [1980] have applied it to the spatial clustering of earthquakes. Figure 3.11 shows the pair-correlation function of the Denver and Powder River basin wells on a log-log plot. The least-square fits to the correlation function yield exponents of $\alpha = -0.59$ for Powder River and $\alpha = -0.50$ for the Denver basin, implying $D = 1.41$ and $D = 1.5$, respectively. The results obtained by the pair-correlation method

are in close agreement with the results obtained by *Barton and Scholz* [1995] using box counting.

To show that these correlation functions are consistent with a caprock with Brownian walk topography, we have constructed synthetic reservoirs where hydrocarbon traps are regions where the caprock elevation is larger than a threshold value. In order to do this we synthesized two-dimensional fractional Brownian walks on a 128 x 128 lattice with the Fourier-filtering technique discussed in MT Section 3.1. The threshold value for showing hydrocarbons was chosen such that the resulting synthetic reservoir had the same percentage of showing wells as the Denver and Powder River basins (about 5%). Figure 3.12 shows a synthetic reservoir produced with $\beta = 2.0$ (a Brownian walk). The synthetic reservoir shows a degree of clustering similar to the Denver and Powder River basins. In Figure 3.9 we have plotted the pair-correlation functions for the showing wells in synthetic reservoirs constructed with $\beta = 2.5, 2.0, 1.5,$ and 1.0 . The pair-correlation functions show a gradual decrease with decreasing β . The synthetic reservoirs whose scaling exponents α most closely match those of the Denver and Powder River basins are $\beta = 2.0$ and $\beta = 1.5$. Although we cannot precisely determine the scaling exponent of the porosity variations with this method, we conclude that β is close to 2, consistent with our model.

Besides the pair-correlation function, two other fractal relations allow us to infer Brownian walk paleotopography from horizontal variations in sedimentary basins. *Agterberg* [1982] has computed the fractal dimension of the perimeter of sand isopach contours from the Lloydminster oil field to be 1.3, close to the value of 1.25 measured for coastlines and topographic contours [*Turcotte*, 1992]. *Barton and Scholz* [1995] have presented frequency-size distributions of oil pools. They found that the cumulative number of oil fields has a power-law dependence on the volume of the fields with exponent close to -1: $N(> V) \propto V^{-1}$. *Kondev and Henley* [1995] have related the length distribution of contour lengths of Gaussian surfaces to the Hausdorff measure Ha . *Pelletier* [1997b] has shown that their results imply that the cumulative frequency-area distribution of areas enclosed by contours of a Brownian walk surface is $N(> A) \propto A^{-3/4}$. Since oil fields have a much larger horizontal

extent than vertical extent, it is reasonable to assume that area and volume are proportional. Our model of the migration of hydrocarbon into regions with caprock topography above a threshold elevation then predicts $N(> V) \propto V^{-3/4}$ in reasonable agreement with the cumulative frequency-size distributions of *Barton and Scholz* [1995]. *Pelletier* [1997b] has employed the same techniques to infer the self-affinity of the top of the convective boundary layer from the size-distribution of cumulus cloud fields.

D. Completeness of the sedimentary record

A related problem to topography and porosity variations in sedimentary basins is the statistics of preserved sections. Stratigraphic sections are formed by alternating periods of deposition and erosion or non-deposition. The resulting stratigraphic section contains the deposited sediments that were not subsequently eroded. Various stochastic models have been proposed to explain aspects of sedimentary bed formation, including the frequency distribution of bed thicknesses. Beginning with Kolmogorov's work [*Kolmogorov*, 1951], many studies have investigated random-walk models of sedimentation. Random-walk models assume that the magnitude of alternating depositional and erosional events are independent. These models are applied by letting the typical episodes of deposition and erosion define minimal units of a discrete time scale. The lengthy periods of non-deposition, as well as any long intervals of deposition and erosion, are treated as multiples of these units. There have been a number of variants of Kolmogorov's work: *Schwarzacher* [1975] described a process of bed formation that results in a random walk on the integers, *Vistelius and Feigel'son* [1965] allowed different types of sediment to be deposited, *Dacey* [1979] considered both exponential and geometrical probability distributions for the amount of sediment deposited and eroded, and *Strauss and Sadler* [1989] have considered a continuous version of the random-walk model. These models are generally considered to be successful at predicting observed bed thickness distributions [*Strauss and Sadler*, 1989].

Tipper [1983] was the first to apply the random-walk model to the problem of stratigraphic completeness: given that deposited sediment is often later eroded, how much of the depositional history is preserved in a given stratigraphic section? *Sadler* [1981] obtained a solution to this problem by investigating the dependence of sedimentation rate on the time span over which the sedimentation rate was measured. If the dependence of the sedimentation rate on time span can be assessed, then for a single stratigraphic section, the ratio of the overall accumulation rate to the average rate at time span T is the completeness [*Sadler and Strauss*, 1990]. *Sadler* quantified the sedimentation rate, R , as a power-law function of time span, T , with exponent -0.65 : $R \propto T^{-0.65}$. *McShea and Raup* [1986] have critically reviewed *Sadler's* approach, indicating possible biases in the data he compiled. *Sadler* interpreted the decreasing sedimentation rate with time as the result of including longer and longer hiatuses of erosion or non-deposition in the average at longer time intervals. *Plotnick* [1986] introduced a fractal model for the length distribution of stratigraphic hiatuses that is consistent with this interpretation and predicts a power-law dependence of sedimentation rate on time span. *Tipper* [1983], *Strauss and Sadler* [1989], and *Sadler and Strauss* [1990] have addressed the issue of stratigraphic completeness with the random-walk model of sedimentation. The random-walk model predicts a power-law dependence of sedimentation rate on time with exponent $-\frac{1}{2}$: $R \propto T^{-\frac{1}{2}}$, giving quite good agreement with *Sadler's* data.

The time history of sedimentation at a point based on our model is given in Figure 3.14 and 3.15. Figure 3.14 is the complete history of deposition and erosion at a point in the basin. The time series of deposition and erosion is represented by a fractional Brownian walk with power spectrum $S(f) \propto f^{-\frac{3}{2}}$. This fractional Brownian walk represents the elevation of total height of sediment deposited locally in a fluvial sedimentary basin, superimposed on a constant rate of subsidence. The time series is scale-invariant in terms of the nondimensional sedimentary thickness, $h\sigma/D$, and time, $t\sigma^2/D$; it is characterized by the single parameter $\sigma/\bar{\eta}$. If $\sigma/\bar{\eta}$ is small the fluctuations in sedimentation rate are small compared to the subsidence rate; if $\sigma/\bar{\eta}$ is large the fluctuations are large. For the example given in Figure 3.14, $\sigma/\bar{\eta} = 0.1$. Figure 3.15 is produced from Figure 3.14 by removing any deposited

sediment that is subsequently eroded. In the “staircase” plot of Figure 3.15, beds are defined as a time interval of continuous deposition, i.e. a series of consecutive timesteps with increasing elevations. Hiatuses are defined as periods in which no sediment is preserved, i.e. a series of consecutive timesteps with the same elevation.

We will next discuss the relationship between sedimentation rate and time span with the stratigraphic model of Plotnick (1986) based on a deterministic fractal distribution of hiatus lengths. The age of sediments in this model is given as a function of depth in Figure 3.16a. As illustrated, the vertical segments (beds) are of equal thickness. The positions of the transitions from beds to hiatuses are given by a second-order Cantor set. Eight kilometers of sediments have been deposited in this model sedimentary basin in a period of 9 Myr so that the mean rate of deposition is $R(9 \text{ Myr}) = 8 \text{ km} / 9 \text{ Myr} = 0.89 \text{ mm/yr}$ over this period. However, there is a major unconformity at a depth of 4 km. The sediments immediately above this unconformity have an age of 3 Ma and the sediments immediately below it have an age of 6 Ma. There are no sediments in the sedimentary pile with ages between 3 and 6 Ma. In terms of the the Cantor set this is illustrated in Figure 3.16b. The line of unit length is divided into three parts and the middle third, representing the period without deposition, is removed. The two remaining parts are placed on top of each other as shown.

During the first three million years of deposition (the lower half of the sedimentary section) the mean rates of deposition are $R(3 \text{ Myr}) = 4 \text{ km} / 3 \text{ Myr} = 1.33 \text{ mm/yr}$. Thus the rate of deposition increases as the period considered decreases. This is shown in Figure 3.16c.

There is also an unconformity at a depth of two kilometers. The sediments immediately above this unconformity have an age of 1 Ma and sediments below have an age of 2 Ma. Similarly there is an unconformity at a depth of 6 km, the sediments above this unconformity have an age of 7 Ma and sediments below an age of 8 Ma. There are no sediments in the pile with ages between 8 and 7 Ma or between 2 and 1 Ma. This is clearly illustrated in Figure 3.16a. In terms of the Cantor set, Figure 3.16b, the two remaining line segments of

length $1/3$ are each divided into three parts and the middle thirds are removed. The four remaining segments of length $1/9$ are placed on top of each other as shown. During the periods 9 to 8, 7 to 6, 3 to 2, and 1 to 0 Myr the rates of deposition are $R(1 \text{ Myr}) = 2 \text{ km} / 1 \text{ Myr} = 2 \text{ mm/yr}$. This rate is also included in Figure 3.16c.

The rate of deposition clearly has a power-law dependence with respect to the length of the time interval considered. The results illustrated in Figure 3.16 are based on a second-order Cantor set but the construction can be extended to any order desired and the power-law results given in Figure 3.11c would be extended to shorter and shorter time intervals.

The sedimentation rate has been calculated in this way based on the sedimentation history of Figure 3.15. The results are plotted in Figure 3.17 on a logarithmic scale. The sedimentation rate has a power-law dependence on time span with exponent $-\frac{3}{4}$: $R \propto T^{-\frac{3}{4}}$. *Sadler and Strauss* [1990] have shown that the random-walk model results in a power-law relationship with exponent $-\frac{1}{2}$. Our result is a better fit to the data of Sadler (1981) who has compiled measurements of fluvial sedimentation rates from the geological literature for time scales of minutes to 100 million years. His data are plotted in Figure 3.18 where they are averaged in bin sizes with an equal spacing on a logarithmic scale. In this plot we have not included the data on time scales from 10^5 to 10^8 years since these time scales include unconformities resulting from regressive and transgressive events on active margins. Variations in sea level are beyond the scope of the model and it would be inappropriate to compare the model to sedimentation rates on those time scales. A least-square linear fit to the log-log plot yields a slope of -0.76 . This result is consistent with the model result given in Figure 3.17.

These results can also be obtained from theoretical fractal relations. Fractional Brownian walks have the property that the standard deviation of the time series has a power-law dependence on time with a fractional exponent Ha , the Hausdorff measure: $\sigma \propto T^{Ha}$ as given by MT equation 3.2. The rate of change of the time series for a given time interval, T , is then the sedimentation rate $R = \sigma/T \propto T^{Ha-1}$. The power-spectral exponent of a time series and its Hausdorff measure are related by $\beta = 2Ha + 1$ (MT equation 5.10). For the

random-walk model, $\beta = 2$, $Ha = 1/2$, and the sedimentation rate is then $R \propto T^{-\frac{1}{2}}$. For the stochastic diffusion model, $\beta = 3/2$, $Ha = 1/4$, and $R \propto T^{-\frac{3}{4}}$, in agreement with the numerical results.

The dependence of sedimentation rate on time span continues up to time scales of the Wilson cycle. On time scales of 10^5 - 10^8 years, transgressive and regressive events give rise to alternating periods of deposition and erosion as mentioned previously. *Korvin* [1992] found, using the SEDPAK simulation package, that alternating periods of deposition and erosion resulting from sea level change, combined with the diffusive parameterization of sediment transport of SEDPAK, resulted in a decreasing sedimentation rate with increasing time span in the same way that channel avulsion and diffusive sediment transport results in episodic sedimentation rates on smaller time scales.

E. Bed thicknesses

Working from our preserved thickness history of Figure 3.10b, we will define a bed as any consecutive sequence of time units with different thickness. Conversely, a hiatus is any consecutive sequence of time units with the same thickness. In this section we will present bed thickness and hiatus length distributions and compare them with observations and with other models.

Plotnick [1986] presented the model for discontinuous sedimentation based on a fractal distribution of hiatus lengths from in Figure 3.15. The cumulative distribution of hiatus lengths, the number of hiatuses greater than or equal to a length of time, T , produced by our model is plotted in Figure 3.19. In order to obtain an accurate curve, we generated 100 synthetic preserved thickness histories and accumulated the hiatus distributions to obtain Figure 3.19. The distribution is not fractal. This was at first surprising since a fractal distribution of hiatuses was used to illustrate how a power-law dependence of sedimentation rate on time span can occur. However, in the model of Figure 3.16 each bed had the same thickness. In contrast, as we will show, the stochastic diffusion model of sedimentation

results in bed thicknesses with an exponential distribution. Therefore, our observation of a scale-invariant sedimentation rate without a scale-invariant distribution of hiatuses is not inconsistent with the model of Figure 3.16 since they result in different bed thickness distributions.

The cumulative distribution of bed thicknesses generated by our model is plotted in Figure 3.20 for the four different values of $\sigma/\bar{\eta}$ indicated next to each distribution. For synthetic depositional histories with a relatively large $\sigma/\bar{\eta}$, such as 0.1, no deposition occurs during most of the history. The result is a small number of beds with a very skewed distribution. For smaller ratios, more thick beds appear in the record. The straight line trends of the distributions on a log-linear axis indicate that the cumulative bed thickness distributions are exponential. The non-cumulative distribution is also exponential since the cumulative distribution is the integral of the non-cumulative distribution. Exponential bed thickness distributions are common in stochastic models of sedimentation [Dacey, 1979]. Despite reported conclusions that stochastic models of sedimentation, including those that generate exponential bed thickness distributions, accurately predict observed bed-thickness distributions [Mizutani and Hattori, 1972], we are not aware of any model which predicts the commonly observed log-normal distribution. This may be a fundamental weakness of the bed formation models that have been proposed to date. Another possibility has been suggested by Drummond and Wilkinson [1996]. They have argued that the observation of log-normal distributions is an artifact resulting from unrecognized or unrecorded small strata. They propose that exponential distributions are consistent with the data if the data for the frequencies of the smallest strata are considered incomplete and not considered in the distribution fitting. This is consistent with the conclusion of Muto [1995] who has presented the cumulative frequency-thickness distribution of four large turbidite datasets from Japan. He found that an exponential distribution best fit the data. However, power-law distributions have also been persuasively argued for the distribution of turbidite beds [Rothman et al., 1993].

In Figure 3.20, synthetic sedimentation histories with larger values of sedimentation

rate, $\sigma/\bar{\eta}$, have a more skewed distribution or a steeper slope on a log-linear scale. This is consistent with the dependence of skew on sedimentation rate observed in deep-sea sequences in Italy by *Claps and Masetti* [1994]. These authors published bed-thickness data from three formations in Italy: Ra Stua, Castagne, and Cismon Valley. The sedimentation rates for a 1 Ma time scale have been estimated to be 2.5, 1.7, and 0.6 cm/kyr, respectively, for these sections. In Figure 3.20 we found that basins which filled slowly had bed-thickness distributions that were more skewed than those in basins which filled more quickly. The cumulative bed-thickness distributions for these sections based on data that were digitally scanned from *Claps and Masetti* [1994] are presented in Figure 3.21. The model prediction that the skew of the bed thickness distributions increases from the (a) Ra Stua section to the (b) Castagne and (c) Cismon Valley sections is consistent with the data.

IV. VARIABILITY OF THE EARTH'S MAGNETIC FIELD

A. Variations of the dipole moment

As our third and final example we consider the time series of the earth's magnetic field. Paleomagnetic studies show clearly that the polarity of the magnetic field has been subject to reversals. *Kono* [1971] has compiled paleointensity measurements of the magnetic field from volcanic lavas for 0-10 Ma. He concluded that the distribution of paleointensity is well approximated by a symmetric binormal distribution with mean $8.9 \times 10^{22} \text{Am}^2$ and standard deviation $3.4 \times 10^{22} \text{Am}^2$. A normal distribution is applicable to the field when it is in its normal polarity and the other when it is in its reversed polarity.

We have utilized three data sets for computing the power spectrum of the dipole moment of the earth's magnetic field. They are archeomagnetic data from time scales of 100 yr to 8 kyr from *Kovacheva* [1980], marine sediment data from the Somali basin from time scales of 1 kyr to 140 kyr from *Meynadier et al.* [1992], and marine sediment data from the Pacific and Indian Oceans from 20 kyr to 4 Myr from *Meynadier et al.* [1994]. The data

were published in table form in *Kovacheva* [1980] and obtained from L. Meynadier (personal communication, 1995) for the marine sediment data in *Meynadier et al.* [1992] and *Meynadier et al.* [1994]. Marine sediment data are accurate measures of relative paleointensity but give no information on absolute intensity. In order to calibrate marine sediment data, the data must be compared to absolute paleointensity measurements from volcanic lavas sampled from the same time period as the sediment record. *Meynadier et al.* [1994] has done this for the composite Pacific and Indian Ocean data set. They have calibrated the mean paleointensity in terms of the virtual axial dipole moment for 0-4 Ma as $9 \times 10^{22} \text{Am}^2$ [*Valet and Meynadier, 1993*]. This value is consistent with that obtained by *Kono* [1971] for the longer time interval up to 10 Ma. Using this calibration, we calibrated the Somali data with the time interval 0-140 ka from the composite Pacific and Indian Ocean dataset. The data from *Meynadier et al.* [1994] are plotted in Figure 4.1 as a function of age in Ma. The last reversal at approximately 730 ka is clearly shown. We computed the power spectrum of each of the time series with the Lomb periodogram [*Press et al., 1992*]. The compiled spectra are given in Figure 4.2. The composite sediment record from the Pacific and Indian Oceans are plotted up to the frequency $1/(25 \text{ kyr})$. Above this time scale good synchronicity is observed in the Pacific and Indian Ocean data sets [*Meynadier et al., 1994*]. This suggests that non-geomagnetic effects such as variable sedimentation rate are not significant in these cores above this time scale. From frequencies of $1/(25 \text{ kyr})$ to $1/(1.6 \text{ kyr})$ we plot the power spectrum of the Somali data. From time scales of 1.6 kyr to the highest frequency we plot the power spectrum of the data of *Kovacheva* [1980]. A least-squares linear regression to the data yields a slope of -1.09 over 4.5 orders of magnitude. This indicates that the power spectrum is well approximated as $1/f$ on these time scales.

The power spectrum of secular geomagnetic intensity variations has been determined to have a $1/f^2$ power spectrum between time scales of one and 100 years [*Currie, 1968; Barton, 1982; Courtillot and Le Mouel, 1988*]. This is consistent with the analysis of *McLeod* [1992] who found that the first difference of the annual means of geomagnetic field intensity is a white noise since the first differences of a random process with power spectrum $1/f^2$ is a white

noise. Our observation of $1/f$ power-spectral behavior above time scales of approximately 100 yr together with the results of *Currie* [1968] and *Barton* [1982] suggests that there is a crossover from $1/f$ to $1/f^2$ spectral behavior at a time scale of approximately one hundred years.

B. Reversal record

We will now show that the statistics of the reversal record are consistent those with of a binormal $1/f$ noise paleointensity record which reverses each time the intensity crosses the zero value. We will compare the polarity length distribution and the clustering of reversals between synthetic reversals produced with $1/f$ noise intensity variations and the reversal history according to *Harland et al.* [1990] and *Cande and Kent* [1992a,1995].

First we consider the polarity length distribution of the real reversal history. The polarity length distribution calculated from the chronology of *Harland et al.* [1990] is given as the solid line in Figure 4.3. The polarity length distribution is the number of interval lengths longer than the length plotted on the horizontal axis. A reassessment of the magnetic anomaly data has been performed by *Cande and Kent* [1992a,1995] to obtain an alternative magnetic time scale. The polarity length distribution of their time scale normalized to the same length as the *Harland et al.* [1990] time scale, is presented as the dashed curve. The two distributions are nearly identical. These plots suggest that the polarity length distribution is better fit by a power law for large polarity lengths than by an exponential distribution, as first suggested by *Cox* [1968]. The same conclusion has been reached by *Gaffin* [1989] and *Seki and Ito* [1993].

The third curve, plotted with a dashed-dotted line, represents the polarity length distribution estimated from the magnetic time scale between C1 and C13 with “cryptochrons” included and scaled to the length of the *Harland et al.* [1990] time scale. Cryptochrons are small variations recorded in the magnetic anomaly data that may either represent variations in paleomagnetic intensity or short reversals [*Blakely*, 1974; *Cande and Kent*, 1992b]. Cryp-

tochons occur with a time scale at the limit of temporal resolution of the reversal record from magnetic anomalies of the sea floor. The form of the polarity length distribution estimated from the record between C1 and C13 including cryptochrons is not representative of the entire reversal history because of the variable reversal rate which concentrates many short polarity intervals in this time period. However, this distribution enables us to estimate the temporal resolution of the reversal record history. The distribution estimated from C1 to C13 has many more short polarity intervals than those of the full reversal history starting at a reversal length of 0.3 Myr. Above a time scale of 0.3 Myr the magnetic time scale is nearly complete. Below it many short polarity intervals may be unrecorded.

To show that this distribution is consistent with binormal $1/f$ noise intensity variations, we have generated synthetic Gaussian noises with a power spectrum proportional to $1/f$, a mean value of $8.9 \times 10^{22} \text{ Am}^2$ and a standard deviation of $3.4 \times 10^{22} \text{ Am}^2$ as obtained by *Kono* [1971], representative of the field intensity in one polarity state. The synthetic noises were generated using the Fourier-domain filtering technique discussed in MT section 2.1. An example is shown as Figure 4.4. In order to construct a binormal intensity distribution from the synthetic normal distribution, we inverted every other polarity interval to the opposite polarity starting from its minimum value below the zero intensity axis and extending to its next minimum below the zero. The result of this procedure on the Gaussian, $1/f$ noise of Figure 4.4 is presented in Figure 4.5. Its irregular polarity lengths are similar to that in the marine sediment data of Figure 4.1.

The operation of reversing the paleomagnetic intensity when it crosses the zero intensity value is consistent with models of the geodynamo as a system with two symmetric attracting states of positive and negative polarity such as the Rikitake disk dynamo. Between reversals, the geomagnetic field fluctuates until a fluctuation large enough occurs to cross the energy barrier into the other basin of attraction. *Kono* [1987] has explored the statistical similarity between the Rikitake disk dynamo and the distribution of paleointensity. Our construction of the binormal $1/f$ noise is consistent with this model.

We have computed the distributions of lengths between successive reversals for twenty

synthetic noises scaled to length 169 Ma, the length of the reversal chronology, and averaged the results in terms of the number of reversals. The results are plotted as the solid curve along with the *Harland et al.* [1990] time scale (dashed curve) in Figure 4.6. The dots in Figure 4.6 are the maximum and minimum values obtained in the twenty synthetic reversal chronologies for each reversal rank, thus representing 95% confidence intervals. The shape of the synthetic polarity length distribution is very similar to the *Harland et al.* [1990] time scale. The synthetic polarity length distribution matches the *Harland et al.* [1990] time scale within the 95% confidence interval over all time scales plotted except for the Cretaceous superchron, which lies slightly outside of the 95% confidence interval, and reversals separated by less than about 0.3 Myr. The overprediction of very short reversals could be a limitation of the model or a result of the incompleteness of the reversal record for short polarity intervals. As mentioned, the temporal resolution of the magnetic time scale inferred from magnetic anomalies is approximately 0.3 Myr. We conclude that the polarity length distribution produced from binormal $1/f$ intensity variations are consistent with the observed polarity length distribution for all time scales for which the reversal record is complete.

We next consider whether the agreement illustrated in Figure 4.6 is unique to $1/f$ noise. We have computed polarity length distributions using binormal intensity variations with power spectra $f^{-0.8}$ and $f^{-1.2}$. These results along with the $1/f$ result from Figure 4.6 are given in Figure 4.7. The shape of the polarity length distribution is very sensitive to the exponent of the power spectrum. A slight increase in the magnitude of the exponent results in many more long polarity intervals than with $1/f$ noise. We conclude that the agreement in Figure 4.6 between the synthetic reversal distribution and the true reversal history is unique to $1/f$ noise and provides strong evidence that the dipole moment has $1/f$ behavior up to time scales of 170 Myr.

A binormal, $1/f$ noise geomagnetic field variation is consistent with the qualitative results of *Pal and Roberts* [1988] who found an anticorrelation between reversal frequency and paleointensity. This anticorrelation is evident in the synthetic $1/f$ noise of Figure 4.5. During the time intervals of greatest average paleointensity the reversal rate is lowest.

In addition to the broad distribution of polarity lengths, the reversal history is also characterized by a clustering of reversals. This behavior has been quantified with the reversal rate. The reversal rate has been relatively high from 0-20 Ma and has decreased gradually going back in history to the Cretaceous superchron. An alternative approach to quantifying the clustering of reversals is with the pair-correlation function. The pair-correlation function $C(t)$ is the number of pairs of reversals whose separation is between t and $t + \Delta t$, per unit time [Vicsek, 1992]. The pair-correlation function for a set of points can be compared to that for a Poisson process to detect non-random clustering. The pair-correlation function analysis is more appropriate for comparison of the reversal history to the synthetic reversal history generated by a stochastic model since a stochastic model cannot predict behavior in time, such as when the reversal rate is large or small. However, a stochastic model may accurately reflect the extent to which small polarity intervals are followed by small polarity intervals and long intervals by long intervals as quantified with the pair-correlation function.

The pair-correlation function of reversals according to the *Harland et al.* [1990] and *Cande and Kent* [1992a,1995] reversal history are shown in Figure 4.8 as filled and unfilled circles, respectively. Also presented in Figure 4.8 is the pair-correlation function for a synthetic reversal data set based on binormal $1/f$ noise dipole moment variations (boxes) and for a Poisson process (triangles). The functions are offset so that they may be placed on the same graph. The Poisson process was constructed with 293 points, the same number of reversals as the *Harland et al.* [1990] time scale, positioned with uniform probability on the interval between 0 and 170 Ma. The Poisson process yields a correlation function independent of t . The real and synthetic reversal histories variations exhibit significant clustering with more pairs of points at small separation and fewer at large separations than for a Poisson process. Straight-line fits of the form $C(t) \propto t^{-\alpha}$ were obtained. The purpose of this was to show that similar clustering is observed in the real and synthetic reversals. The exponents of the *Harland et al.* [1990], *Cande and Kent* [1992a,1995], and synthetic reversals are -0.39, -0.31, and -0.42, respectively, indicating close agreement between the model and real reversals.

C. Inclination and declination data

Power spectral analyses of inclination and declination data have also been carried out. We obtained time series data for inclination and declination from lake sediment cores in the Global Paleomagnetic Database [Lock and McElhinney, 1992]. The core with the greatest number of data points was from Lac du Bouchet [Thouveny *et al.*, 1990]. The inclination data from this data set is plotted in Figure 4.9. The power spectrum of the inclination and declination at Lac du Bouchet estimated with the Lomb Periodogram is presented in Figure 4.10. We associate the spectra with a flat spectrum below a frequency of $f \approx 1/(3 \text{ kyr})$ and a constant spectrum above a frequency of $f \approx 1/(500 \text{ yr})$. From frequencies of $f \approx 1/(3 \text{ kyr})$ to $f \approx 1/(500 \text{ yr})$ the inclination and declination are Brownian walks with $S(f) \propto f^{-2}$. Spectral analyses of inclination data from five other sediment cores were calculated. These spectra are presented in Figure 4.11. The spectra correspond, from top to bottom, to cores from Anderson Pond [Lund and Banerjee, 1985], Bessette Creek [Turner *et al.*, 1982], Fish Lake [Verosub *et al.*, 1986], Lake Bullenmerri [Turner and Thompson, 1981], and Lake Keilambete [Barton and McElhinny, 1985]. Since the data sets have fewer points there is more uncertainty in the spectra and they are characterized by greater variability between adjacent frequencies. The spectra have the same form, within the uncertainty of the spectra, as that associated with the spectra from Lac du Bouchet. These results suggest that 3 kyr and 500 yr are characteristic time scales of geodynamo behavior. Variations in inclination and declination are associated with changes in the non-dipole components of the field. Therefore, the autocorrelation or decay time of the quadrupole moment is the maximum time scale for correlated fluctuations of inclination and declination to occur. The autocorrelation time of the quadrupole moment has been estimated by McLeod [1996] to be 1.6 kyr. This is within a factor of two of the 3 kyr time scale above which variations in inclination and declination are observed to be uncorrelated in the spectra of Figures 4.10 and 4.11.

Many analyses of variations in paleointensity of the earth's magnetic field concentrate on

identifying characteristic time scales of variation. Many such characteristic time scales have been identified. *Valet and Meynadier* [1993] suggested, based on the same sediment core data analyzed in this paper, that the earth’s magnetic field regenerates following a reversal on a time scale of a few thousand years and then decays slowly on a time scale of 0.5 Myr before the next reversal. They termed this an “asymmetric saw-tooth” pattern. More recent data have shown that the “asymmetric saw-tooth” is not a robust pattern. Longer cores show a slow decay preceding a reversal to be rare [*Tauxe and Hartl*, 1997]. Moreover, *Laj et al.* [1996] has shown that the magnetic field does not always regenerate quickly after a reversal. *Thibal et al.* [1995] have quantified the rate of decrease in field intensity preceding a reversal and found it to be inversely proportional to the length of the polarity interval. The authors concluded from this that the length of the reversal was predetermined. Such behavior is not indicative of a predetermined polarity length. This can be concluded by considering the null hypothesis that variations in the field are characterized by any stationary random process. By definition, a stationary time series has a variance which is independent of the length of the series. The average rate of change of the time series over a time interval will then be a constant value divided by the interval of time, i.e. inversely proportional to time interval. Therefore, any stationary random function satisfies the relationship that *Thibal et al.* [1995] observed.

In the power-spectral analyses of geomagnetic variations inferred from sediment cores performed by *Lund et al.* [1988], *Meynadier et al.* [1992], *Lehman et al.* [1996], and *Tauxe and Hartl* [1997] dominant periodicities in the record were identified and proposed as characteristic time scales of geodynamo behavior. However, it must be emphasized that any finite length record will exhibit peaks in its power spectrum even if the underlying process is random such as a $1/f$ noise. Periodicity tests such as those developed by *Lees and Park* [1995] need to be applied to data in order to assess the probability that a peak in a spectrum is statistically significant. The periodicity tests developed by *Lees and Park* [1995] are especially valuable because they do not depend on a particular model of the stochastic portion of the spectrum. Some of the periodicity tests that have been used in the

geomagnetism literature assume forms for the stochastic portion of the spectrum that are not compatible with the $1/f$ process we have identified. See *Mann and Lees* [1996] for an application of these techniques to climatic time series.

It is generally believed that secular geomagnetic variations are the result of internal dynamics while longer time scale phenomena such as variations in the reversal rate are controlled by variations in boundary conditions at the core-mantle boundary (CMB) [*McFadden and Merrill*, 1995]. However, our observation of continuous $1/f$ spectral behavior from time scales of 100 yr to 170 Myr suggests that a single process controls variations in geomagnetic intensity over this range of time scales. In Section 4.4 we consider a model for geodynamo behavior which reproduces the $1/f$ dipole moment variations over a wide range of time scales and exhibits many of the other features of geomagnetic variability we have identified.

D. Model for geomagnetic variations

There has been great interest in $1/f$ noise processes in the physics literature for many years [*Weissman*, 1988]. One model of $1/f$ noise is a stochastic process comprised of a superposition of modes with exponential decay characterized by different time constants. The time constant for a stochastic process is defined through its autocorrelation function $a(\tau)$. For a stochastic process with a single time constant τ_o the autocorrelation function is given by $a(\tau) = e^{-\frac{\tau}{\tau_o}}$. The power spectrum of such a process is, by the Weiner-Khinchine theorem, the Fourier transform of the autocorrelation function:

$$S(f) \propto \frac{\tau_o}{1 + (2\pi f)^2} \quad (1)$$

This is a Lorentzian spectrum with Brownian walk behavior ($S(f) \propto f^{-2}$) for time scales small compared to τ_o and white noise behavior ($S(f) = \text{constant}$) above the characteristic time constant. If the stochastic process is composed of a superposition of modes with time constants following a distribution $D(\tau_o) \propto \tau_o^{-1}$, where the $D(\tau_o)\Delta\tau_o$ is the net variance contributed by modes between τ_o and $\tau_o + \Delta\tau_o$, then a $1/f$ spectrum results over a range of

frequencies [*van der Ziel*, 1950; *Weissman*, 1988]. Such a distribution of exponential time constants has been documented for the earth’s magnetic field by *McLeod* [1996].

McLeod [1996] calculated the autocorrelation of each degree of the geomagnetic field during the last eighty years. The autocorrelation functions that he computed had an exponential dependence on time with degree-dependent time constants $\tau_o \propto n^{-2}$. This behavior is consistent with a diffusion process. *McLeod* [1996] attributed this autocorrelation structure to a simple model of the geomagnetic field in which the field was stochastically generated with a balance between field regeneration and diffusive decay across a magnetic boundary layer. One way to model such a stochastic diffusion process is with a two-dimensional diffusion equation driven by random noise:

$$\frac{\partial B_z}{\partial t} = D\nabla^2 B_z + \eta(x, y, t) \quad (2)$$

where B_z is the axial component of the magnetic field at a point inside the core and $\eta(x, y, t)$ is a Gaussian white noise representing random amplification and destruction of the field locally by dynamo action. To this equation we add a term equal to $c(p - B_{z,tot})$:

$$\frac{\partial B_z}{\partial t} = D\nabla^2 B_z + \eta(x, y, t) + c(p - B_{z,tot}) \quad (3)$$

where c is a constant, $B_{z,tot}$ is the dipole moment integrated over all space, and p is +1 if the dipole moment of the field outside the core-mantle boundary is positive and -1 if the dipole moment outside the core-mantle boundary is negative. The effect of this term is to create two basins of attraction (polarity states) within which the dipole field fluctuates around an intensity of +1 or -1 until a fluctuation large enough occurs to cross the barrier to the other basin of attraction. This term could be the result of a conservation of magnetic energy for the combination of the poloidal and toroidal fields such that when the poloidal dipole field intensity is low the toroidal field intensity, which is unobservable outside the core and not explicitly modeled in equation 3, is high and dynamo action is intensified, repelling the poloidal field away from a state of low dipole intensity.

In our model the core is modeled as a two-dimensional circular region of uniform diffusivity (the fluid outer core) surrounded by an infinite region with small but finite diffusivity

and the boundary condition that B_z approach zero as r approaches zero where r is the radial distance from the center of the earth. The diameter of the inner circular region is the diameter of the core-mantle boundary.

This model has been simulated by computer using finite differencing of the model equation on a two-dimensional lattice. It has been studied in terms of the distribution of values and power spectrum of the dipole moment and the power spectrum of the angular deviation from the dipole field. The dipole field from the simulation is plotted in Figure 4.12. The field clearly undergoes reversals with a broad distribution of polarity interval lengths. Figure 4.13 represents the dipole distribution of 10 simulations (solid curve) along with the fit to a binormal distribution (dashed curve). A binormal distribution fits the data well. The slight asymmetry is the result of this particular model run spending slightly more time in the negative polarity state than in the positive polarity state. Model outputs were generated which showed asymmetry in the other direction.

The average power spectrum of time series of the dipole field from 25 simulations is presented in Figure 4.14. The spectrum has a low-frequency spectrum $S(f) \propto f^{-1}$ and a high-frequency spectrum $S(f) \propto f^{-2}$. This is identical to the spectrum observed in sediment cores and historical data discussed earlier in the chapter. The crossover time scale is the diffusion time across the diameter of the core, estimated to be between 10^3 yr [Harrison and Huang, 1990] and 10^4 yr [McLeod, 1996]. These values are somewhat higher than the time scale of 10^2 yr identified as the crossover in the sediment core and historical data.

Figure 4.15 shows the average power spectrum of the angular displacement from the dipole from 25 simulations. The spectrum has a high-frequency region $S(f) \propto f^{-2}$ which slowly flattens out to a flat spectrum at low frequencies. This is nearly consistent with the spectra of inclination and declination from lake sediment time series shown in Figures 4.10 and 4.11. The measured value of the crossover from white noise to Brownian walk behavior in the lake sediment power spectra is 3 kyr. This value is consistent with estimates of 10^3 to 10^4 years for the diffusion time across the core from Harrison and Huang [1990] and McLeod [1996]. A major discrepancy between the model and the observed spectrum is the absence

of a flattening out of the spectrum of angular displacement at high frequencies in the model calculation.

V. OTHER APPLICATIONS

Self-affine time series occur in many other areas of Earth science. For example, topographic profiles are Brownian walks [Turcotte, 1987]. Pelletier [1997c] has shown that a model of topography governed by the diffusion equation with the diffusivity a function of discharge predicts both the Brownian walk variations and the log-normal distribution of topography. Branching river networks with statistics identical to those of real river networks were also obtained. Gravity fields also exhibit power-law power spectra [Turcotte, 1987; Passier and Sneider, 1995]. These power spectra have been interpreted as resulting from random density anomalies in the mantle [Lambeck, 1976]. A related problem to the fractal structure of topography which may also exhibit self-affinity is sediment loads in rivers. Plotnick and Prestegard [1993] have obtained time series data for sediment loads in rivers on time scales of minutes to days. They applied both the rescaled-range technique and power-spectral analysis to show that the time series are approximately self-affine.

Tjemkes and Visser [1987] have performed power-spectral analyses on the horizontal variability of temperature, humidity, and cloud water in the atmosphere. They found that different power-law behaviors were applicable over well-defined wave number ranges. These results are important for understanding the variability of the atmosphere and for improved characterization of these fields for inputs into large scale models of the climate system [IPCC, 1995]. The TOPEX/POSEIDON project has provided data on sea surface height with global coverage with a 10-day sampling interval. Wunsch and Stammer [1995] have shown that sea surface height has self-affine behavior in both space and time with three different values of β characterizing the variability over different wave number ranges. Variability in sea surface height has been modeled using the potential vorticity equation with stochastic forcing to represent variable wind conditions [Muller, 1996]. These techniques are very similar to the

stochastic partial differential equations discussed in Sections 2-4. *Hsui et al.* [1993] have shown that sea level variations are a self-affine time series on time scales of 10^4 to 10^8 yr. Since sea level variations determine the major unconformities of the stratigraphic record, the record of the earth's history is determined by self-affine behavior.

Self-affine time series have applications in other fields. It has long been recognized that spatial variations in plankton abundance in the oceans are self-affine. This has been determined by performing power-spectral analysis on remotely-sensed data for plankton along one-dimensional transects [*Platt and Denman*, 1975]. Plankton variability has been modeled using stochastic diffusion equations similar to those presented in this paper [*Fasham*, 1978]. Diffusion is used to model ocean mixing and stochastic terms are introduced to model the effects of local environmental variations that affect the population growth rate such as variations in light intensity and nutrient concentration. Power spectral analyses have also been performed on vegetation densities [*Palmer*, 1988]. The time series were observed to have power-law power spectra. *Sugihara and May* [1990] and *McKinney and Frederick* [1992] have applied the self-affinity of population abundance in time to assessing the probability of extinction. They argued that populations with stronger correlations in variability, characterized by larger values of β or Hu , have greater fluctuations in population size and have a higher probability of extinction.

Self-affine time series with $\beta \approx 1$ are also observed in traffic flows [*Musha and Higuchi*, 1976]. This behavior is reproduced in lattice gas models which move cars around on a lattice according to simple interaction rules that prevent cars from occupying the same space and that are driven by a random input of cars into the lattice [*Takayasu and Takayasu*, 1993]. $1/f$ noise has also been observed in the the density of internet traffic. This observation may have important implications for the design and testing of network software and services.

Alexander, L.L., Geologic evolution and stratigraphic controls on fluid flow of the Eugene Island Block 330 Mini Basin, offshore Louisiana, Ph.D. dissertation, Cornell Univ., Ithaca, N. Y., 1995.

Allen, P.A., and J.R. Allen, *Basin Analysis: Principles and Applications*, Blackwell Sci., Cambridge, Mass., 1990.

Arking, A., and D. Ziskin, Relationship between clouds and sea surface temperatures in the western tropical Pacific, *J. Clim.*, 7, 988, 1994.

Barnett, T.P., A.D. Del Genio, and R.A. Ruedy, Unforced decadal fluctuations in a coupled model of the atmosphere and ocean mixed layer, *J. Geophys. Res.*, 97, 7341-7354, 1992.

Barton, C.C., and C.H. Scholz, The fractal size and spatial distribution of hydrocarbon accumulations: implications for resource assessment and exploration strategy, edited by C.C. Barton and P.R. LaPointe, *Fractals in Petroleum Geology and Earth Sciences*, pp. 13-34, Plenum, New York, 1995.

Barton, C.E., Spectral analysis of palaeomagnetic time series and the geomagnetic spectrum, *Phil. Trans. R. Soc. London A*, 306, 203-209, 1982.

Berg, R.R., Point bar origin of Fall River sandstone reservoirs, northeast Wyoming, *Am. Assoc. Pet. Geol. Bull.*, 52, 2116-2122, 1968.

Blakely, R.J., Geomagnetic reversals and crustal spreading rates during the Miocene, *J. Geophys. Res.*, 79, 2979-2985, 1974.

Booy, C., and L.M. Lye, A new look at flood risk determination, *Water Resour. Bull.*, 25, 933-943, 1989.

Bras, R.L., and I. Rodriguez-Iturbe, *Random Functions and Hydrology*, Addison-Wesley, Reading, Ma., 1985.

Cande, S.C., and D.V. Kent, A new geomagnetic polarity time scale for the Late Cretaceous and Cenozoic, *J. Geophys. Res.*, 97, 13,917-13,951, 1992a.

Cande, S.C., and D.V. Kent, Ultrahigh resolution marine magnetic anomaly profiles : a record of continuous paleointensity variations?, *J. Geophys. Res.*, 97, 15075-15083, 1992b.

Cande, S.C., and D.V. Kent, Revised calibration of the geomagnetic polarity timescale for the Late Cretaceous and Cenozoic, *J. Geophys. Res.*, *100*, 6093-6095, 1995.

Claps, M., and D. Masetti, Milankovitch periodicities recorded in Cretaceous sequences from the Southern Alps (Northern Italy), in *Orbital Forcing and Cyclic Sequences*, edited by P.L. DeBoer and D.L. Smith, pp. 99-107, Blackwell Sci., Cambridge, Mass., 1994.

Coleman, J.M., and D.B. Prior, Deltaic environments of deposition, in *Sandstone Depositional Environments*, edited by P.A. Scholle and D. Spearing, *AAPG Mem.*, *31*, 139-178, 1982.

Courtillot, V., and J.L. Le Mouel, Time variations of the earth's magnetic field: From daily to secular, *Ann. Rev. Earth Plan. Sci.*, *16*, 389-476, 1988.

Cox, A., Lengths of geomagnetic polarity intervals, *J. Geophys. Res.*, *73*, 3247-3260, 1968.

Currie, R.G., Geomagnetic spectrum of internal origin and lower mantle conductivity, *J. Geophys. Res.*, *73*, 2779-2768, 1968.

Curry, W.H., and W.H. Curry III, South Glenrock oil field, Wyoming: A pre-discovery thinking and post-discovery description, in *Stratigraphic Oil and Gas Fields*, edited by R.E. King, *Mem. Am. Assoc. Pet. Geol.*, *15*, 415-427, 1972.

Dacey, M.F., Models of bed formation, *Math. Geol.*, *11*, 655-668, 1979.

Deshpande, A., P.B. Flemings, and J. Huang, Quantifying lateral heterogeneities in fluvio-deltaic sediments using 3-D reflection seismic data: Offshore Gulf of Mexico, *J. Geophys. Res.*, in press, 1997.

Dolan, S.S., C.J. Bean, and B. Riollet, The broad-band fractal nature of heterogeneity in the upper crust from petrophysical logs, submitted, 1996.

Drummond, C.N., and B.H. Wilkinson, Stratal thickness frequencies and the prevalence of orderedness in stratigraphic sequences, *J. Geol.*, *104*, 1-18, 1996.

Dunne, T., K.X. Whipple, and B.F. Aubry, Microtopography of hillslopes and initiation of channels by Horton overland flow, in *Natural and Anthropogenic Influences in Fluvial Geomorphology: The Wolman Volume*, *Geophys. Monogr. Ser.*, vol. 89, edited by J.E.

Costa et al., pp. 27-44, AGU, Washington, D. C., 1995.

Family, F., Scaling of rough surfaces: Effects of surface diffusion, *J. Phys. A Math. Gen.*, *19*, L441-L446, 1986.

Fasham, M. J. R., The statistical and mathematical analysis of plankton patchiness, *Oceanogr. Mar. Biol. Ann. Rev.*, *16*, 43-79, 1978.

Gaffin, S., 1989. Analysis of scaling in the geomagnetic polarity reversal record, *Phys. Earth Plan. Inter.*, **57**, 284-290.

Garcia, R., Depositional systems and their relation to gas accumulation in Sacramento Valley, California, *AAPG Bull.*, *65*, 653-674, 1981.

Garrett, A.E., Vertical eddy diffusivity in the ocean interior, *J. Mar. Res.*, *42*, 359-393, 1984.

Ghil, M., Theoretical climate dynamics: An introduction, in *Turbulence and Predictability in Geophysical Fluid Dynamics and Climate Dynamics*, edited by M. Ghil, North Holland, Amsterdam, 1983.

Gomes da Silva, L.M., and D.L. Turcotte, A comparison between Hurst and Hausdorff measures derived from fractional time series, *Chaos, Solitons and Fractals*, *4*, 2181-2192, 1994.

Harland, W.B., Cox, A., Llewellyn, P.G., Pickton, C.A.G., Smith, A.G. & Walters, R., *A Geologic Time Scale 1989*, Cambridge University Press, London, 1990.

Harrison, C.G.A., and Q. Huang, Q., Rates of change of the Earth's magnetic field measured by recent analyses, *J. Geomag. Geoelectr.*, *42*, 897-928, 1990.

Harvey, L.D.D., and S.H. Schneider, Transient climate response to external forcing on 10^0 - 10^4 year time scales Part I: Experiments with globally averaged, coupled, atmosphere and ocean energy balance models, *J. Geophys. Res.*, *90*, 2191-2205, 1985.

Hays, J.D., J. Imbrie, and N.J. Shackleton, Variations in the earth's orbit: Pacemaker of the ice ages, *Science*, *194*, 1121-1132, 1976.

Hewett, T.A., Fractal distribution of reservoir heterogeneity and their influence of fluid transport, *SPE Prof. Pap.* 15386, Soc. of Pet. Eng., Richardson, Tex., 1986.

Hoffert, M.I., A.J. Callegari, and C.-T. Hsieh, The role of deep sea heat storage in the secular response to climatic forcing, *J. Geophys. Res.*, *85*, 6667-6679, 1980.

Hofmann, D.J., and J.M. Rosen, On the prolonged lifetime of the El Chichon sulfuric acid aerosol cloud, *J. Geophys. Res.*, *92*, 9825-9830, 1987.

Holliger, K., Upper-crustal seismic velocity heterogeneity as derived from a variety of P-wave sonic logs, *Geophys. J. Int.*, *125*, 813-829, 1996.

Hsui, A.T., K.A. Rust, and G.D. Klein, A fractal analysis of Quaternary, Cenozoic-Mesozoic, and late Pennsylvanian sea-level changes, *J. Geophys. Res.*, *98*, 21963-21967, 1993.

Intergovernmental Panel on Climate Change, *Climate Change, The IPCC Scientific Assessment*, edited by J.T. Houghton and B.A. Callendar, Cambridge Univ. Press, New York, 1995.

Janosi, I.M., and G. Vattay, Soft turbulent state of the atmospheric boundary layer, *Phys. Rev. A*, *46*, 6386-6389, 1992.

Jouzel, J., C. Lorius, J.R. Petit, C. Genthon, N.I. Barkov, V.M. Kotlyakov, Vostok ice-core: A continuous isotope temperature record over the last climatic cycle (160,000 years), *Nature*, *329*, 403-407, 1987.

Jouzel, J., and D. Merlivat, Deuterium and oxygen 18 in precipitation: Modeling of the isotopic effects during snow formation, *J. Geophys. Res.*, *89*, 11,749-11,757, 1984.

Kagan, Y.Y., and L. Knopoff, Spatial distribution of earthquakes: The two-point correlation function, *Geophys. J. R. Astron. Soc.*, *62*, 303-320, 1980.

Kendall, D.R., and J.A. Dracup, A comparison of index-sequential and AR(1) generated hydrologic sequences, *J. Hyd.*, *122*, 335-352, 1991.

Kerr, R.A., Climate control: How large a role for orbital variations?, *Science*, *201*, 144-146, 1978.

Kolmogorov, A.N., Solution of a problem in probability theory connected with the problem of the mechanism of stratification, *Trans. Am. Math. Soc.*, *53*, 171-177, 1951.

Kondev, J., and C.L. Henley, Geometrical exponents of contour loops on random gaussian

surfaces, *Phys. Rev. Lett.*, *74*, 4580-4583, 1995.

Kono, M., Intensity of the earth's magnetic field during the Pliocene and Pleistocene in relation to the amplitude of mid-ocean ridge magnetic anomalies, *Earth and Plan. Sci. Lett.*, *11*, 10-17, 1971.

Kono, M., Rikitake two-disk dynamo and paleomagnetism, *Geophys. Res. Lett.*, *14*, 21-24, 1987.

Korvin, G., *Fractal Models in the Earth Sciences*, Elsevier, Amsterdam, 1992.

Kovacheva, M., Summarized results of the archeomagnetic investigation of the geomagnetic field variation for the last 8000 yr in south-eastern Europe, *Geophys. J. R. Astr. Soc.*, *61*, 57-64, 1980.

Laj, C., C. Kissel, and I. Lefevre, Relative geomagnetic field intensity and reversals from Upper Miocene sections in Crete, *Earth Plan. Sci. Lett.*, *141*, 67-78, 1996.

Lambeck, K., Lateral density anomalies in the upper mantle, *J. Geophys. Res.*, *81*, 6333-6340, 1976.

Landwehr, J.M., and N.C. Matalas, On the nature of persistence in dendrochronologic records with implications for hydrology, *J. Hyd.*, *86*, 239-277, 1986.

Lees, J.M., and J. Park, Multiple-taper spectral analysis: A stand-alone C-subroutine, *Computers & Geology*, *21*, 199-236, 1995.

Lehman, B., C. Laj, C. Kissel, A. Mazaud, M. Paterne, and L. Labeyrie, Relative changes of the geomagnetic field intensity during the last 280 kyear from piston cores in the Acores area, *Phys. Earth Plan. Int.*, *93*, 269-284, 1996.

Lock, J., and M.W. McElhinney, The Global Paleomagnetic Database: design, installation, and use with ORACLE, *Surveys in Geophysics*, *12*, 317-506, 1992.

Lund, S.P., and S.K. Banerjee, The paleomagnetic record of Late Quaternary secular variation from Anderson Pond, Tennessee, *Earth Plan. Sci. Lett.*, *72*, 219-237, 1985.

Lund, S.P., J.C. Liddicoat, K.R. Lajoie, T.L. Henyey, and S.W. Robinson, Paleomagnetic evidence for long-term (10^4 year) memory and periodic behavior in the earth's core dynamo process, *Geophys. Res. Lett.*, *15*, 1101-1104, 1988.

Manabe, S., and R.J. Stouffer, Low-frequency variability of surface air temperature in a 1000-year integration of a coupled atmosphere-ocean-land surface model, *J. Climate*, *9*, 376-393, 1996.

Manley, G., Central England temperatures: monthly means 1659-1973, *Quat. J. Roy. Met. Soc.*, *100*, 389-405, 1974.

Mann, M.E., and J.M. Lees, Robust estimation of background noise and signal detection in climatic time series, *Climatic Change*, *33*, 409-445, 1996.

Matteucci, G., Analysis of the probability distribution of the late Pleistocene climatic record: Implications for model validation, *Clim. Dyn.*, *5*, 35-52, 1990.

McFadden, P.L., and R.T. Merrill, History of the Earth's magnetic field and possible connections to core-mantle boundary processes, *J. Geophys. Res.*, *100*, 307-316, 1995.

McKinney, M.L., and D. Frederick, Extinction and population dynamics: New methods and evidence from Paleogene foraminifera, *Geology*, *20*, 343-346, 1992.

McLeod, M.G., Signals and noise in magnetic observatory annual means: Mantle conductivity and jerks, *J. Geophys. Res.*, *97*, 17,261-17,290, 1992.

McLeod, M.G., Spatial and temporal power spectra of the geomagnetic field, *J. Geophys. Res.*, *101*, 2745-2763, 1996.

Meynadier, L., J.-P. Valet, F.C. Bassonot, N.J. Shackleton, and Y. Guyodo, Asymmetrical saw-tooth pattern of the geomagnetic field intensity from equatorial sediments in the Pacific and Indian oceans, *Earth Plan. Sci. Lett.*, *126*, 109-127, 1994.

Meynadier, L., J.-P. Valet, R. Weeks, N.J. Shackleton, and V.L. Hagee, Relative geomagnetic intensity of the field during the last 140 ka, *Earth Plan. Sci. Lett.*, *114*, 39-57, 1992.

Mitchell Jr., J.M., An overview of climatic variability and its causal mechanisms, *Quat. Res.*, *6*, 481-493, 1976.

Mizutani, S., and I. Hattori, Stochastic analysis of bed-thickness distribution of sediments, *Math. Geol.*, *4*, 123-146, 1972.

Molz, F.J., and G.K. Boman, A fractal-based stochastic interpolation scheme in subsur-

face hydrology, *Water Resour. Res.*, *29*, 3769-3774, 1993.

Muller, P., Stochastic forcing of quasi-geostrophic eddies, in *Stochastic Modelling in Physical Oceanography*, edited by R. J. Adler, P. Muller, and B. Rozovskii, pp. 381-395, Birkhauser, Boston, 1996.

Musha, T., and H. Higuchi, The $1/f$ fluctuation of a traffic current of an expressway, *Jap. J. Appl. Phys.*, *15*, 1271-1275, 1976.

Muto, T., The Kolmogorov model of bed thickness distribution: An assessment based on numerical simulation and field-data analysis, *Terra Nova*, *7*, 408-416, 1995.

National Geophysical Data Center, *Global Paleomagnetic Database, version 3.1*, National Oceanographic and Atmospheric Administration, 1995.

Noakes, D.J., K.W. Hipel, A.I. McLeod, C. Jimenez, and S. Yakowitz, Forecasting annual geophysical time series, *Int. J. Forecasting*, *4*, 103-115, 1988.

North, G.R., and R.F. Cahalan, Predictability in a solvable stochastic climate model, *J. Atm. Sci.*, *38*, 504-513, 1981.

Novikov, E.A., Random force method in turbulence theory, *Soviet Phys., J.E.T.P.*, *17*, 1449-1454, 1963.

Pal, P.C., and P.H. Roberts, Long-term polarity stability and strength of the geomagnetic dipole, *Nature*, *331*, 702-705, 1988.

Palmer, M.W., Fractal geometry: A tool for describing spatial patterns of plant communities, *Vegetatio* *75*, 91-102, 1988.

Passier, M.L., and R.K. Snieder, On the presence of intermediate-scale heterogeneity in the upper mantle, *Geophys. J. Int.*, *123*, 817-837, 1995.

Peixoto, J.P., and A.H. Oort, *Physics of Climate*, Am. Inst. Phys., New York, 1992.

Pelletier, J.D., Variations in solar luminosity from time scales of minutes to months, *Astrophys. J.*, *463*, L41-L45, 1996.

Pelletier, J.D., Analysis and modeling of the natural variability of climate, *J. Climate*, *10*, 1331-1342, 1997a.

Pelletier, J.D., Kardar-Parisi-Zhang scaling of the convective boundary layer and the

- fractal structure of cumulus cloud fields, *Phys. Rev. Lett.*, 78, 2672-2675, 1997b.
- Pelletier, J.D., Why is topography fractal?, *J. Geophys. Res.*, submitted, 1997c.
- Pelletier, J.D., and D.L. Turcotte, Scale-invariant topography and porosity variations in sedimentary basins, *J. Geophys. Res.*, 101, 28,165-28,175, 1996.
- Pilkington, M., and J.P. Todoeschuck, Stochastic inversion for scaling geology, *Geophys. J. Int.*, 102, 205-217, 1990.
- Platt, T., and K.L. Denman, Spectral analysis in ecology, *Ann. Rev. Ecol. Syst.*, 6, 189-210, 1975.
- Pleune, R., Vertical diffusion in the stable atmosphere, *Atm. Env. A*, 24, 2547-2555, 1990.
- Plotnick, R.E., A fractal model for the distribution of stratigraphic hiatuses, *J. Geol.*, 94, 885-890, 1986.
- Plotnick, R.E., and K. Prestegard, Fractal analysis of geologic time series, in *Fractals in Geography*, edited by L. De Cola and S. Lam, pp. 193-210, Prentice-Hall, Englewood Cliffs, Cal., 1993.
- Press, W.H., S.A. Teukolsky, W.T. Vetterling, and B.P. Flannery, *Numerical Recipes in C: The Art of Scientific Computing*, 2nd ed., Cambridge Univ. Press, New York, 1992.
- Rosen, J.M., N.T. Kjome, R.T. McKenzie, and J.B. Liley, Decay of Mount Pinatubo aerosols at midlatitudes in the northern and southern hemispheres, *J. Geophys. Res.*, 99, 25,733-25,739, 1994.
- Rothman, D.H., J. Grotzinger, and P. Flemings, Scaling in turbidite deposition, *J. Sed. Petrol. A*, 64, 59-67, 1993.
- Sadler, P.M., Sediment accumulation rates and the completeness of stratigraphic sections, *J. Geol.*, 89, 569-584, 1981.
- Sadler, P.M., and D.J. Strauss, Estimation of completeness of stratigraphical sections using empirical data and theoretical methods, *J. Geol. Soc. London*, 147, 471-485, 1990.
- Schwarzacher, W., *Sedimentation Models and Quantitative Stratigraphy*, Elsevier, Amsterdam, 1975.

Seinfeld, J.H., *Atmospheric Chemistry and Physics of Air Pollution*, Wiley, New York, 1986.

Seki, M. and K. Ito, A phase-transition model for geomagnetic polarity reversals, *J. Geomag. Geoelectr.*, *45*, 79-88, 1993.

Shiomi, K., H. Sato, and M. Ohtake, Broad-band power-law spectra of well-log data in Japan and the effects on seismic wave propagation, *Geophys. J. Int.*, in press, 1997.

Slack, J.R., J.M. Landwehr, Hydro-climatic data network: A U.S. Geological Survey streamflow data set for the United States for the study of climatic variations: 1874-1988, *U.S. Geol. Surv. Open-File Rep. 92-129*, 1992.

Stevenson, D.J., Planetary magnetic fields, *Rep. Prog. Phys.*, *46*, 555-620, 1983.

Strauss, D.J., and P.M. Sadler, Stochastic models for the completeness of stratigraphic sections, *Math. Geol.*, *21*, 37-59, 1989.

Sugihara, G., and R.M. May, Applications of fractals in ecology, *Trends in Ecol. Evol.* *5*, 79-86, 1990.

Takayasu, M., and H. Takayasu, $1/f$ noise in a traffic model, *Fractals*, *1*, 860-866, 1993.

Tarboton, D.G., The source hydrology of severe sustained drought in the Southwestern United States, *J. Hyd.*, *161*, 31-69, 1994.

Tauxe, L., and P. Hartl, 11 million years of Oligocene geomagnetic field behavior, *Geophys. J. Int.*, *128*, 217-229, 1997.

Thibal, J., J.-P. Pozzi, V. Barthes, and G. Dubuisson, Continuous record of geomagnetic field intensity between 4.7 and 2.7 Ma from downhole measurements, *Earth Plan. Sci. Lett.*, *136*, 541-550, 1995.

Thouveny, N., K.M. Creer, and I. Blunk, Extension of the Lac du Bouchet palaeomagnetic record over the last 120,000 years, *Earth Plan. Sci. Lett.*, *97*, 140-161, 1990.

Tipper, J.C., Rates of sedimentation, and stratigraphical completeness, *Nature*, *21*, 296-298, 1983.

Tjemkes, S.A., and M. Visser, Horizontal variability of temperature, specific humidity, and cloud liquid water as derived from spaceborne observations, *J. Geophys. Res.*, *99*,

23,089-23,105, 1994.

Todoeschuck, J.P., O.G. Jensen, and S. Labonte, Gaussian scaling noise model of seismic reflection sequences: evidence from well logs, *Geophysics*, *55*, 480-484, 1990.

Tubman, K.M., and S.D. Crane, Vertical versus horizontal well log variability and application to fractal reservoir modeling, in *Fractals in Petroleum Geology and Earth Sciences*, edited by C.C. Barton and P.R. LaPointe, pp. 279-294, Plenum, New York, 1995.

Turcotte, D.L., A fractal interpretation of topography and geoid spectra on the Earth, Moon, Venus, and Mars, *J. Geophys. Res.*, *92*, 597-601, 1987.

Turcotte, D.L., *Fractals and Chaos in Geology and Geophysics*, Cambridge Univ. Press, New York, 1992.

Turner, G.M., and R. Thompson, Lake sediment record of the geomagnetic secular variation in Britain during Holocene times, *Geophys. J. R. Astron. Soc.*, *65*, 703-725, 1981.

Valet, J.-P., L. Meynadier, Geomagnetic field intensity and reversals during the past four million years, *Nature*, *366*, 234-238, 1993.

van der Ziel, A., On the noise spectra of semiconductor noise and of flicker effect, *Physica*, *16*, 359-375, 1950.

Van Kampen, N.G., *Stochastic Processes in Physics and Chemistry*, North-Holland, Amsterdam, 1981.

Van Vliet, K.M., A. van der Ziel, and R.R. Schmidt, Temperature-fluctuation noise of thin films supported by a substrate, *J. Appl. Phys.*, *51*, 2947-2956, 1980.

Verosub, K.L., P.J. Mehringer, and P. Waterstraat, Holocene secular variation in western North America: paleomagnetic record from Fish Lake, Harney County, Oregon, *J. Geophys. Res.*, *91*, 3609-3623, 1986.

Vicsek, T., *Fractal Growth Phenomena*, World Sci., River Edge, N. J., 1992.

Vistelius, A.B., and T.S. Feigel'son, On the theory of bed formation, *Dokl. Akad. Nauk. SSSR*, *164*, 158-160, 1965.

Voorhies, C.V., and J. Conrad, Accurate predictions of mean geomagnetic dipole excursion and reversal frequencies, mean paleomagnetic field intensity, and the radius of the

Earth's core using McLeod's rule, *NASA Technical Memorandum 104634*, 1996.

Vose, R.S., R.L. Schmoyer, P.M. Stewer, T.C. Peterson, R. Heim, T.R. Karl, and J.K. Eischeid, The global historical climatology network: Long-term monthly temperature, precipitation, sea-level pressure, and station pressure data, *Envir. Sci. Div. Pub. No. 392*, Oak Ridge National Laboratory, 1992.

Voss, R.F., and J. Clarke, Flicker ($1/f$) noise: Equilibrium temperature and resistance fluctuations, *Phys. Rev. B*, *13*, 556-573, 1976.

Walden, A.T., and J.W.J. Hosken, An investigation of the spectral properties of primary reflection coefficients, *Geophys. Prospect.*, *33*, 400-435, 1985.

Wallis, J.R., D.P. Lettenmaier, and E.F. Wood, A daily hydroclimatological data set for the continental U.S., *Water Resour. Res.*, *27*, 1657-1663, 1991.

Weissman, M.B., $1/f$ noise and other slow, nonexponential kinetics in condensed matter, *Rev. Mod. Phys.*, *60*, 537-571, 1988.

Wilde, P., W.R. Normark, and T.E. Chase, Channel sands and petroleum potential of Monterey deep-sea fan, California, *AAPG Bull.*, *62*, 967-983, 1978.

Wunsch, C., and D. Stammer, The global frequency-wavenumber spectrum of oceanic variability estimated from TOPEX/POSEIDON altimetric measurements, *J. Geophys. Res.*, *100*, 24,895-24,910, 1995.

Yiou, P., J. Jouzel, S. Johnsen, and O.E. Rognvaldsson, Rapid oscillations in Vostok and GRIP ice cores, *Geophys. Res. Lett.*, *22*, 2179-2182, 1995.

FIGURE CAPTIONS

Figure 2.1: Atmospheric temperatures at Vostok, Antarctica inferred from Deuterium concentrations in the Vostok ice core [Jouzel *et al.*, 1987].

Figure 2.2: Power-spectral density estimated with the Lomb periodogram of the temperature inferred from the Deuterium concentrations in the Vostok (East Antarctica) ice core. The power-spectral density S is given as a function of frequency for time scales of 500 yr to 200 kyr.

Figure 2.3: Average monthly atmospheric temperature for Central England [Manley [1974] with the yearly periodicity removed.

Figure 2.4: Power-spectral density of the time series of Central England temperatures in Figure 2.3.

Figure 2.5: Average power-spectral density of 94 complete monthly temperature time series from the dataset of the Vose *et al.* [1992] plotted as a function of frequency in yr^{-1} . The power-spectral density S is given as a function of frequency for time scales of 2 months to 100 yr.

Figure 2.6: Average power-spectral density of 50 continental daily temperature time series from the data set of the *National Climatic Data Center* [1994] as a function of frequency in yr^{-1} . The power-spectral density S is given as a function of frequency for time scales of 2 days to 10 yr.

Figure 2.7: Average power-spectral density of 50 maritime daily temperature time series from the data set of the *National Climatic Data Center* [1994] as a function of frequency in yr^{-1} . The power-spectral density S is given as a function of frequency for time scales of 2 days to 10 yr.

Figure 2.8: Power-spectral density of local atmospheric temperature from instrumental data and inferred from ice cores from time scales of 200 kyr to 2 days. The high frequency data are for continental stations. Piecewise power-law trends are indicated.

Figure 2.9: Average normalized power-spectral density of 636 monthly river discharge

series as a function of frequency in yr^{-1} .

Figure 2.10: Average normalized power-spectral density of 43 tree ring chronologies in the western U.S. as a function of frequency in yr^{-1} .

Figure 2.11: Average power-spectral density of the number of random walkers in the central site of a lattice. The average of 50 simulations is presented.

Figure 2.12: Cumulative distribution function of the time series produced by the stochastic diffusion model (solid circles). The curve represents the cumulative log-normal distribution function fit to the data.

Figure 2.13: (a) Geometry of the one-dimensional diffusion calculation detailed in the text. (b) Boundary conditions appropriate to the air masses above the ocean (maritime stations), where the ocean acts as a thermal conductor. (c) Boundary conditions appropriate to the air masses above the continents (continental stations), where the continents act as a thermal insulator.

Figure 2.14: Geometry of the coupled atmosphere-ocean model and the constants chosen.

Figure 2.15: Average power-spectral density of atmospheric temperature above continents and oceans for each grid point in the general circulation model calculations of *Manabe and Stouffer* [1996]. The straight-line corresponding to $f^{-\frac{1}{2}}$ is included for comparison.

Figure 2.16: Power spectral density of variations in the solar irradiance in 1987 and 1985 from the ACRIM project as a function of frequency in hour^{-1} .

Figure 2.17: Logarithm (base 10) of the recurrence interval as a function of drought duration and magnitude (normalized to the mean annual flow) for a log-normal distribution with coefficient of variation (a) 0.2, (b) 0.4, and (c) 0.6.

Figure 3.1: Illustration of the sediment deposition model. In each case a site is chosen randomly (the center of the three sites in each of the above pictures). The dashed block is the unit of sediment being added to the surface. The arrows point toward the site upon which the unit of sediment will be deposited. (a) The chosen site has a lower elevation than either of its nearest neighbors, so the sediment is deposited at the chosen site. (b) One of the nearest neighboring sites has a lower elevation and the sediment is deposited at that

lower site. (c) In the case of a tie for the lowest elevation between two or three sites, the site on which the sediment is deposited is chosen randomly between the sites of the same elevation.

Figure 3.2: A typical surface produced by the deposition model with 1024 grid points.

Figure 3.3: Average power spectrum of the surfaces constructed from fifty independent simulations on 1024 grid points as a function of the wave number k . The model surfaces are Brownian walks.

Figure 3.4: One-dimensional transect of hillslope topography perpendicular to the channel dip. Obtained with the use of laser altimetry [*Dunne, Whipple, and Aubry, 1995*].

Figure 3.5: Difference from the mean height of the central site of the lattice as a function of time.

Figure 3.6: Average power spectrum of the difference from the mean height of the central site for fifty independent simulations as a function of frequency f . The power spectrum is proportional to $f^{-\frac{3}{2}}$.

Figure 3.7: Vertical porosity well log from the Gulf of Mexico.

Figure 3.8: Power spectral density of porosity as a function of wave number in units of m^{-1} in fifteen wells from the Gulf of Mexico. The spectra are offset so that they may be placed on the same graph.

Figure 3.9: Probability density function for elevation of topographic transects from [*Dunne et al., 1995*].

Figure 3.10: Wells producing hydrocarbons in the (a) Powder River and (b) Denver basins [*Barton and Scholz, 1995*]. Distance units are scaled such that the basin is 128 x 128.

Figure 3.11: Pair-correlation function of the Powder River and Denver basins as a function of the pair separation.

Figure 3.12: Synthetic reservoir constructed from a source and cap rock with a two-dimensional Brownian walk topography constructed on a 128 x 128 grid where all the sites with porosity greater than a fixed level are showing.

Figure 3.13: Pair-correlation functions for synthetic reservoirs with caprocks constructed

with different values of β . The plots are offset so that they may be placed on the same graph.

Figure 3.14: The nondimensional thickness of sediments $h\sigma/D$ in a sedimentary basin is given as a function of nondimensional time $t\sigma^2/D$ for a sequence in which the ratio of the standard deviation to the mean of sedimentation, $\sigma/\bar{\eta}$ is 0.1.

Figure 3.15: For the model given in Figure 3.14 the age of the sediments is given as a function of depth. Only those sediments which are not later eroded are preserved.

Figure 3.16: Illustration of a model for sediment deposition based on a Devil's staircase associated with a second-order Cantor set. (a) Age of sediments T as a function of depth y . (b) Illustration of how the Cantor set is used to construct the sedimentary pile. (c) Average rate of deposition R as a function of the period T considered.

Figure 3.17: Average rate of sedimentation, $R/\bar{\eta}$, as a function of time span, $T\sigma^2/D$, for the sediment column of Figure 3.10(b).

Figure 3.18: Observed sedimentation rates as a function of time span from the data of *Sadler* [1995]. The data have been binned in equally-spaced bins in log space. A least-square linear fit to the logarithms of the data yields a slope of $-\frac{3}{4}$ indicating that $R \propto T^{-\frac{3}{4}}$.

Figure 3.19: Cumulative frequency-length distribution of hiatuses, the number of hiatuses longer than nondimensional hiatus length $t_h\sigma^2/D$, for synthetic sequences produced with the stochastic diffusion model.

Figure 3.20: Cumulative frequency-thickness distribution of nondimensional bed thicknesses for synthetic sediment columns with $\sigma/\bar{\eta} = 0.1, 0.01, 0.001$ and 0.0003 . The distributions are exponential.

Figure 3.21: Cumulative frequency-thickness distribution of bed thicknesses of deep-sea sequences from (a) Ra Stua, (b) Castagne, and (c) Cismon Valley, Italy published in *Claps and Masetti* [1994]. The coefficients in the exponential distributions determined by a least-squares fit of the logarithm of the bed number to the bed thickness for the largest forty beds were $-0.052, -0.166,$ and -0.252 , showing an increasing trend with sedimentation rate consistent with the model behavior.

Figure 4.1: Paleointensity of the virtual axial dipole moment (VADM) of the earth's

magnetic field (with reversed polarity data given by negative values) inferred from sediment cores for the past 4 Ma from *Meynadier* [1994].

Figure 4.2: Power spectral density of the geomagnetic field intensity variations estimated from the Lomb periodogram of sediment cores from *Meynadier* [1992] and *Meynadier* [1994] and archeomagnetic data from *Kovacheva* [1980]. The power-spectral density S is given as a function of frequency f for time scales of 100 yr to 4 Myr.

Figure 4.3: Cumulative frequency-length distribution of the lengths of polarity intervals from the time scale of *Harland et al.* [1990] (solid curve), *Cande and Kent* [1992a,1995] (dashed curve), and the *Cande and Kent* [1992a,1995] time scale from C1 to C13 with cryptochrons included (dashed-dotted line).

Figure 4.4: A $1/f$ noise with a normal distribution with mean of 8.9 and standard deviation of $3.4 \times 10^{22} \text{Am}^2$ representing the geomagnetic field intensity in one polarity state.

Figure 4.5: Binormal $1/f$ noise constructed from the normal $1/f$ noise of Figure 4.4 as described in the text.

Figure 4.6: Cumulative frequency-length polarity interval distributions from the *Harland et al.* [1990] time scale and that of the binormal $1/f$ noise model of intensity variations. The distribution from the *Harland et al.* [1990] time scale is the dashed curve. The solid line is the average cumulative distribution from the $1/f$ noise model. The dotted lines represent the minimum and maximum reversal length distributions for 20 numerical experiments, thereby representing 95% confidence intervals.

Figure 4.7: Cumulative frequency-length polarity interval distributions for the $1/f$ noise model of intensity variations (shown in the middle, the same as that in Figure 4.6) and for intensity variations with power spectra proportional to $f^{-0.8}$ and $f^{-1.2}$. This plot illustrates that the polarity length distribution is very sensitive to the form of the power spectrum, allowing us to conclude that the agreement between the model and the observed distribution in Figure 4.5 is unique to $1/f$ noise intensity variations.

Figure 4.8: Pair-correlation function of the reversal history according to the *Harland et al.* (1990) time scale (filled circles), *Cande and Kent* (1992a,1995) (unfilled circles),

synthetic reversals produced from $1/f$ noise model of intensity variations (boxes), and a Poisson process (triangles). The real and synthetic reversals exhibit similar non-random clustering.

Figure 4.9: Magnetic field inclination inferred from the Lac du Bouchet sediment core [Thouveny *et al.*, 1990].

Figure 4.10: Power spectra of inclination and declination from the Lac du Bouchet sediment core. The declination spectrum is offset from the inclination spectrum so that they may be placed on the same graph.

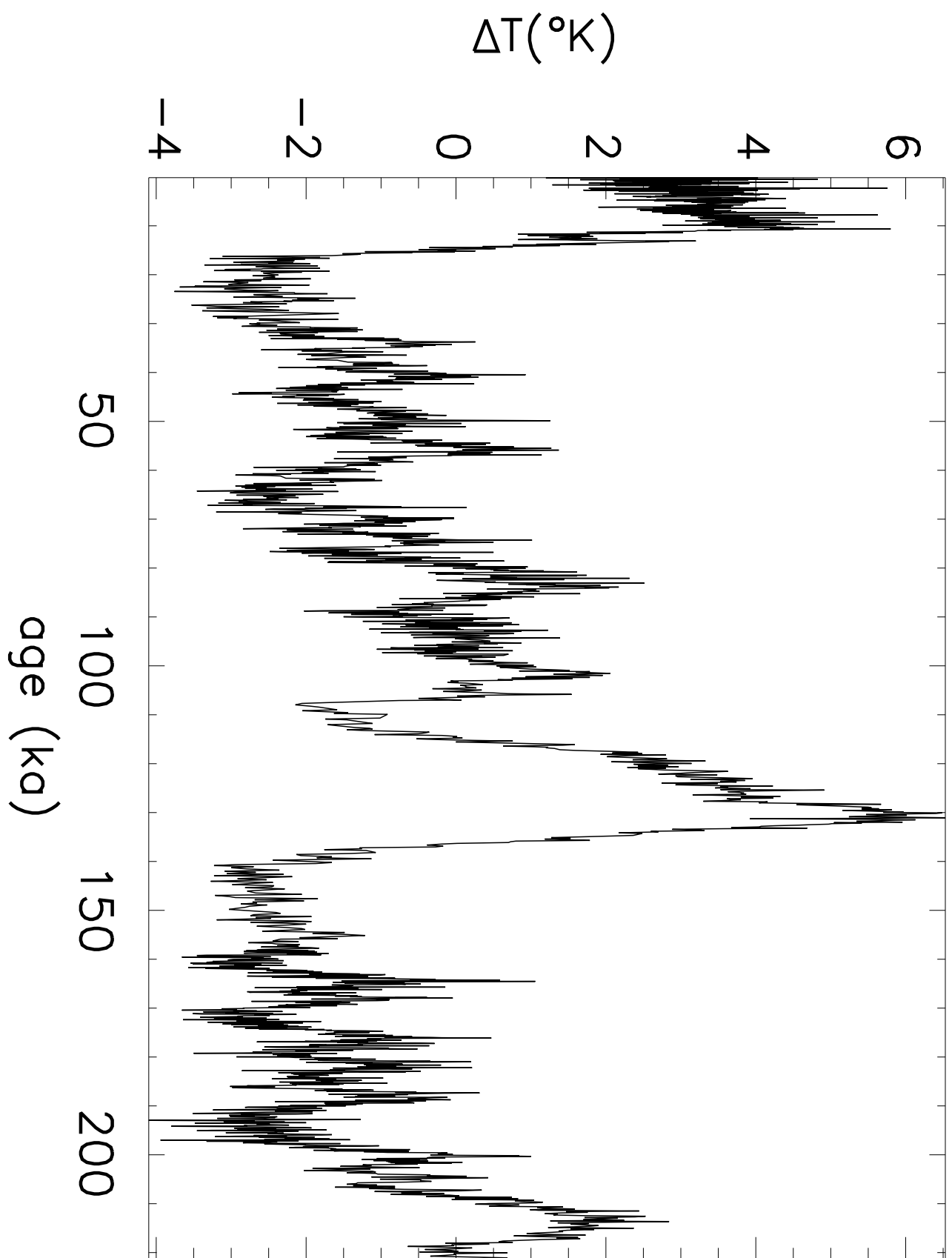
Figure 4.11: Power spectra of inclination from the following locations, top to bottom: 1) Anderson Pond, 2) Bessette Creek, 3) Fish Lake, 4) Lake Bullenmerri, and 5) Lake Keilambete. The spectra are offset to place them on the same graph.

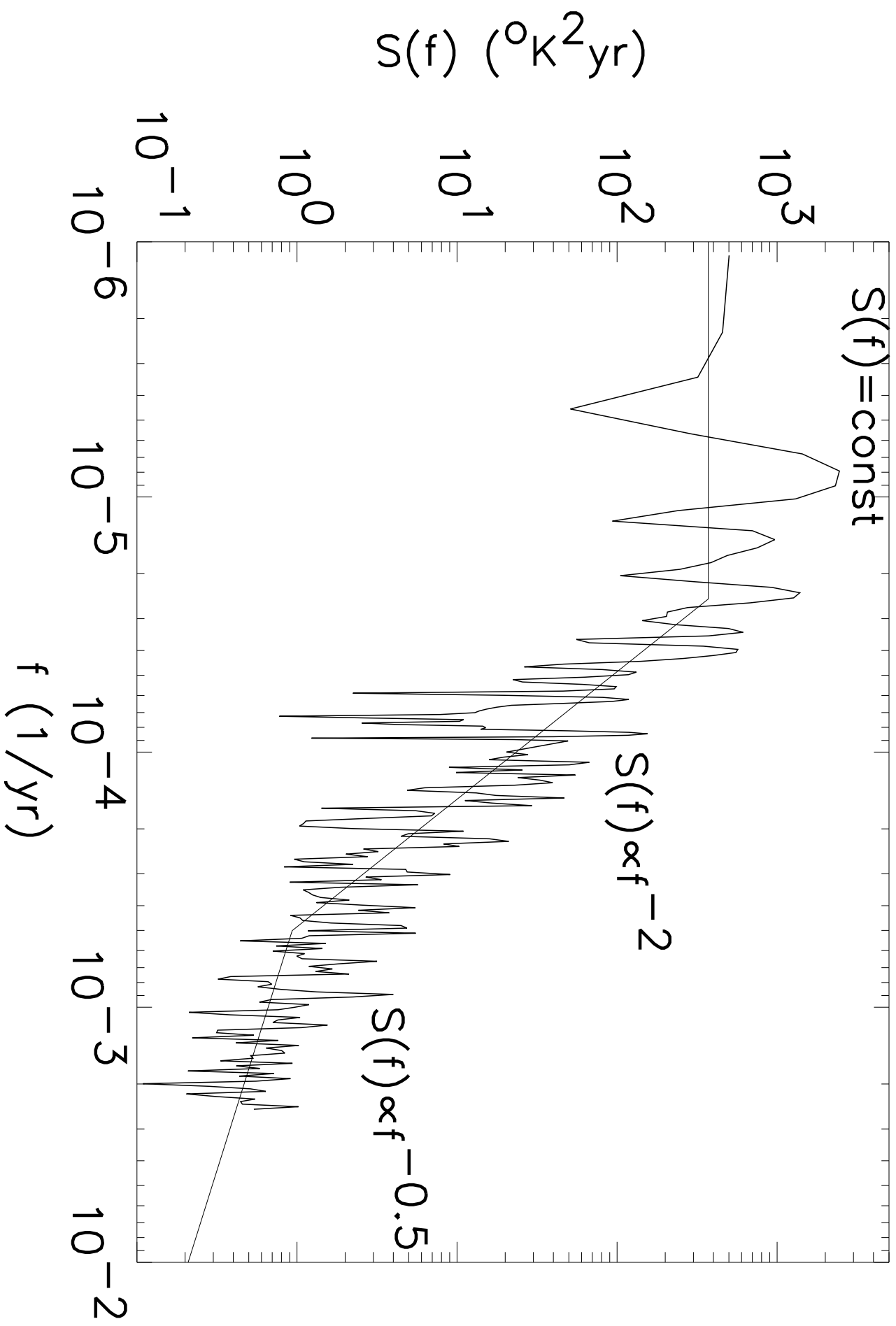
Figure 4.12: Dipole moment produced by the model for geomagnetic variations normalized to the average dipole moment, set to be one. The field exhibits reversals with a broad distribution of polarity interval lengths and a variable reversal rate decreasing at later times in the simulation.

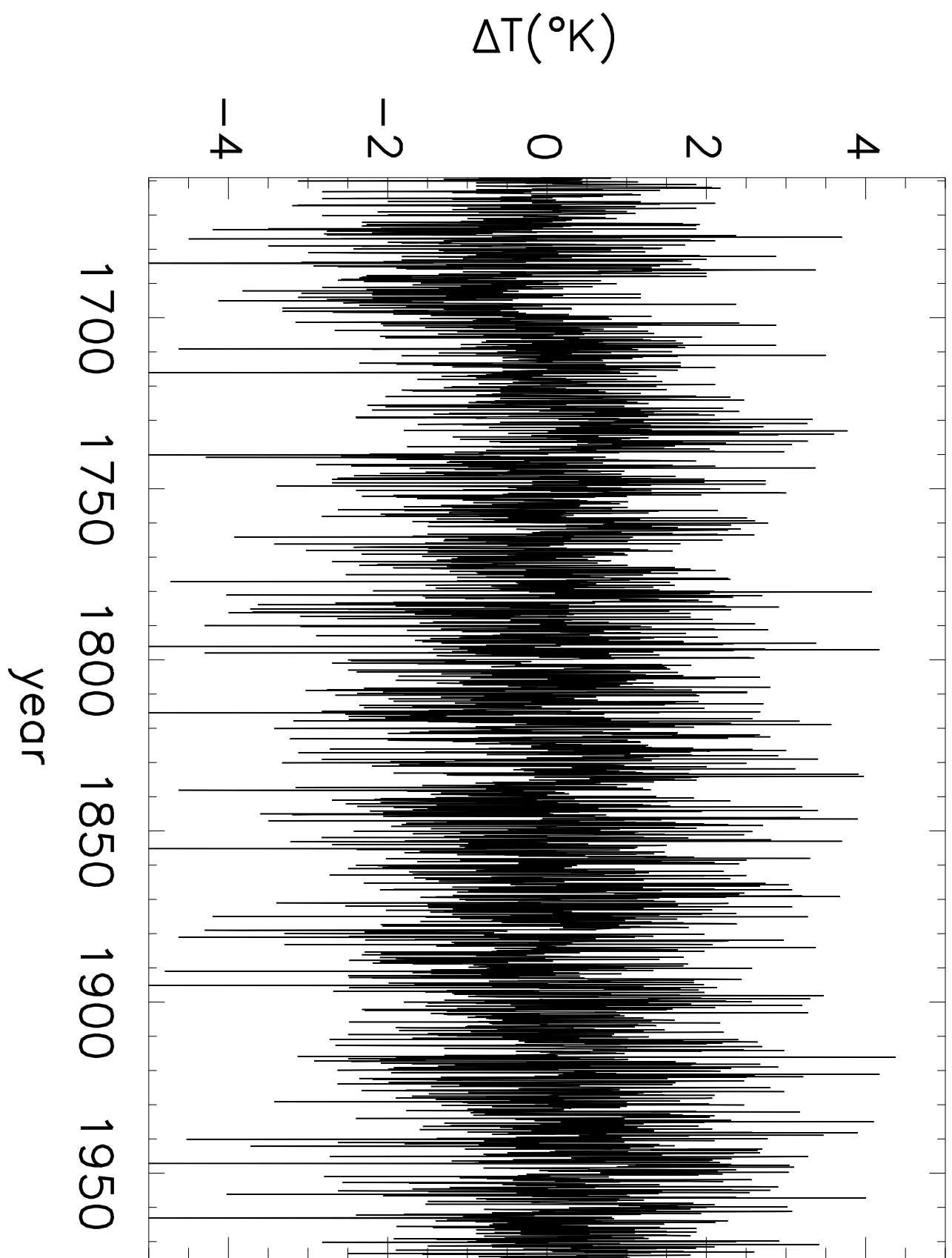
Figure 4.13: Distribution of the magnetic field according to ten simulations of the model (solid curve) and a binormal distribution fit to the data (dashed line). The binormal distribution fits the data well.

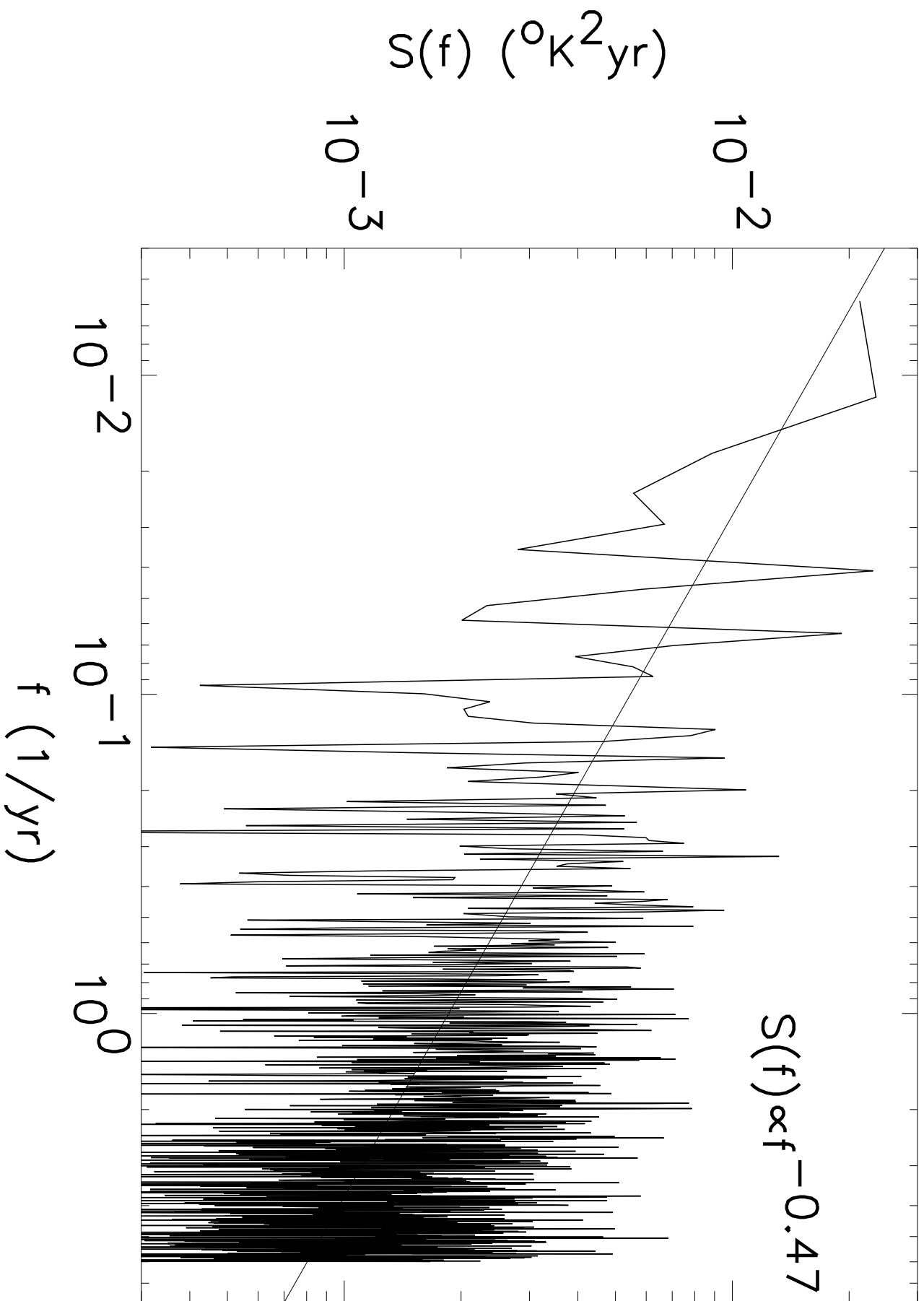
Figure 4.14: Average power spectrum of the mean value of the magnetic field (dipole field) from 25 simulations. The spectrum has a low-frequency spectrum with $S(f) \propto f^{-1}$ and a high frequency region $S(f) \propto f^{-2}$. The same spectrum is observed in geomagnetic intensity from sediment cores and historical data.

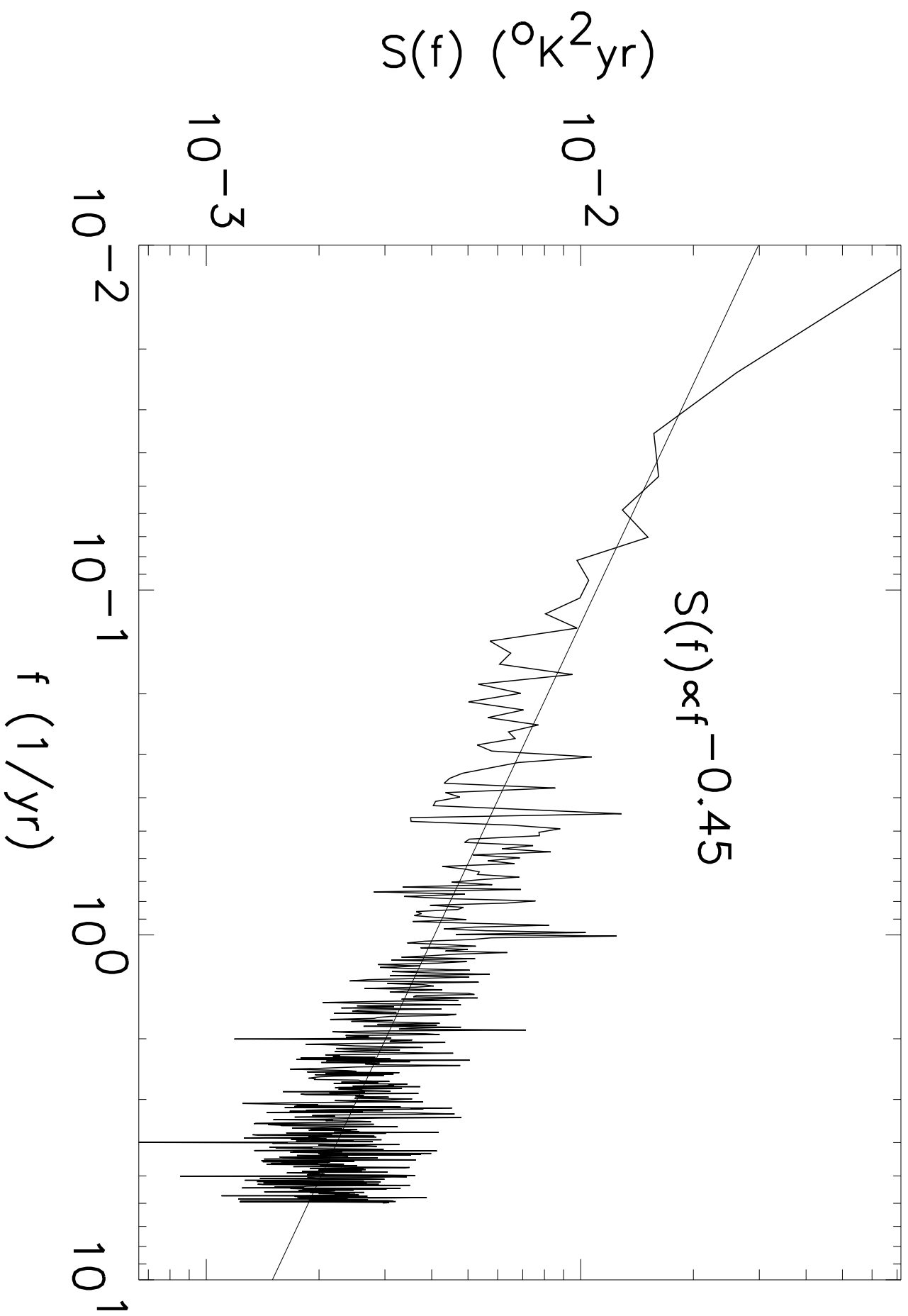
Figure 4.15: Average power spectrum of the angular deviation from a dipole field from 25 simulations. The spectrum is $S(f) \propto f^{-2}$ for high frequencies and gradually flattens out to a constant spectrum at low frequencies.

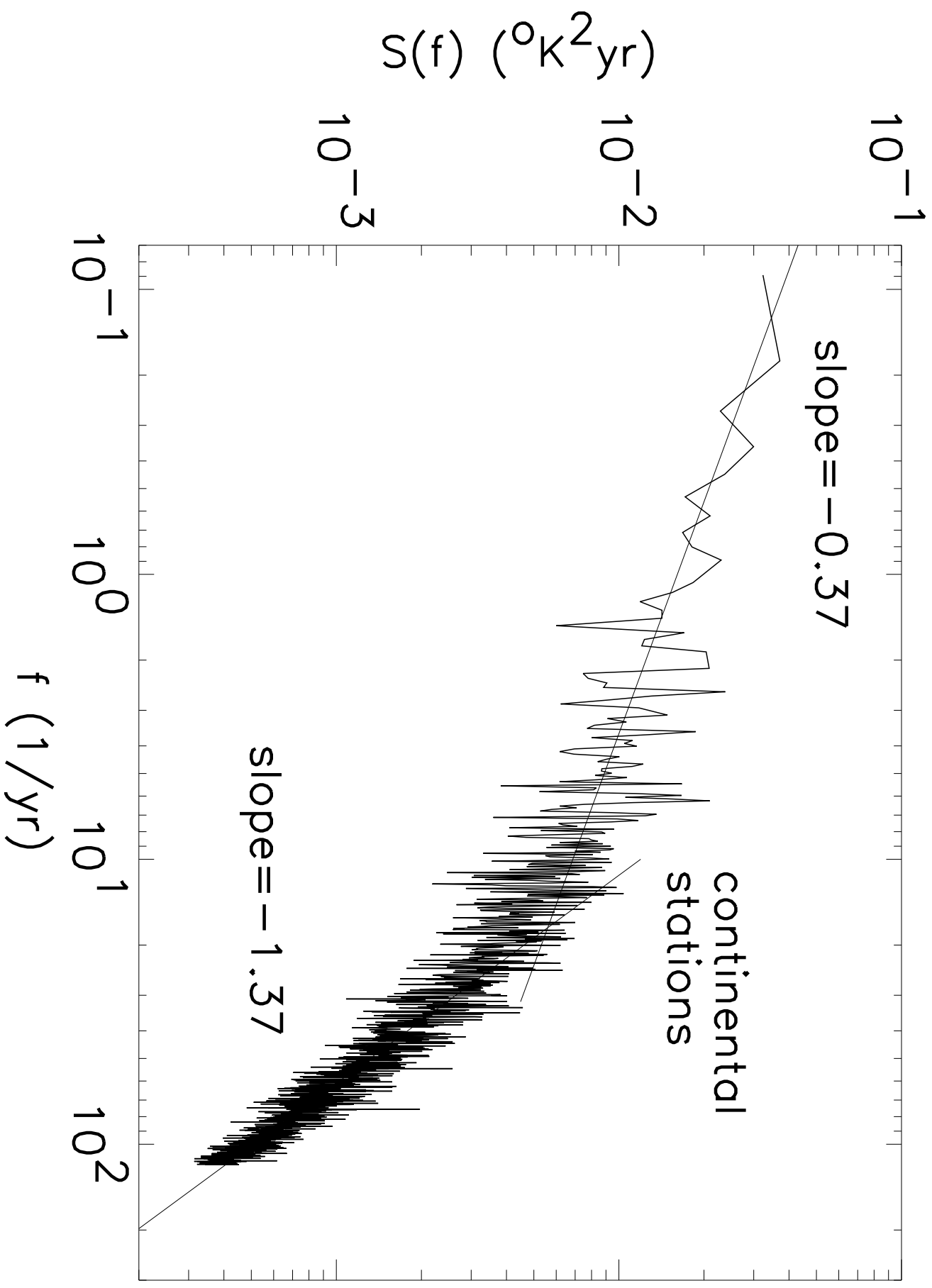


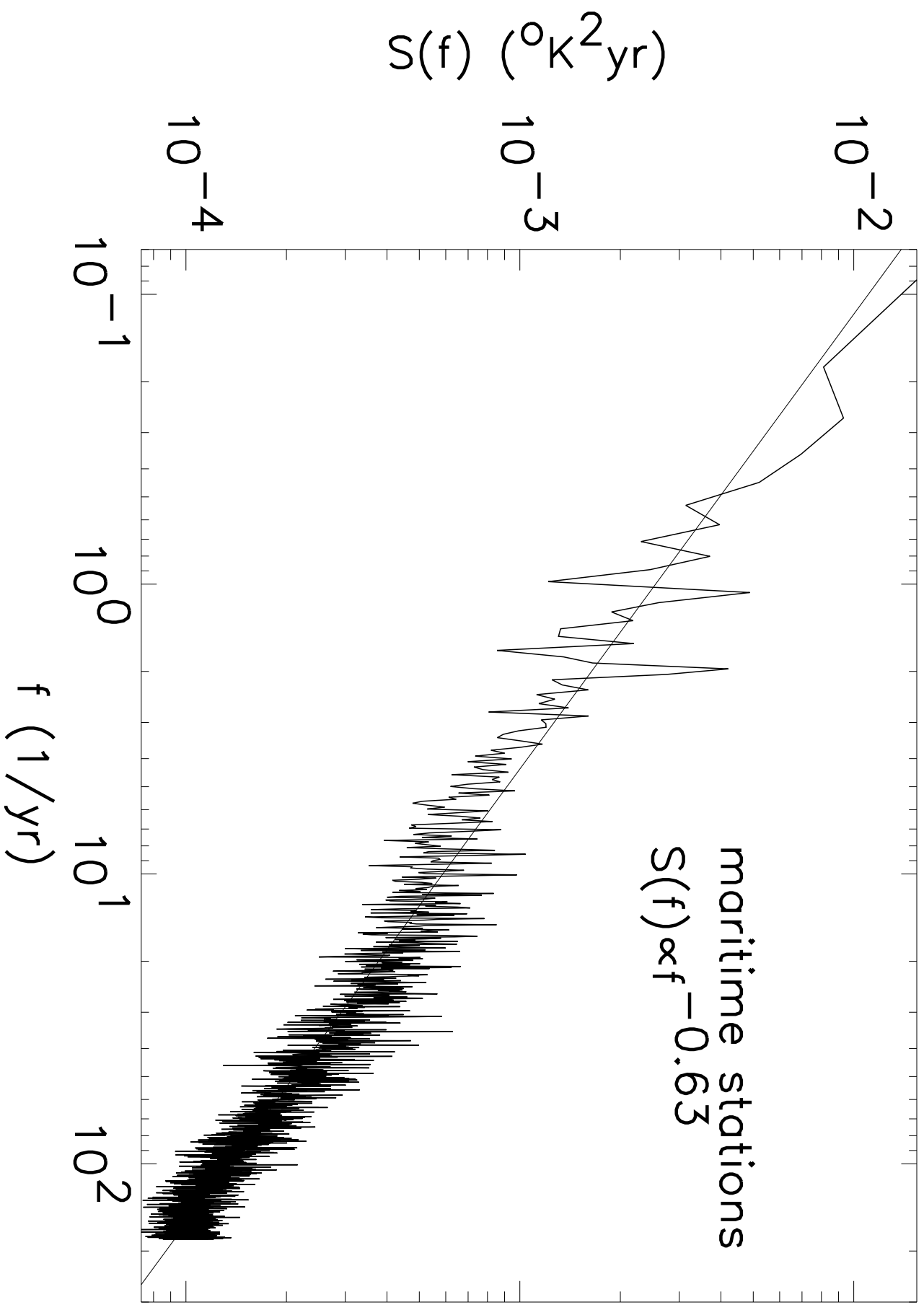


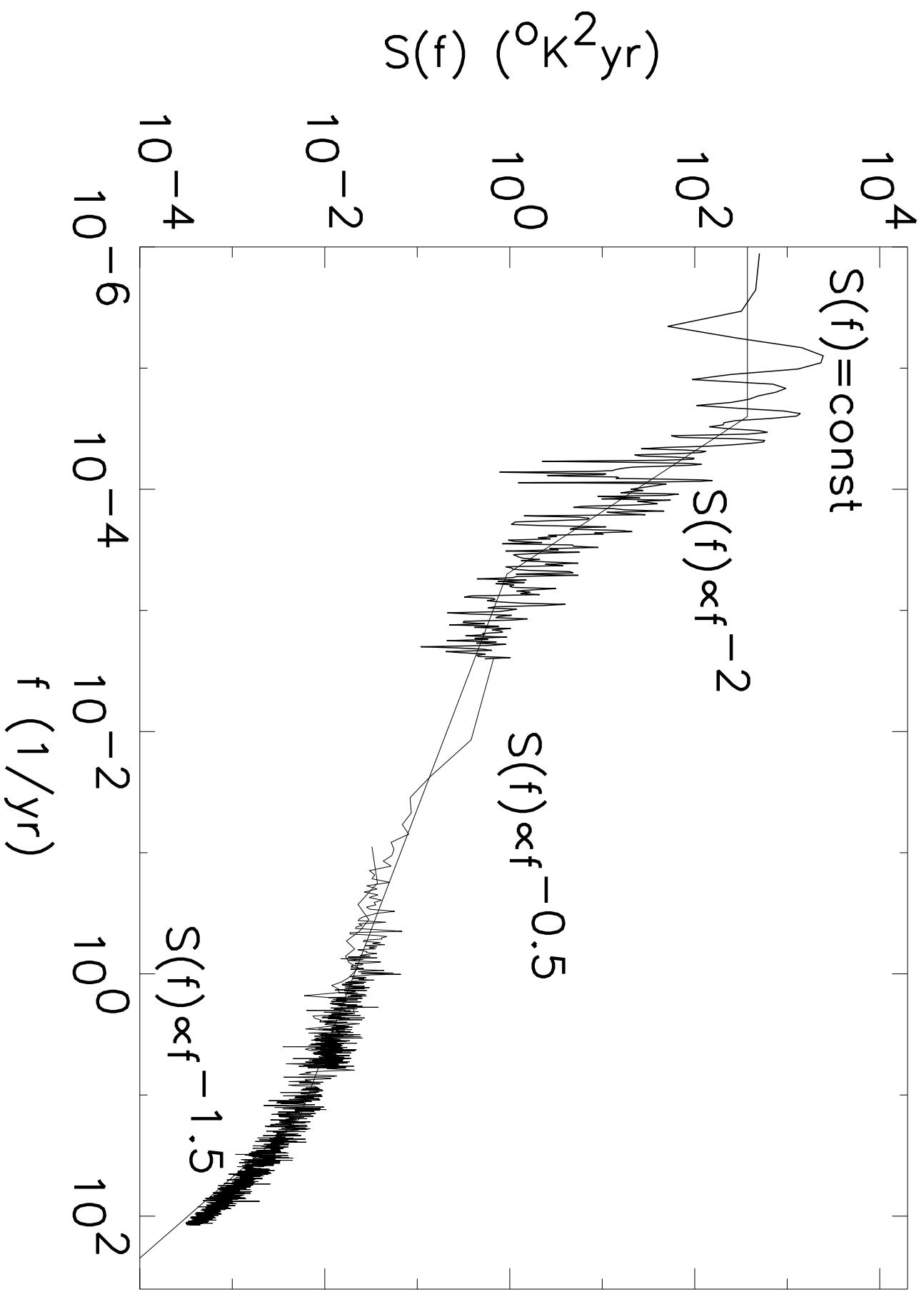












$S(f)$ (yr)

10^{-1}

10^{-2}

10^{-2}

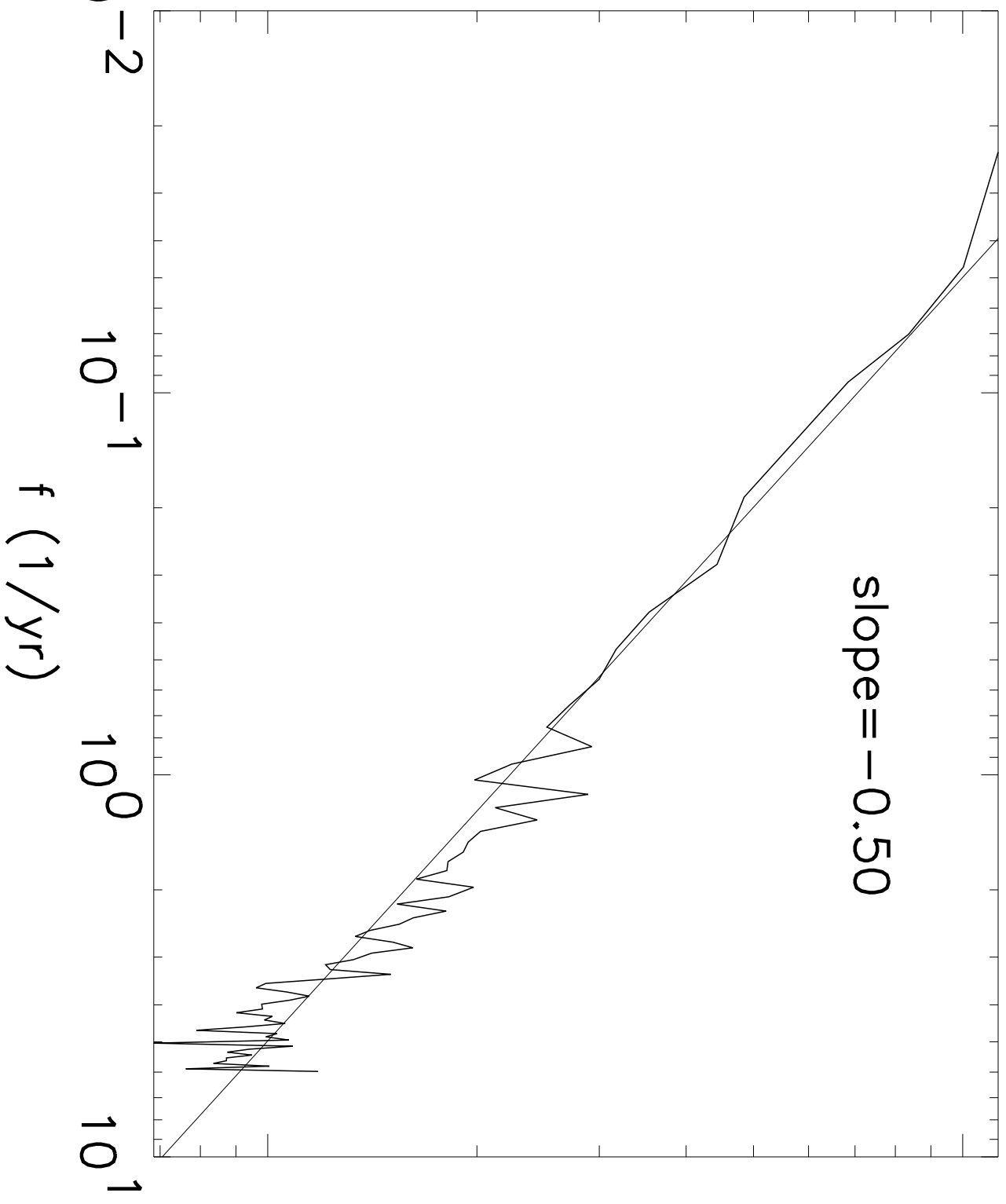
slope = -0.50

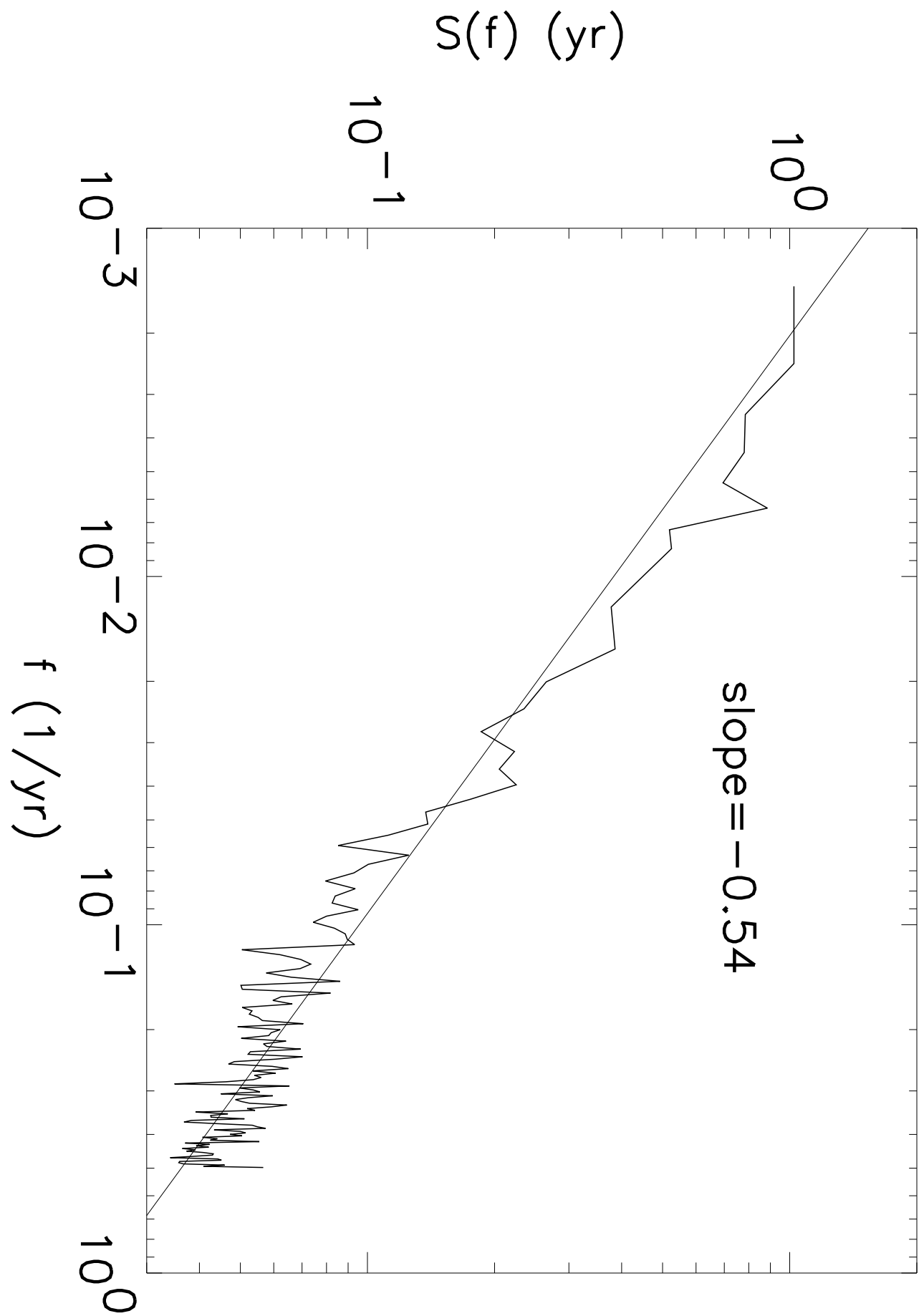
f (1/yr)

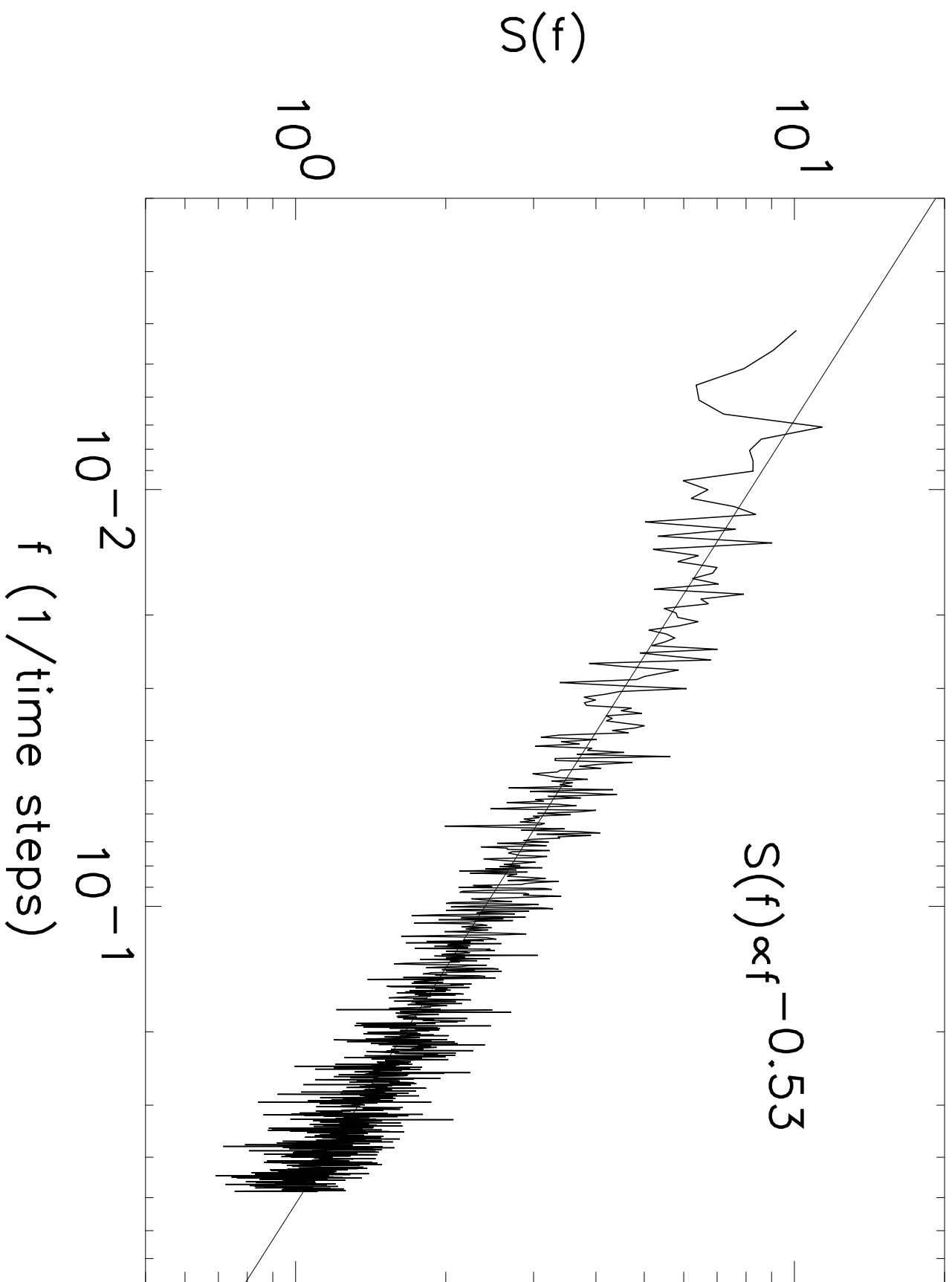
10^{-1}

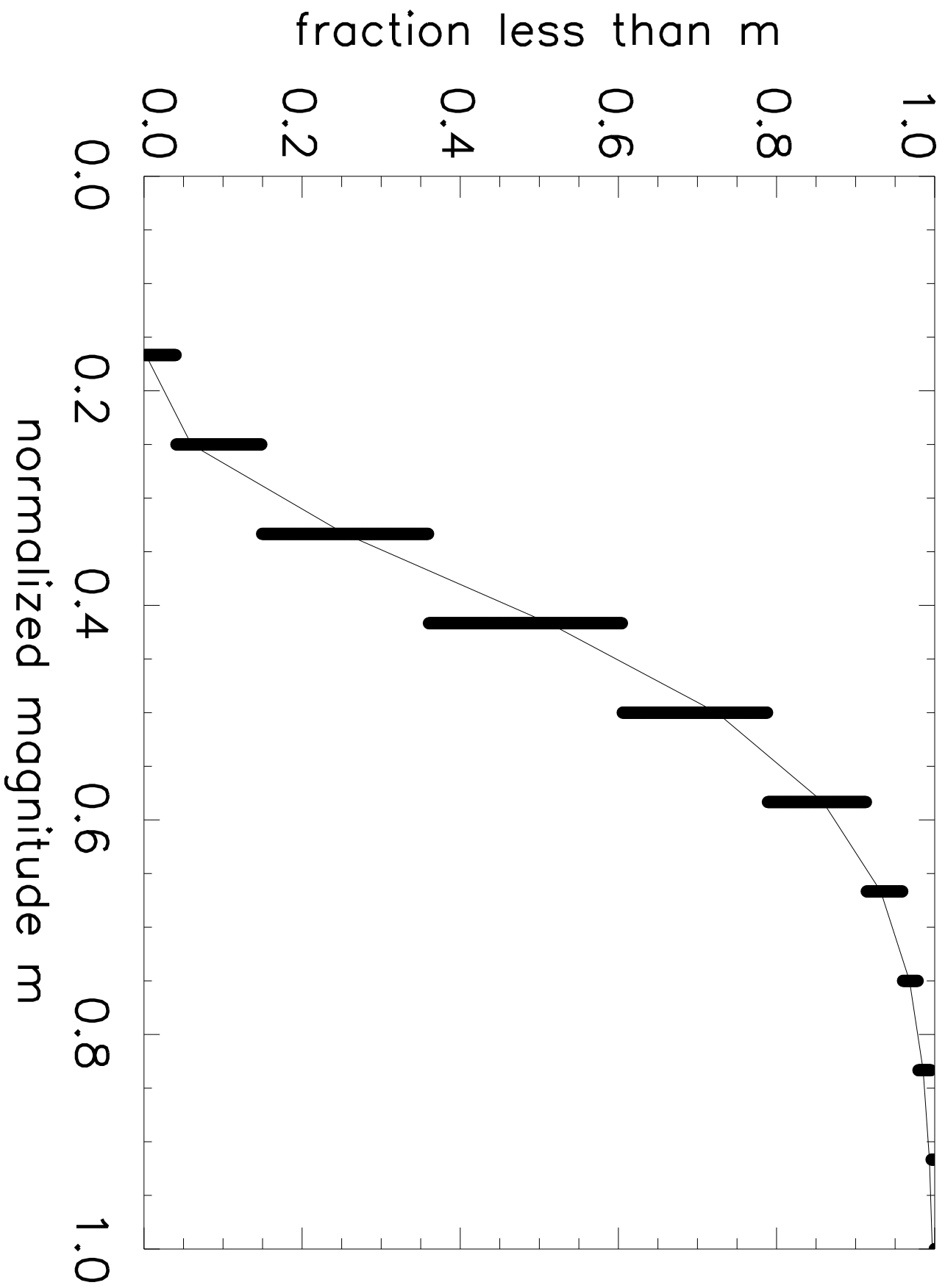
10^0

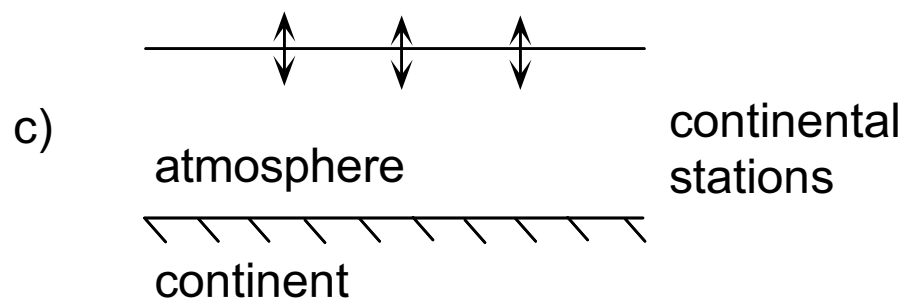
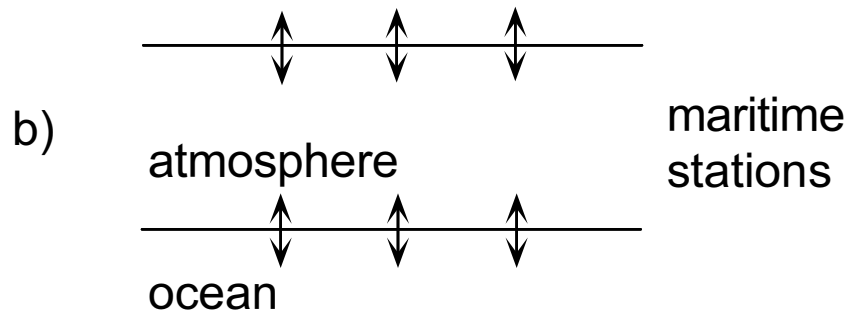
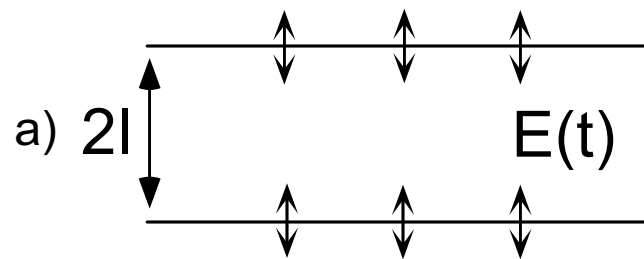
10^1



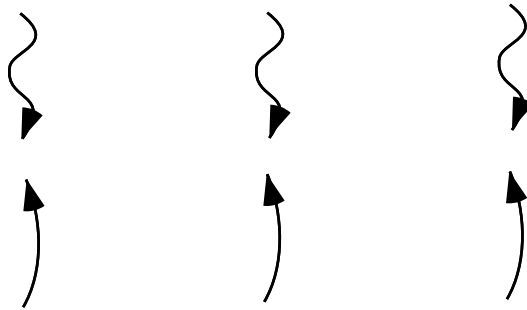








constant solar input



heat flux $\propto \Delta T$

$x=0$

atmosphere

$$\alpha = 100 \text{ m}^2/\text{s}$$

$$\sigma = 10^5 \text{ W/m}^2\text{K}$$

$$\rho = 1 \text{ kg/m}^3$$

$$c = 1000 \text{ J/kg}^{\circ}\text{K}$$

$$w_1 = 8000 \text{ m}$$

$x=w_1$

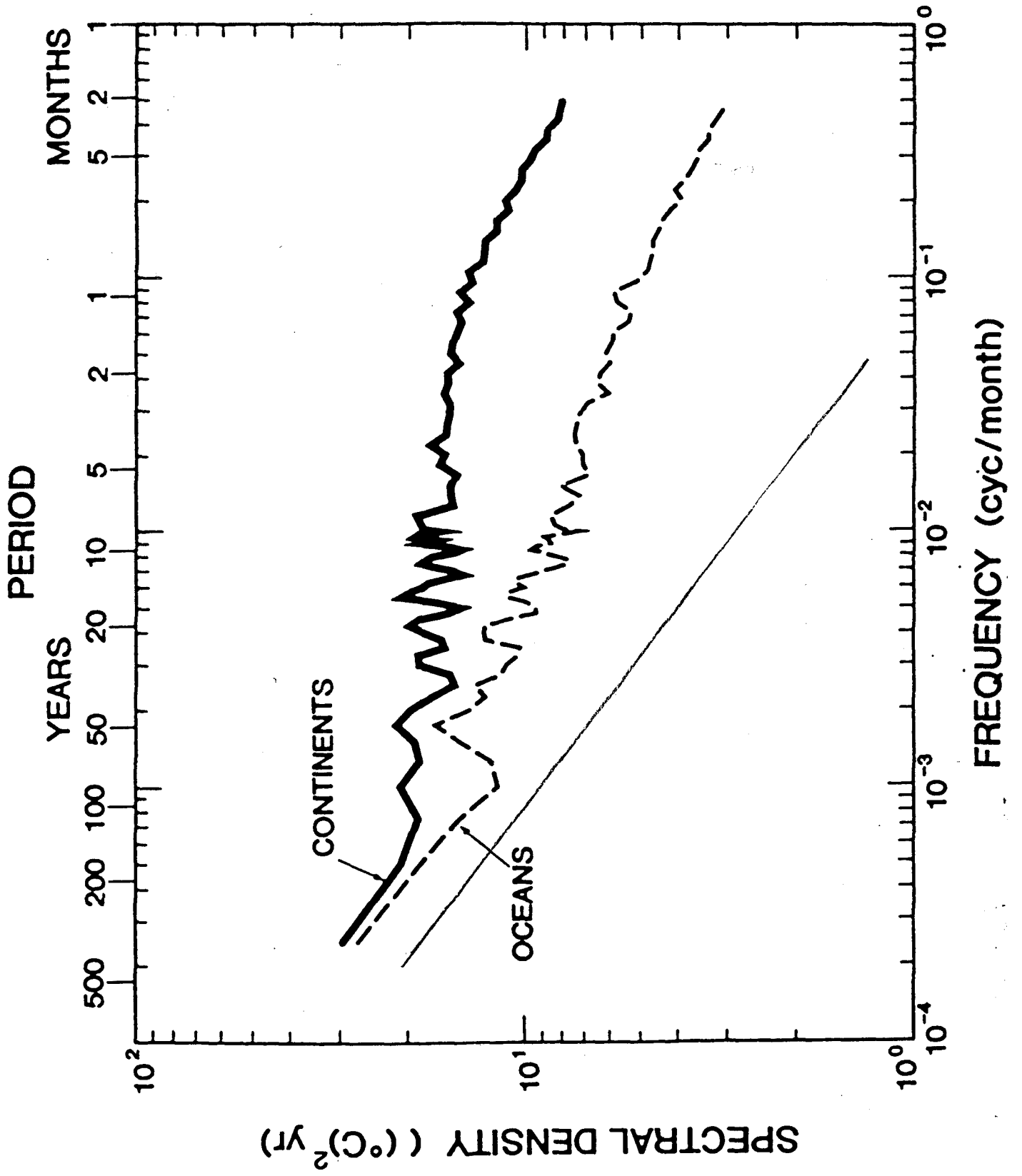
ocean

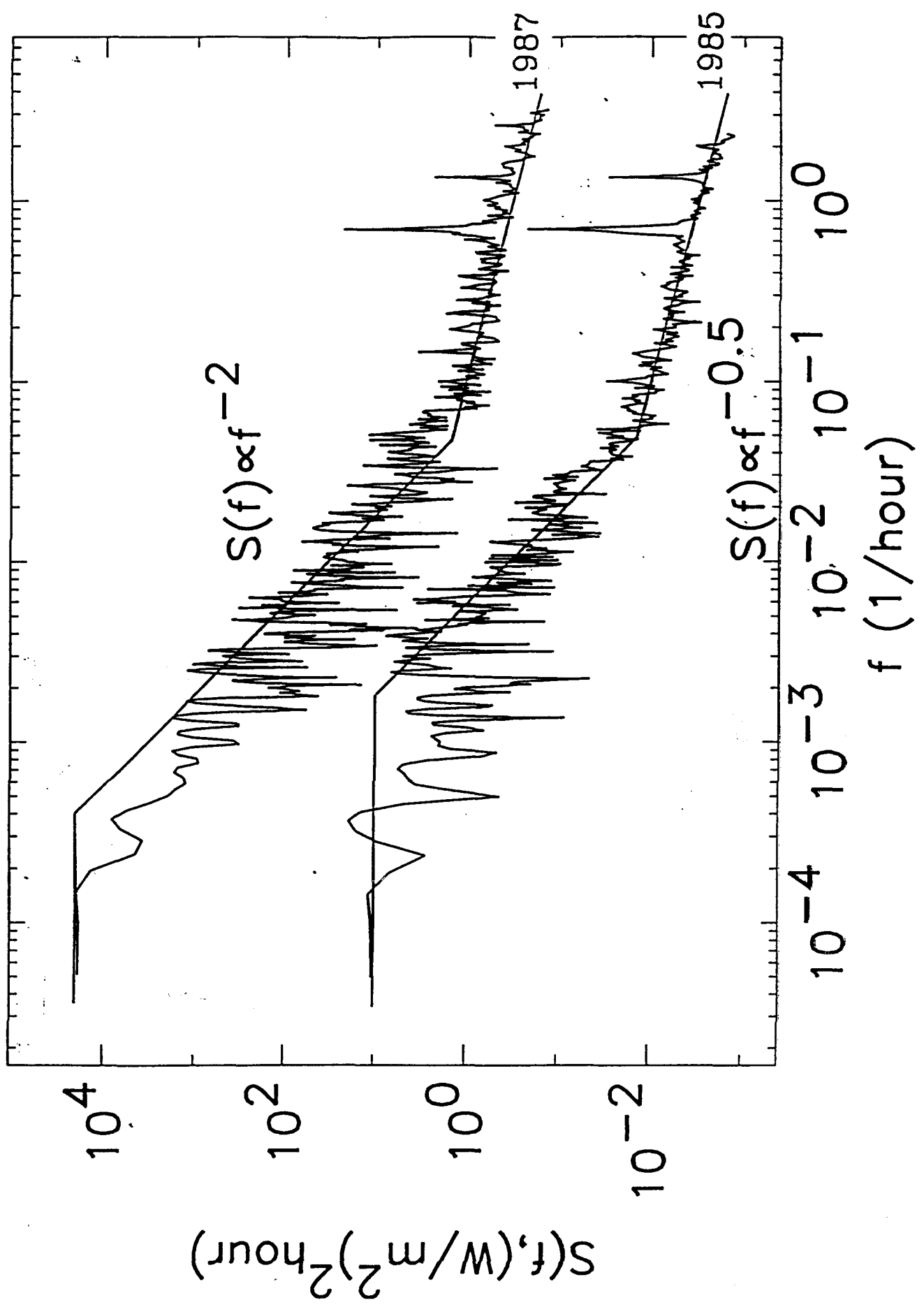
$$\alpha' = 6 \times 10^{-5} \text{ m}^2/\text{s} \quad c' = 4200 \text{ J/kg}^{\circ}\text{K}$$

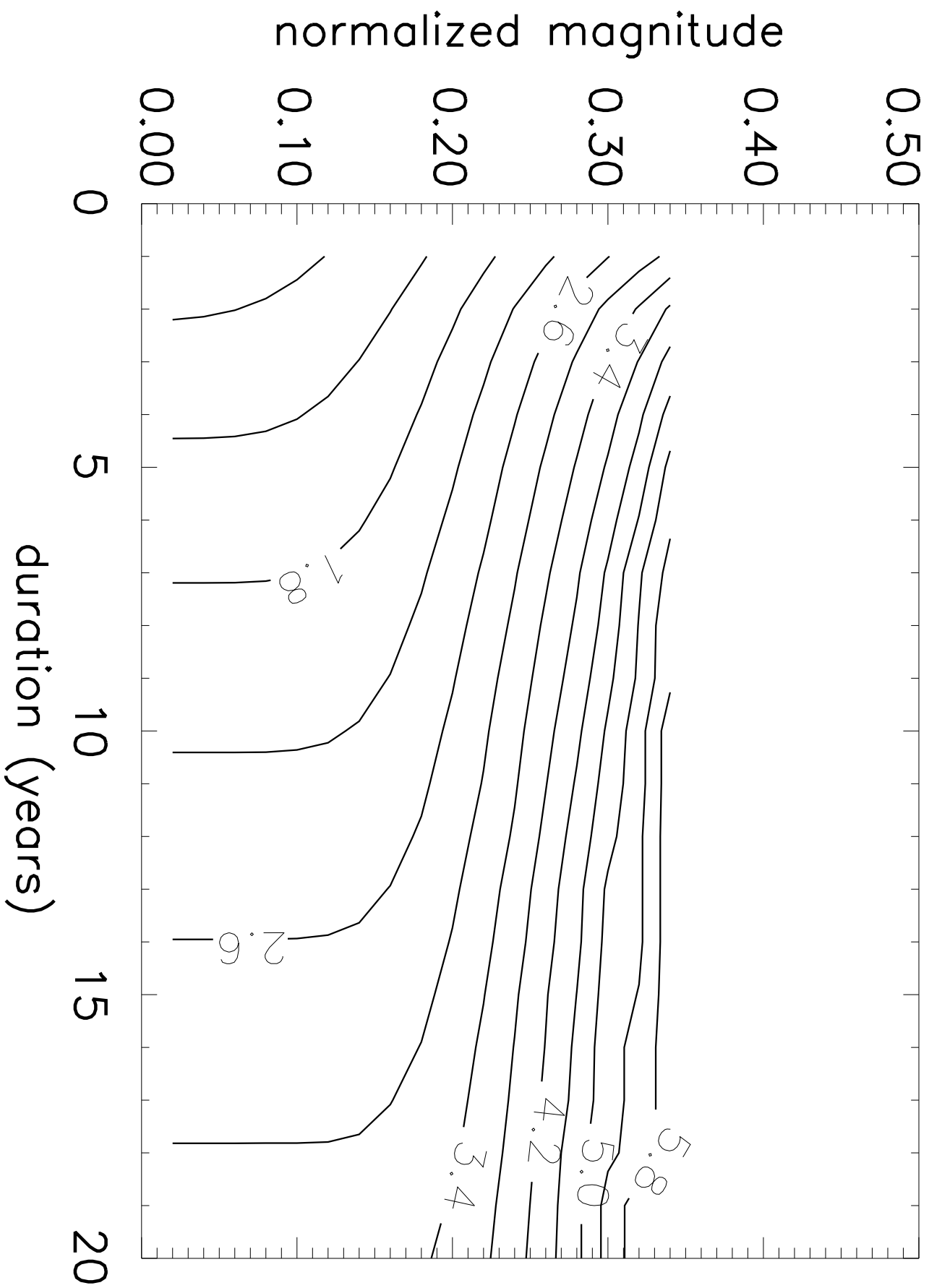
$$\rho' = 1000 \text{ kg/m}^3 \quad w_2 = 4000 \text{ m}$$

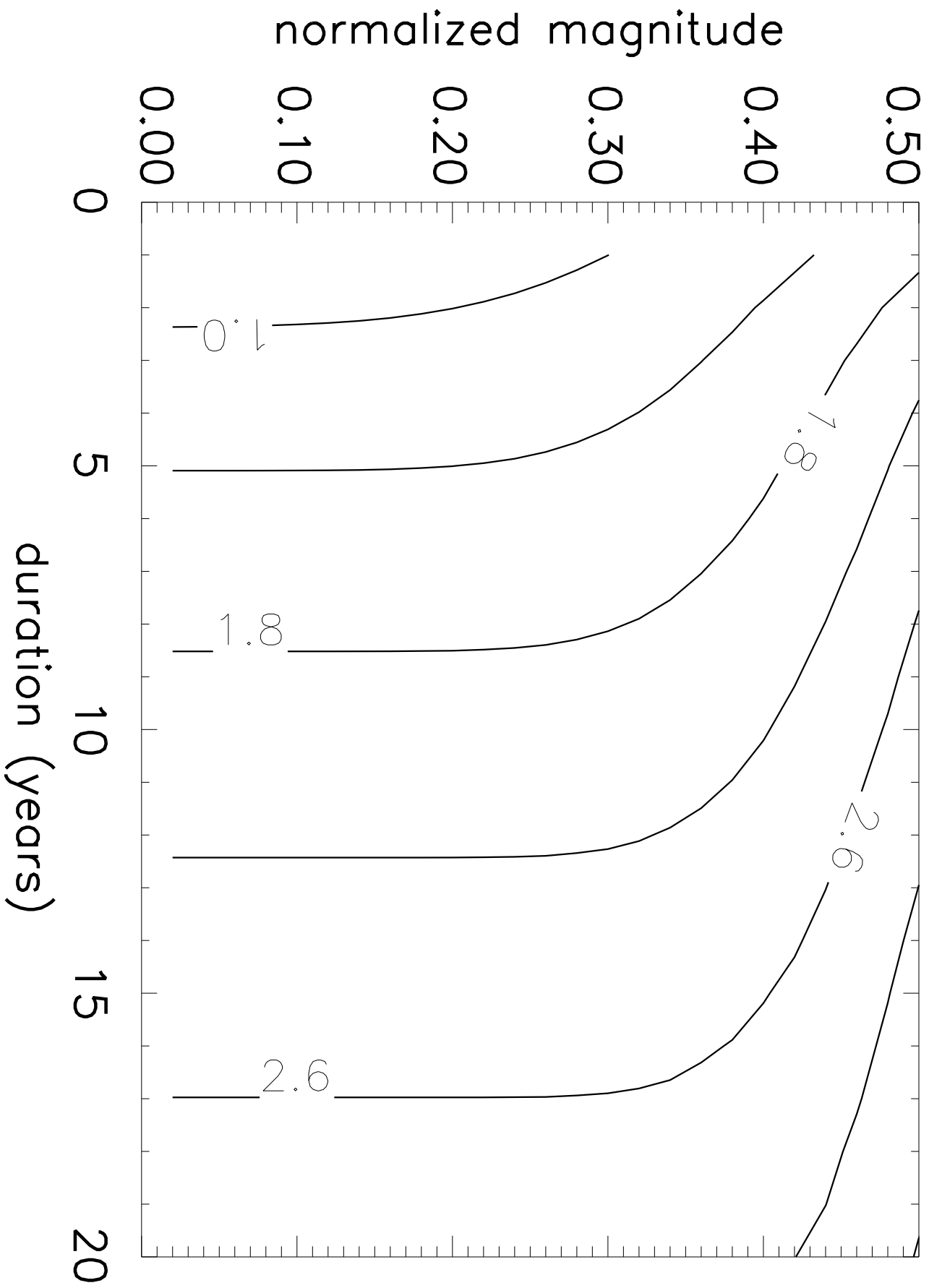
$$\sigma' = 250 \text{ W/m}^2\text{K}$$

$x=w_1+w_2$

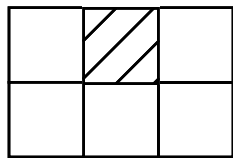




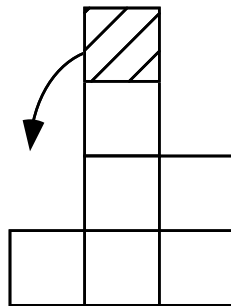
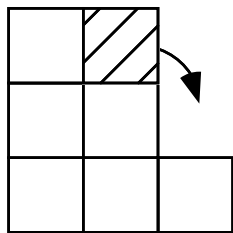




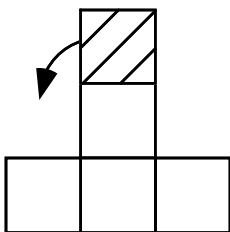
a)



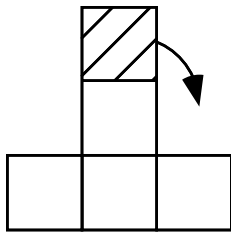
b)

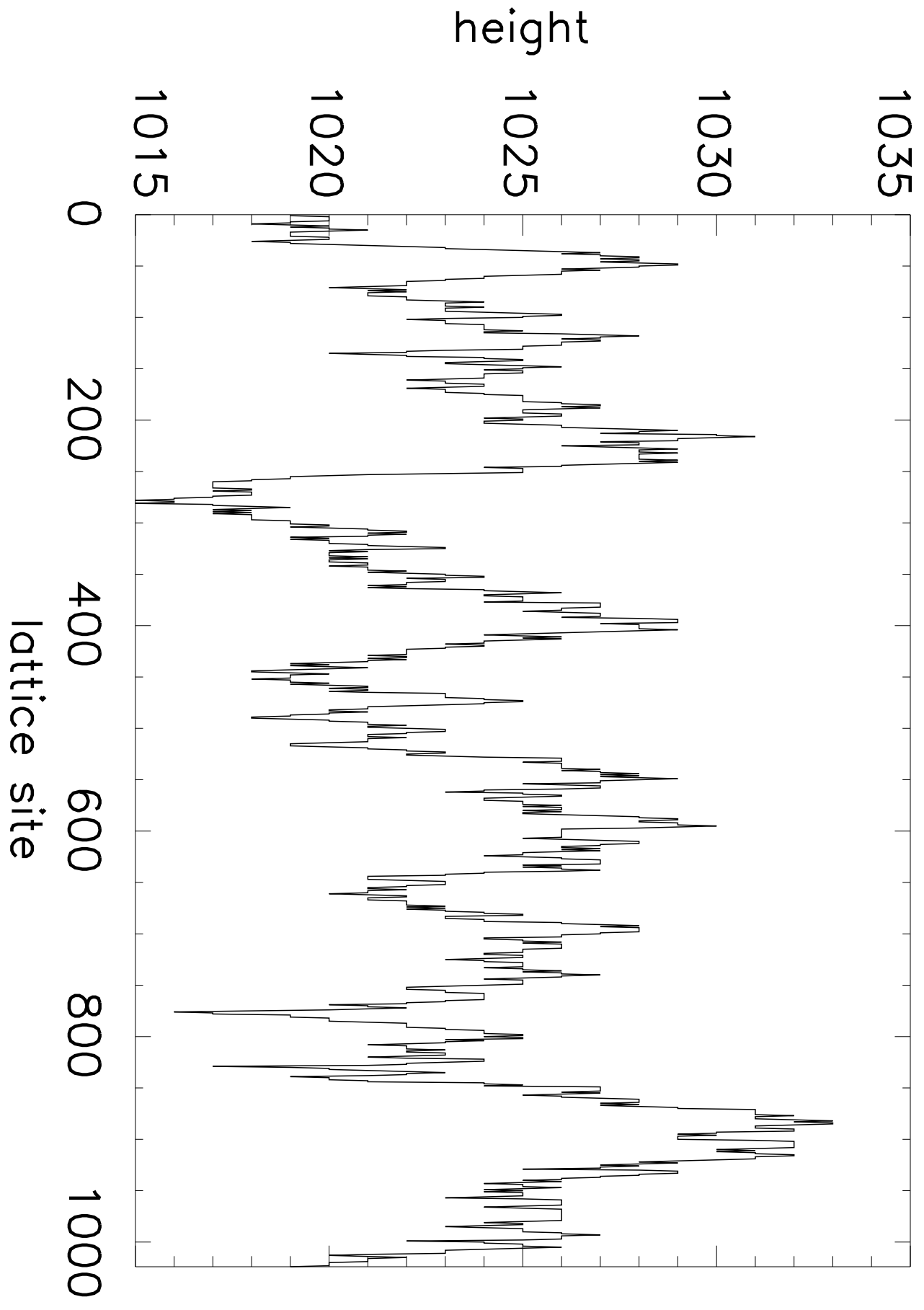


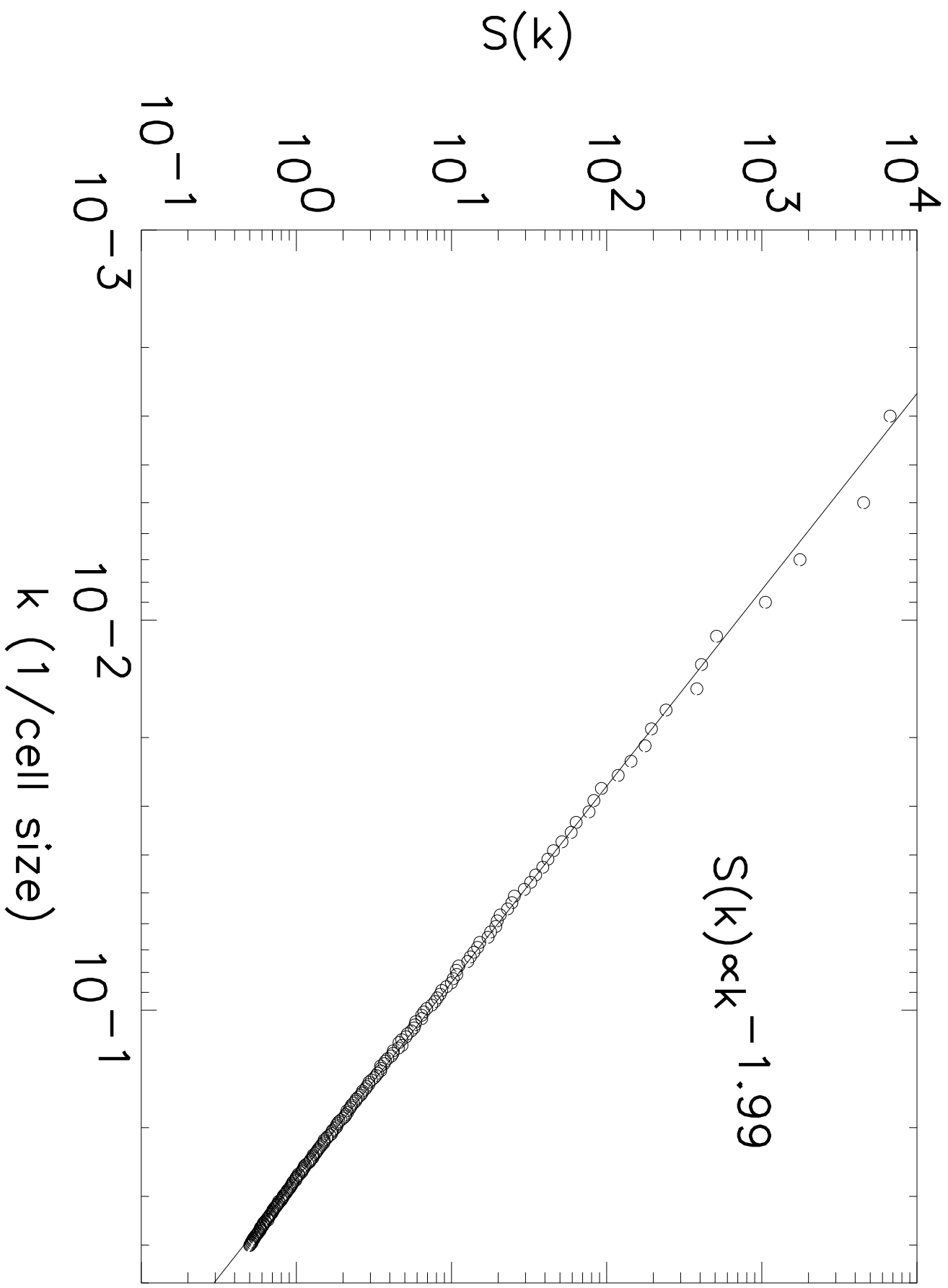
c)

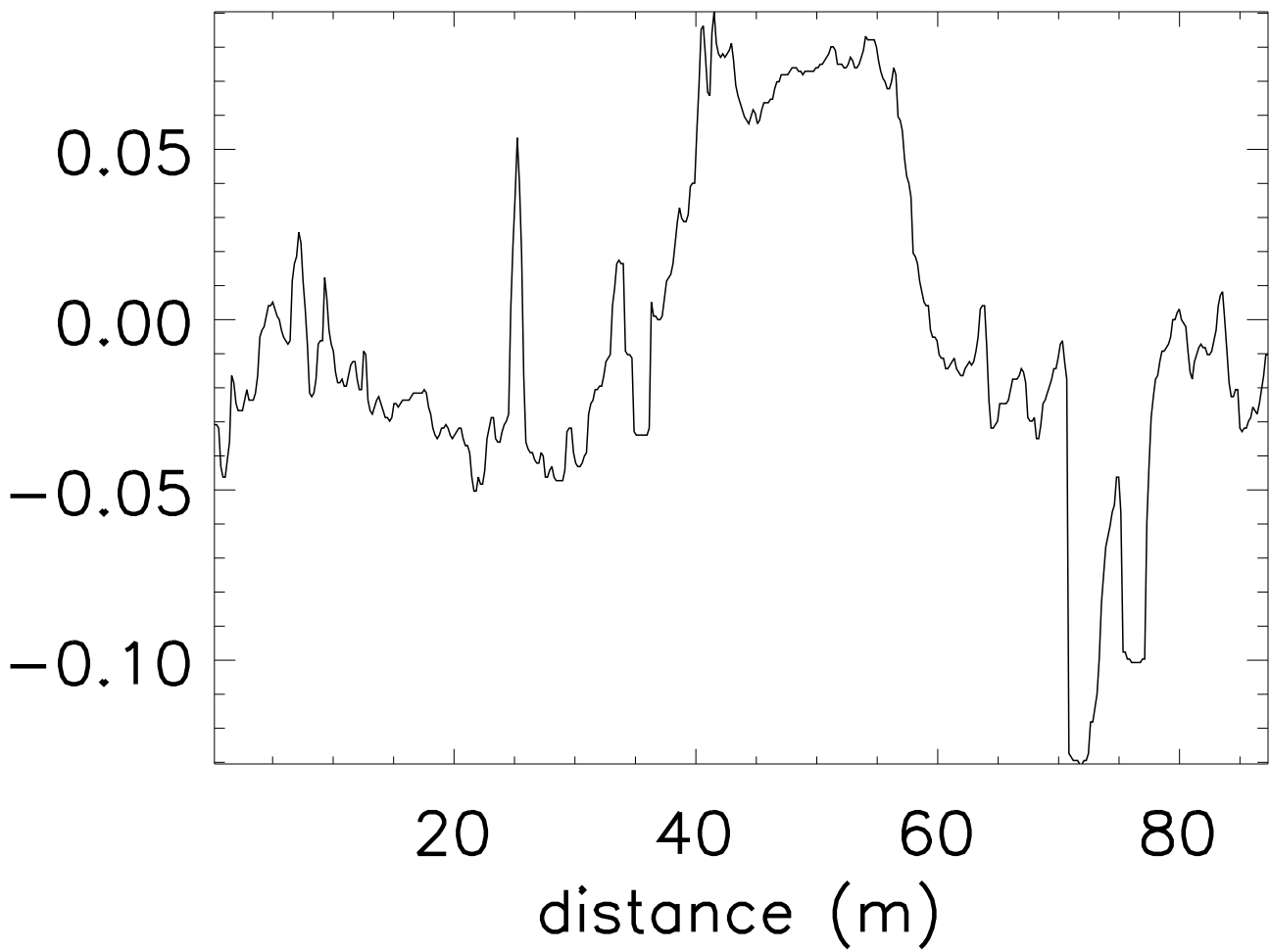


or









5/4

10

12

14

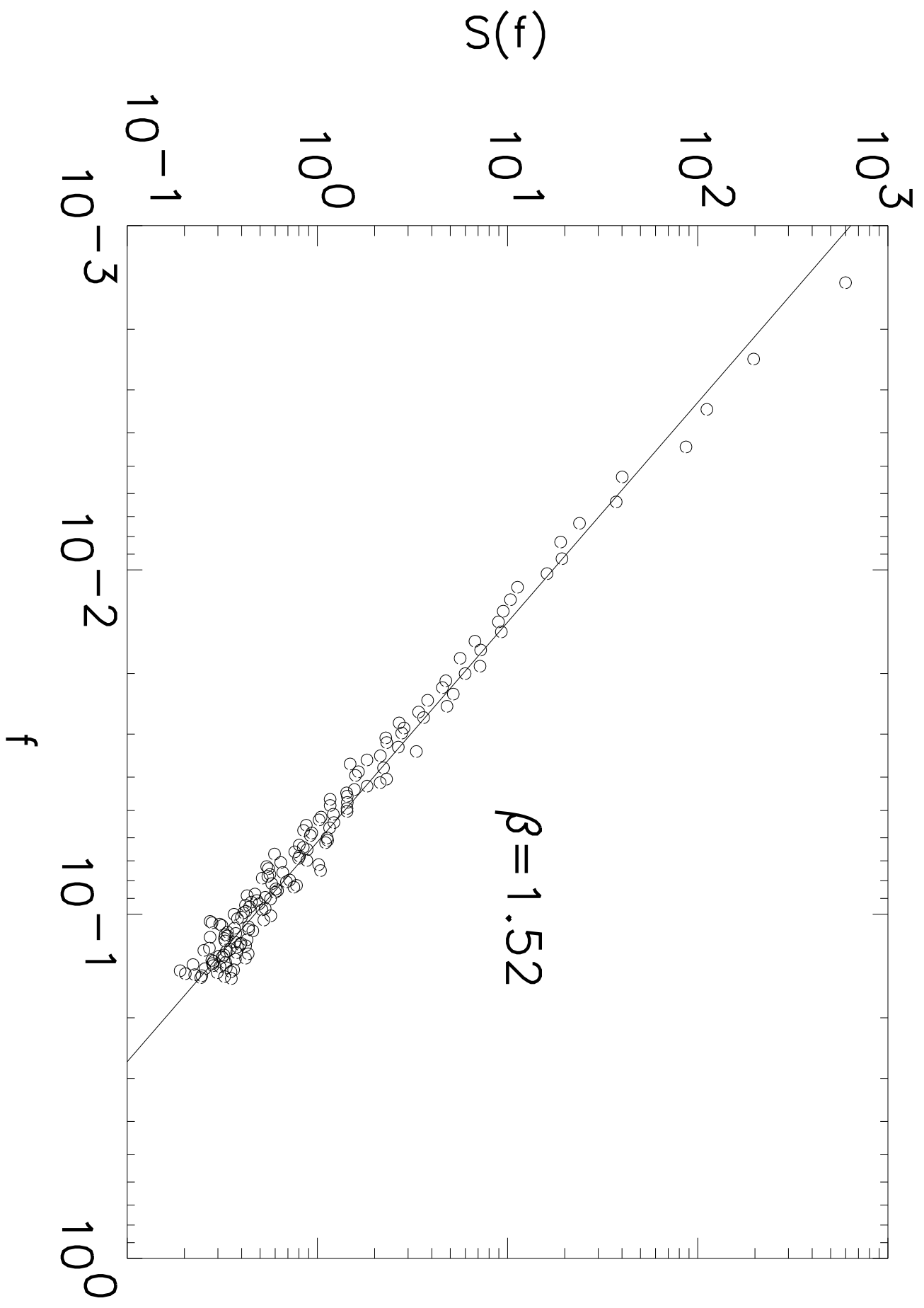
16

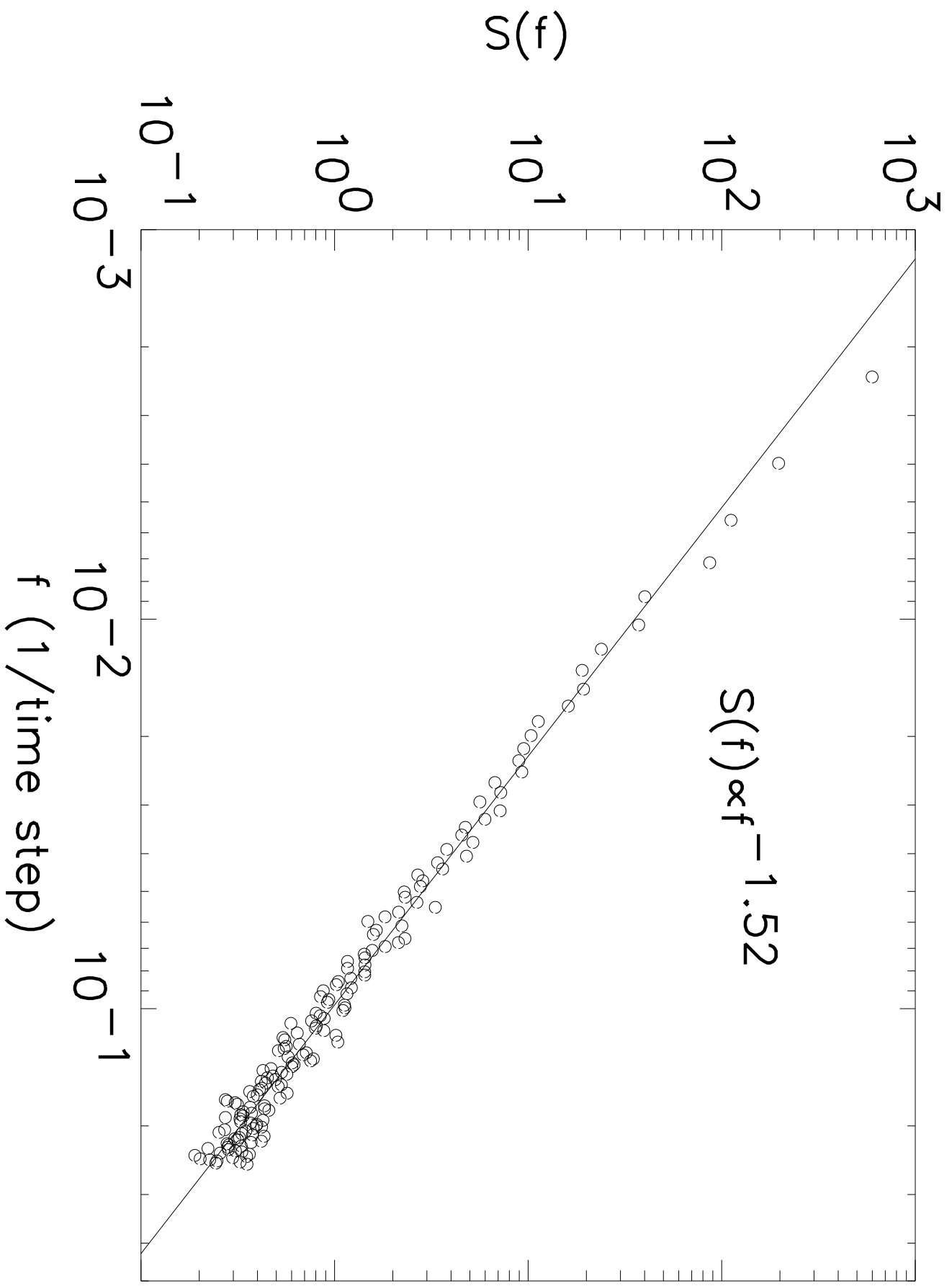
18

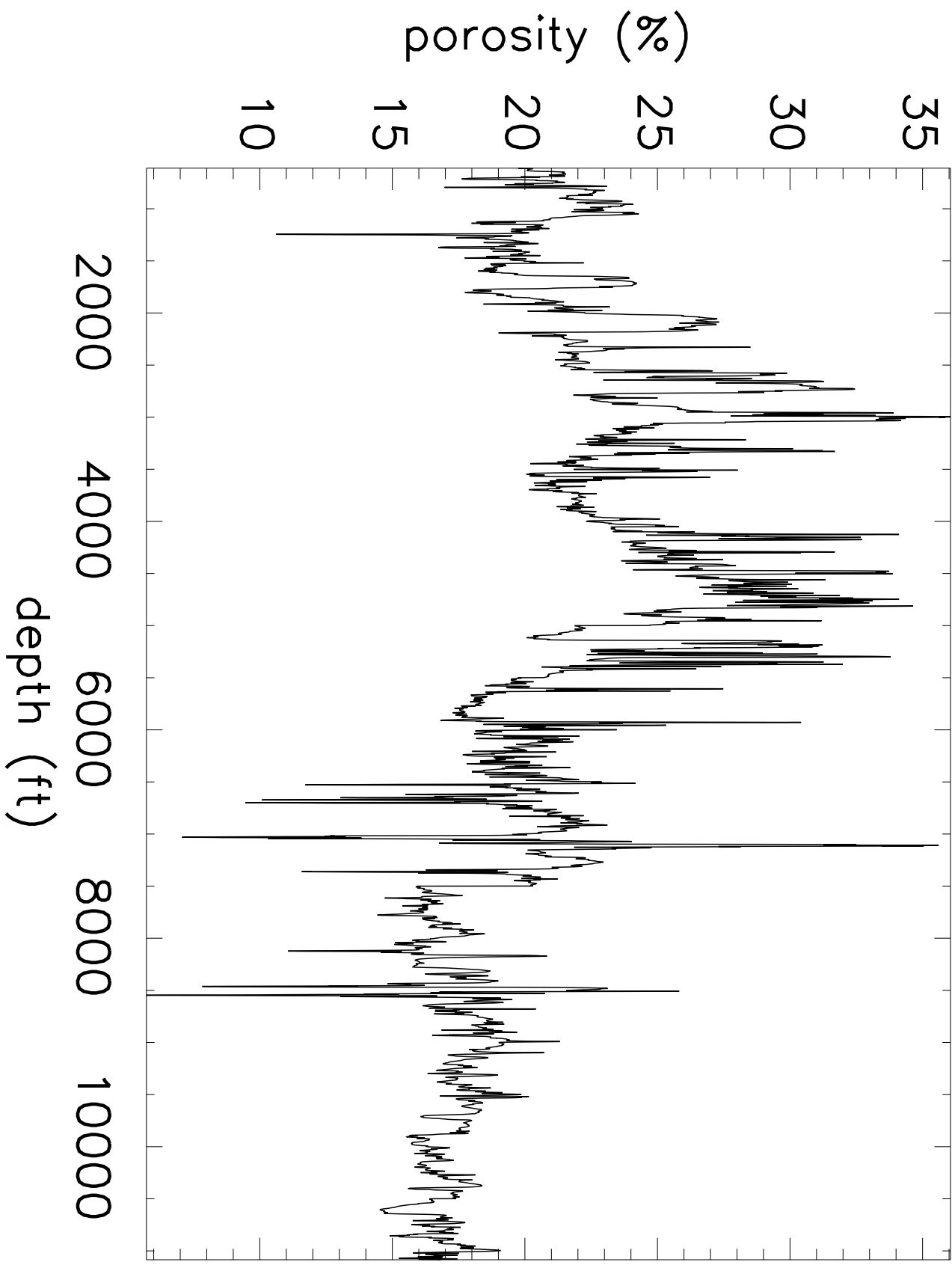
20

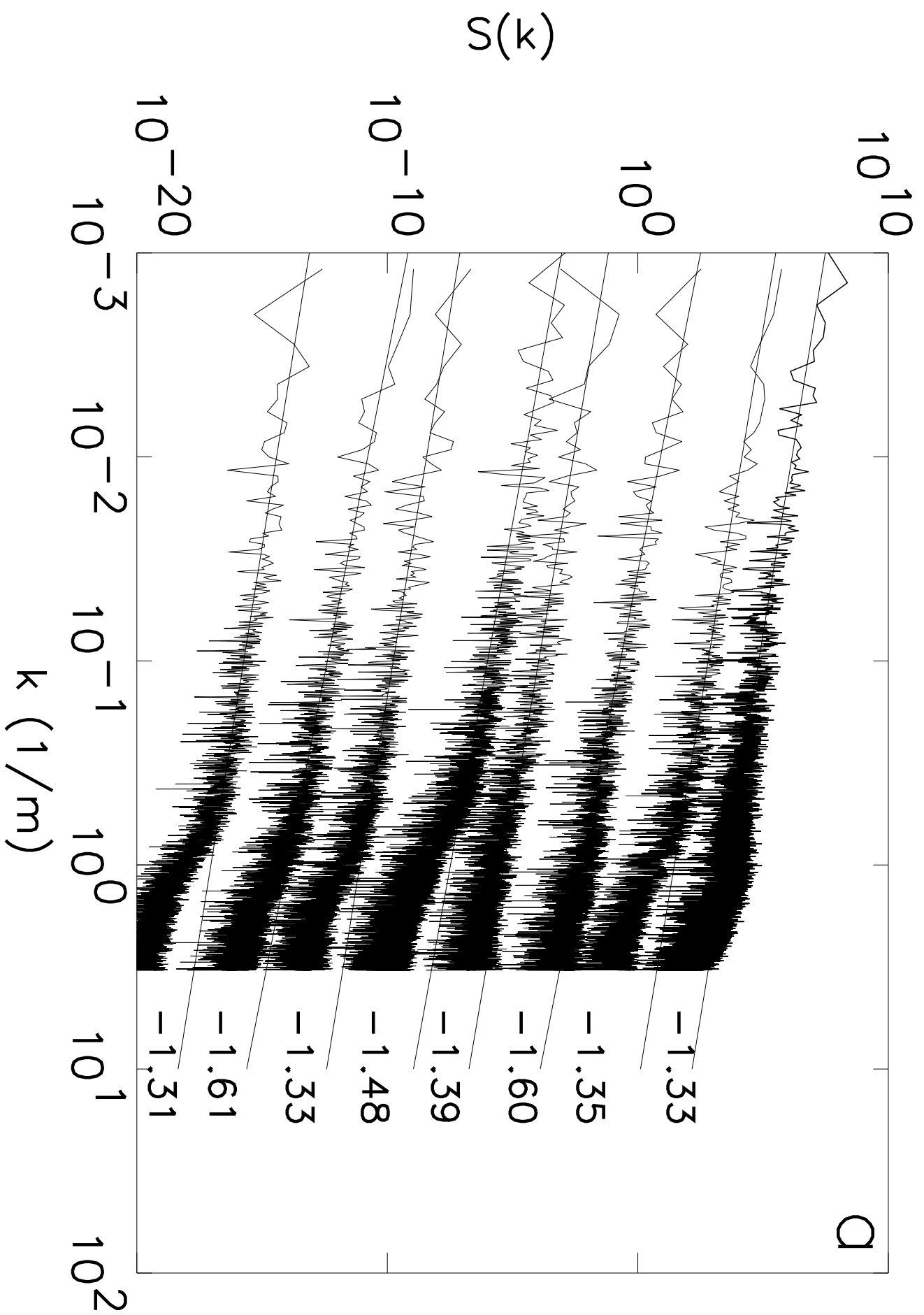
22

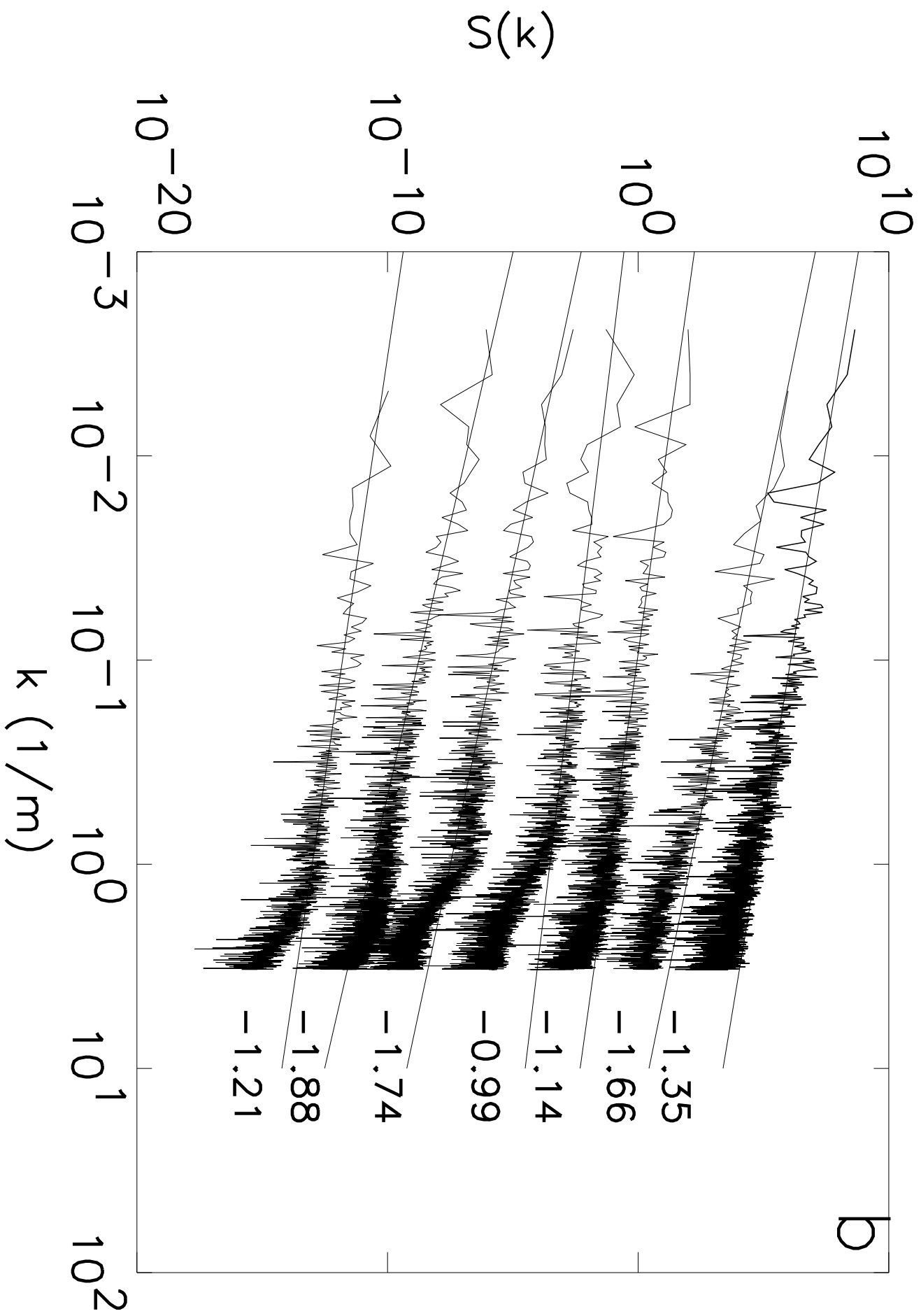
timesteps $\times 10^6$



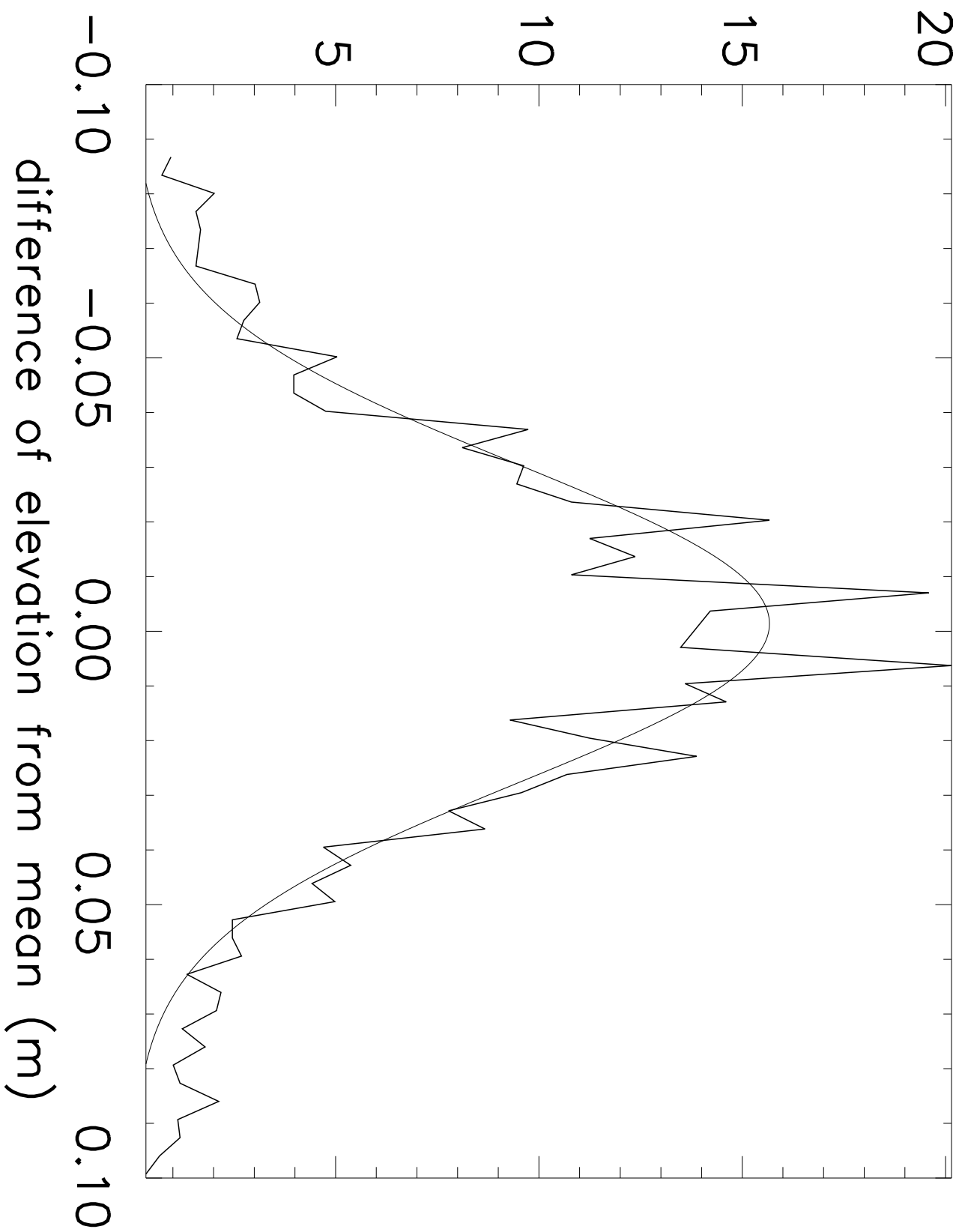


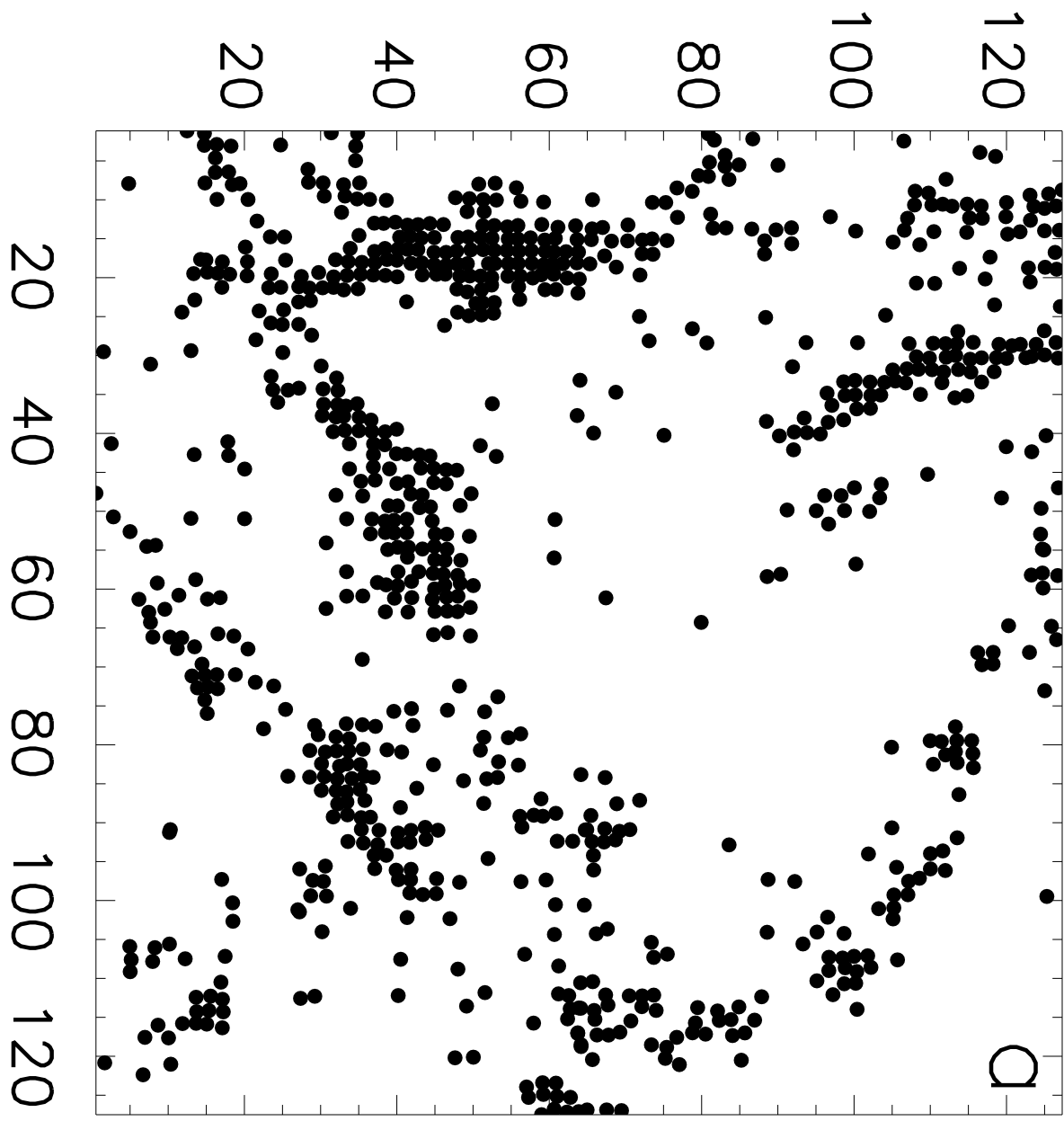


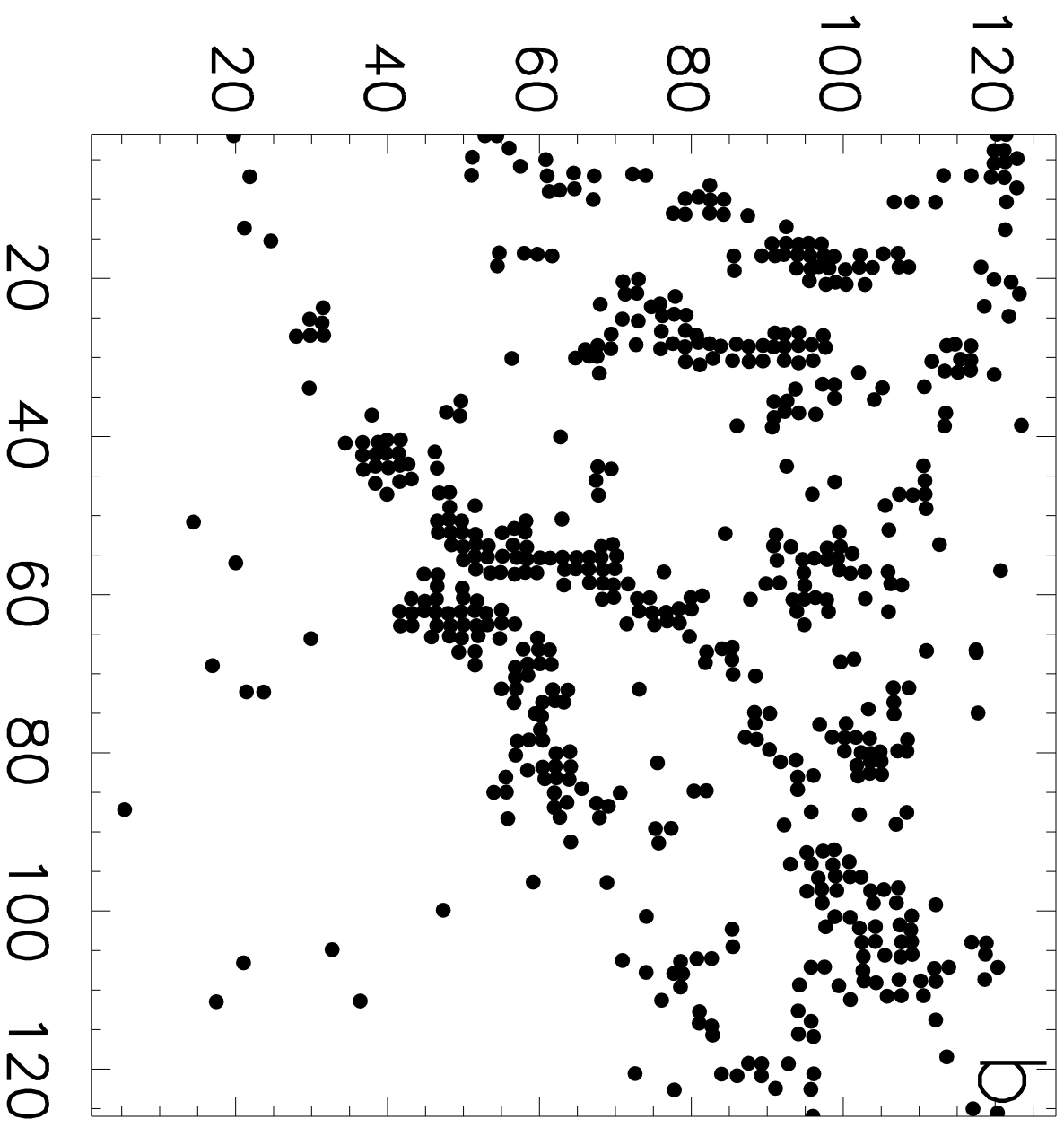


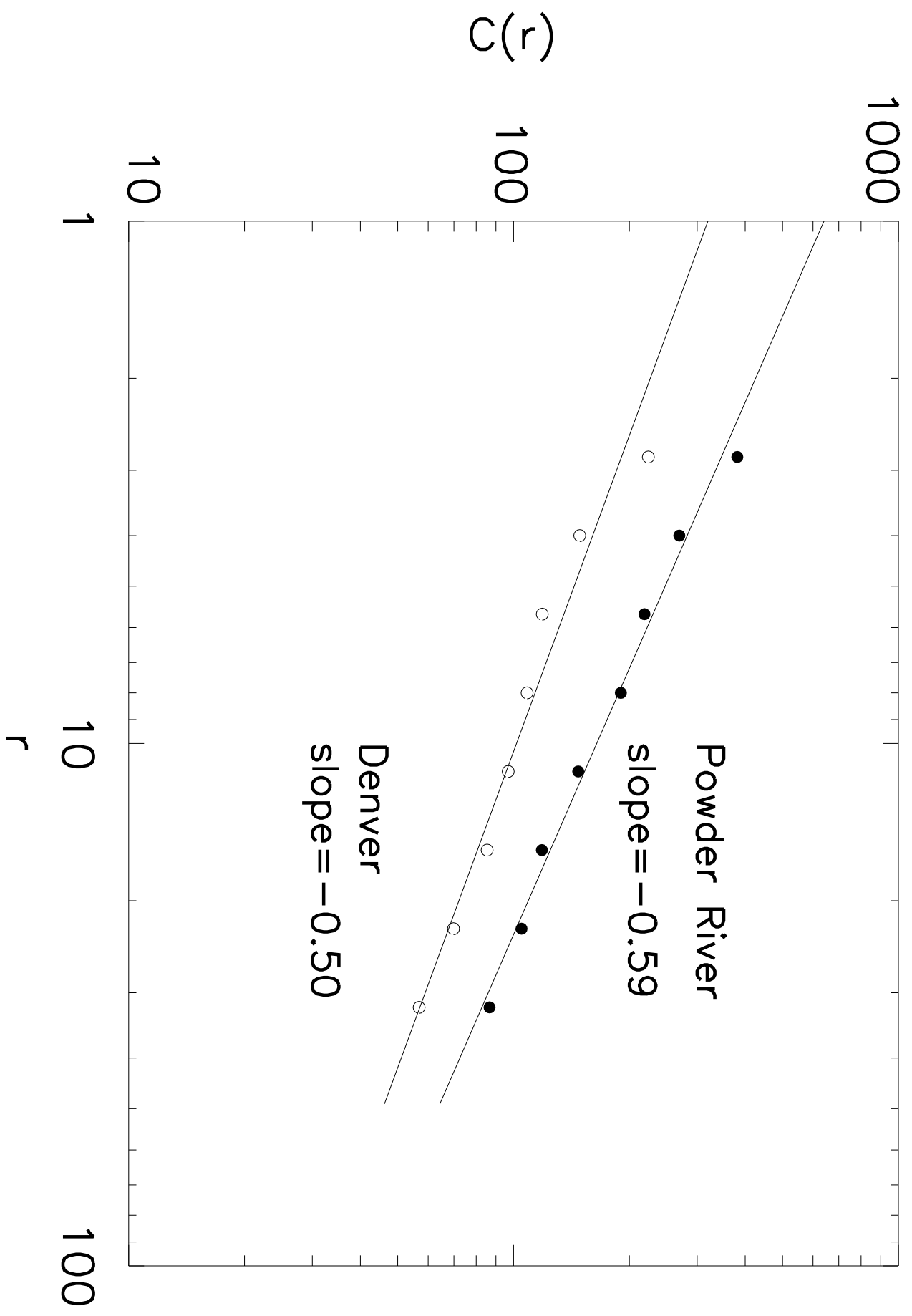


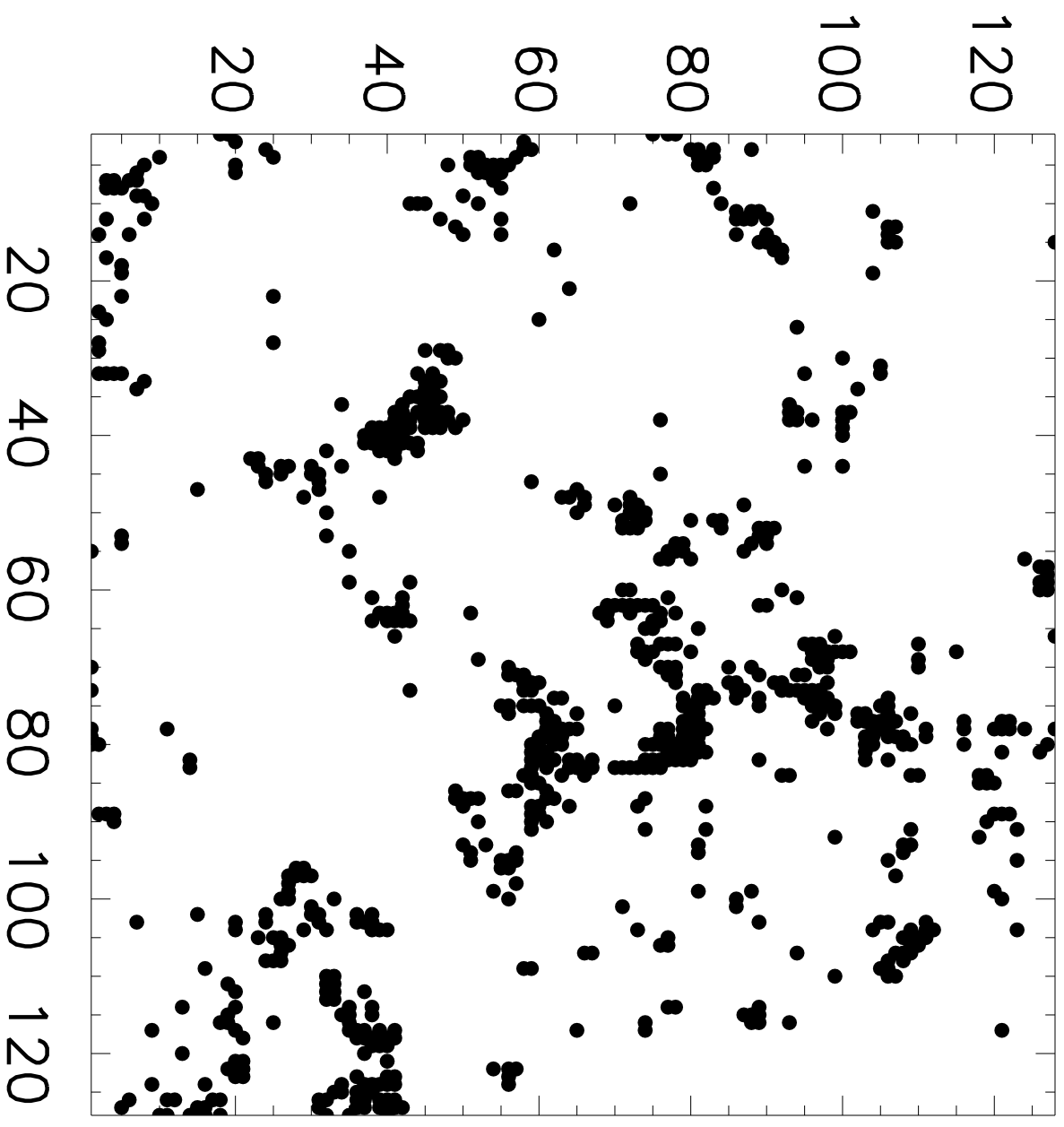
probability density function

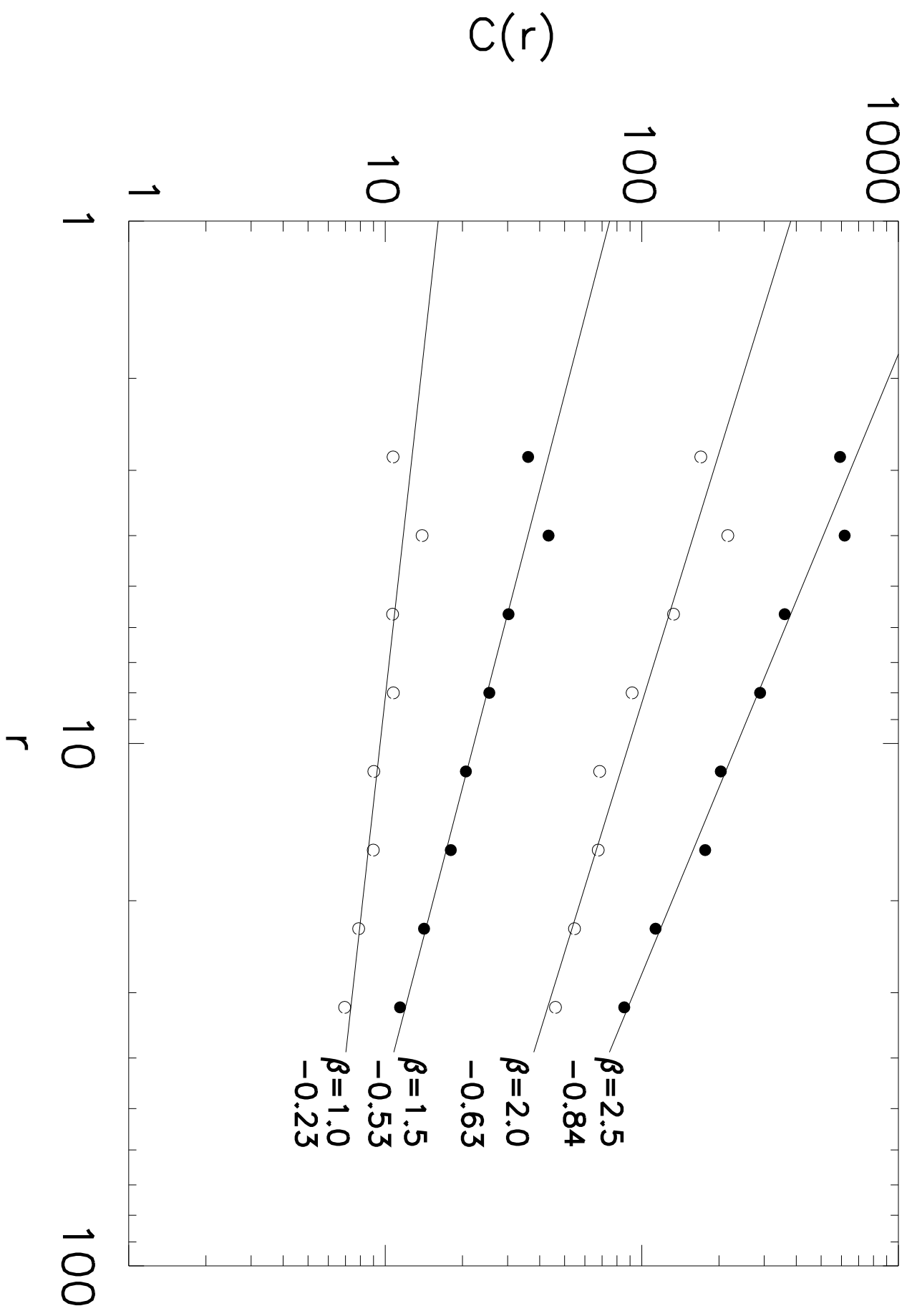


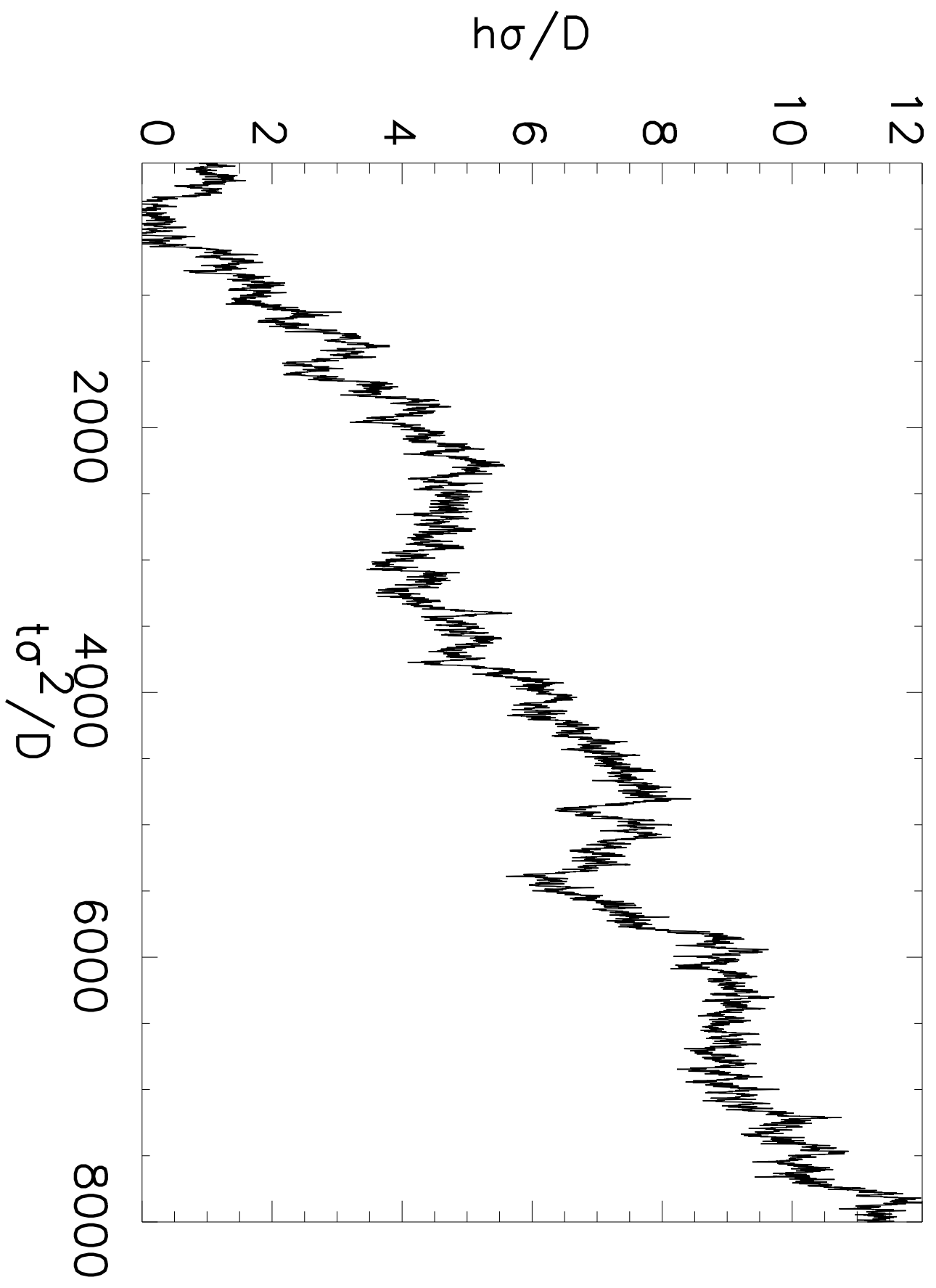


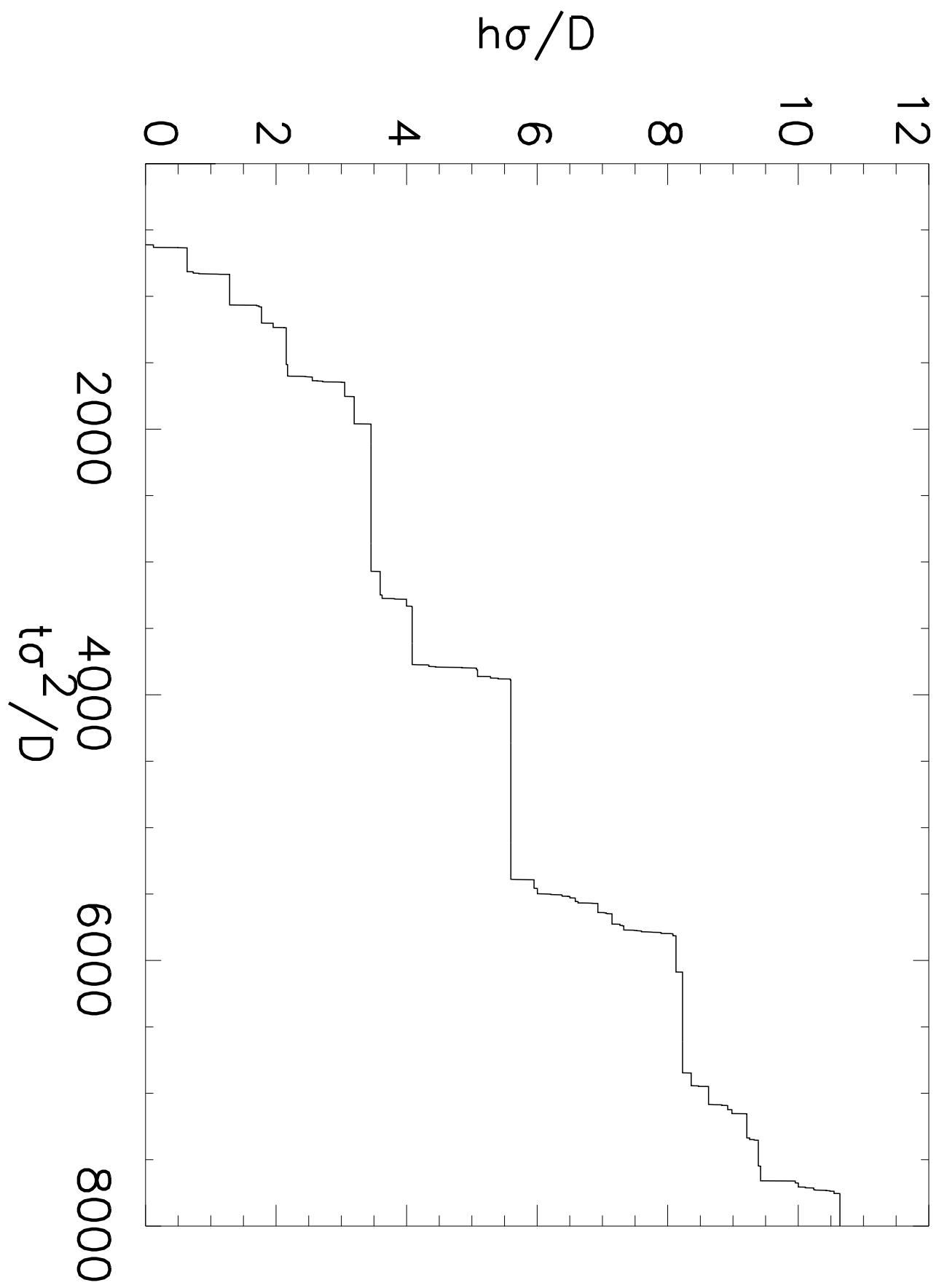


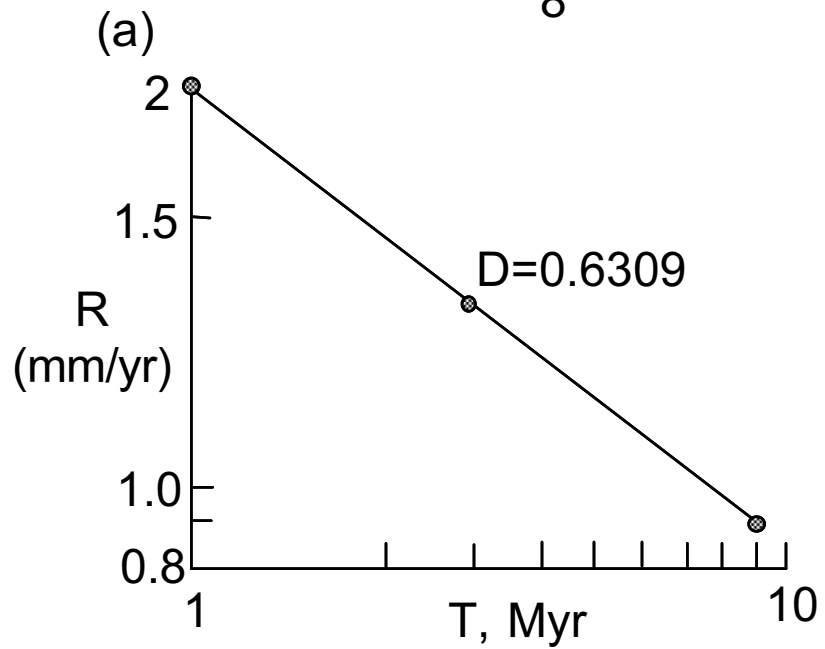
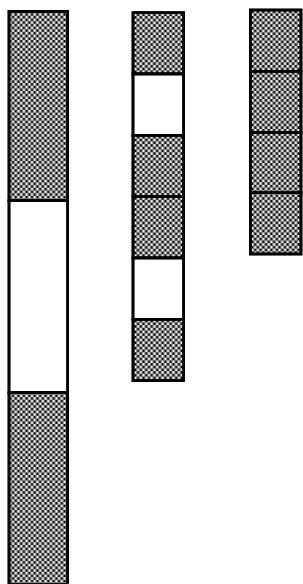
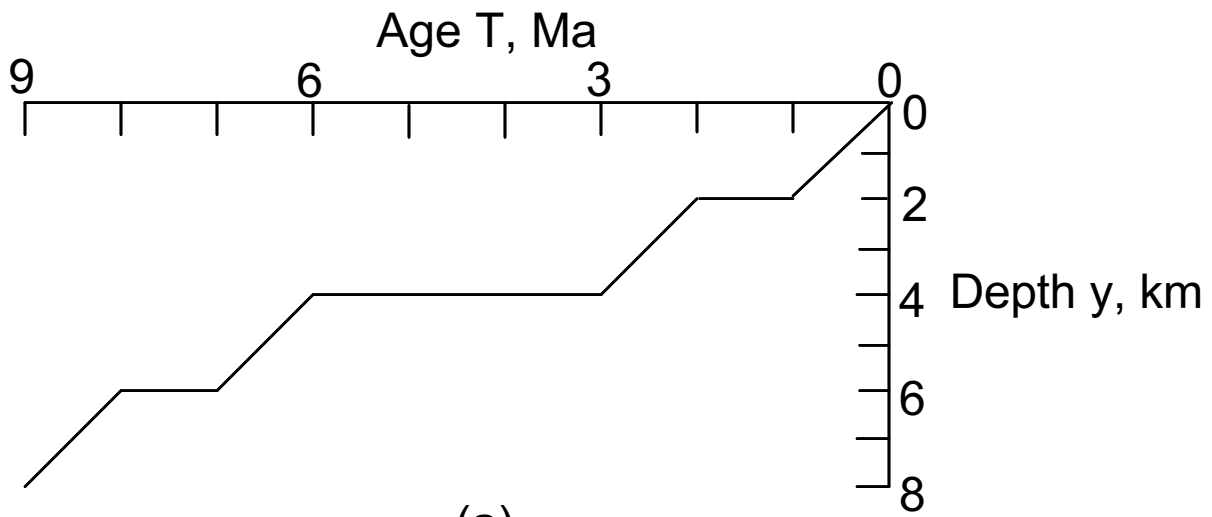






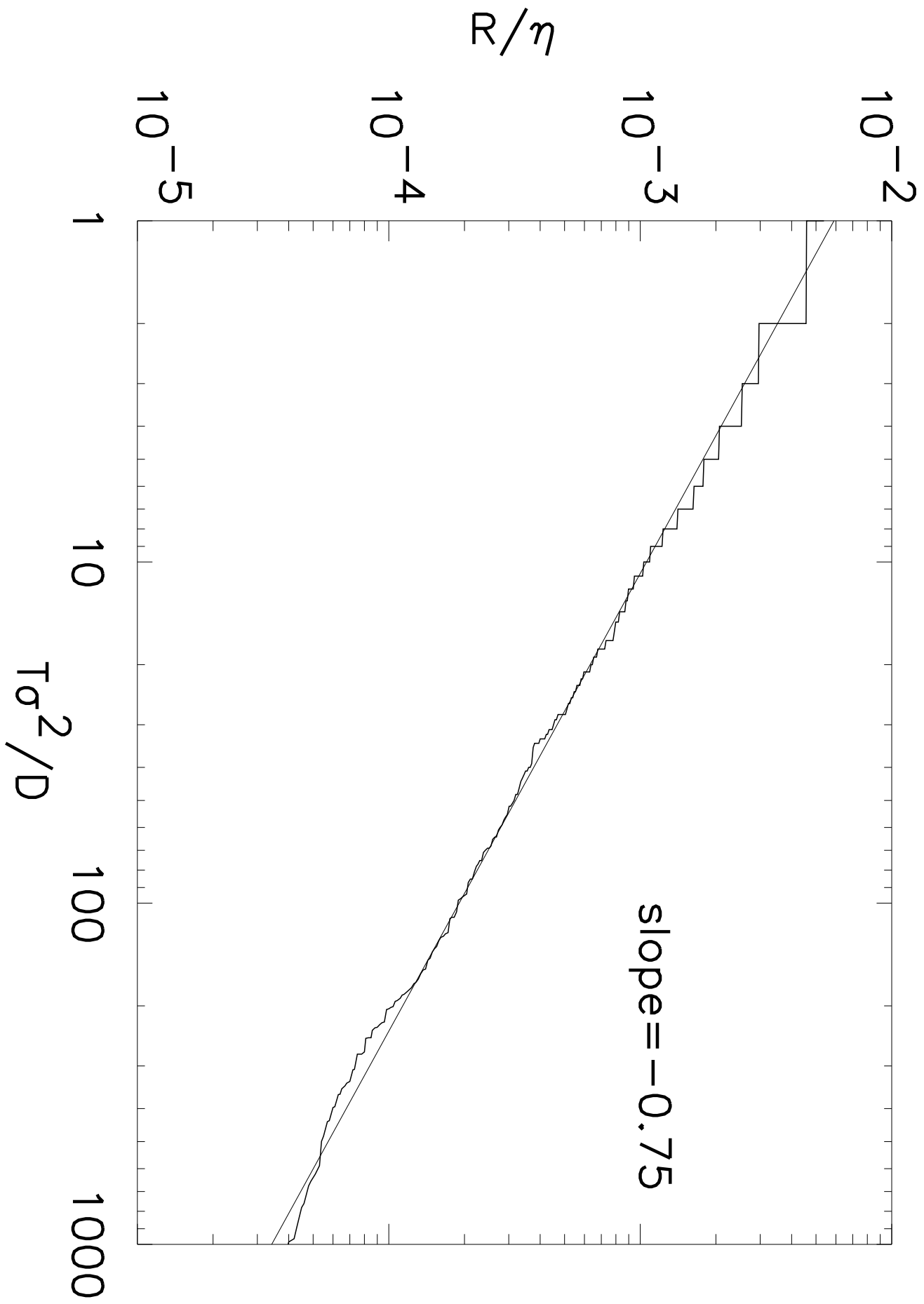


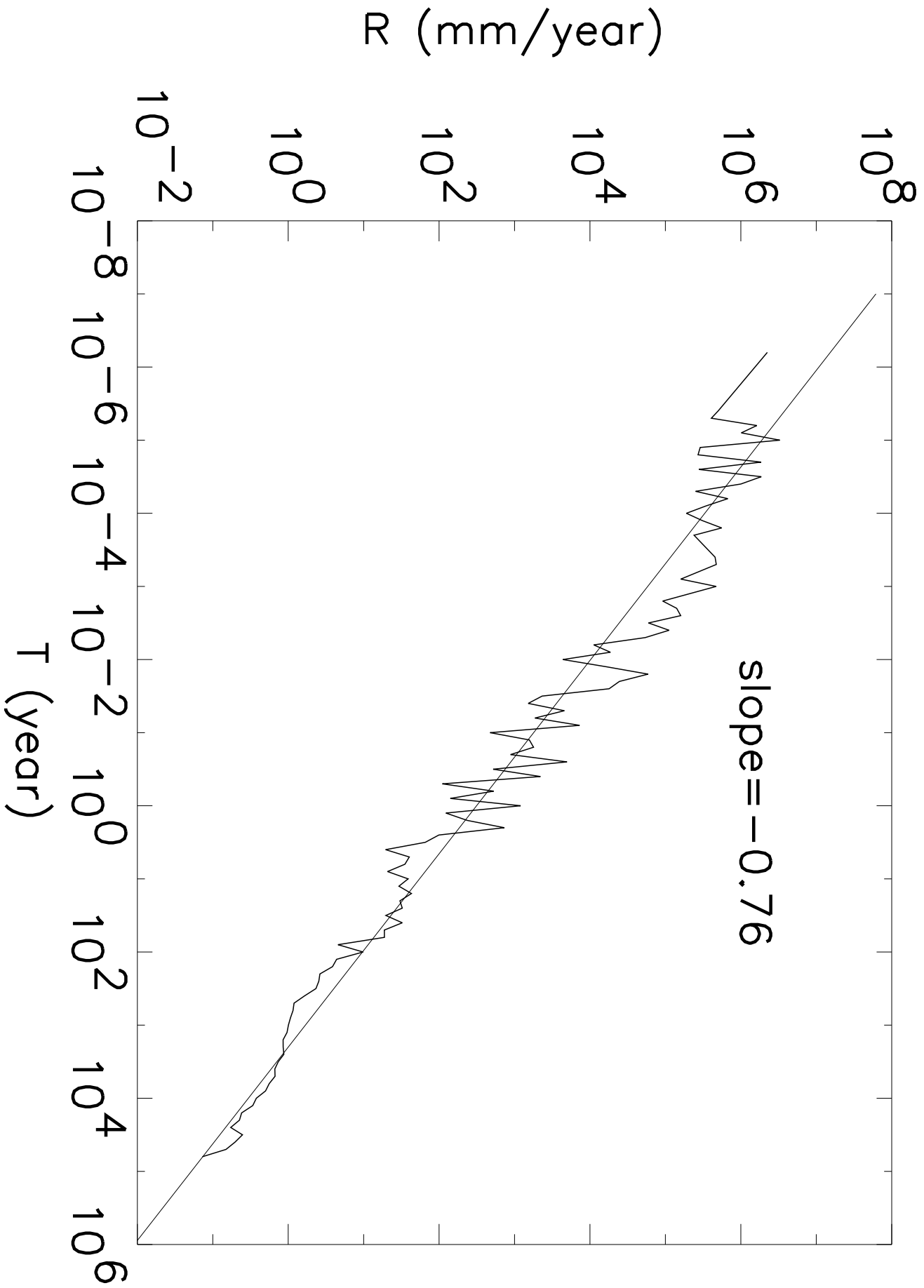




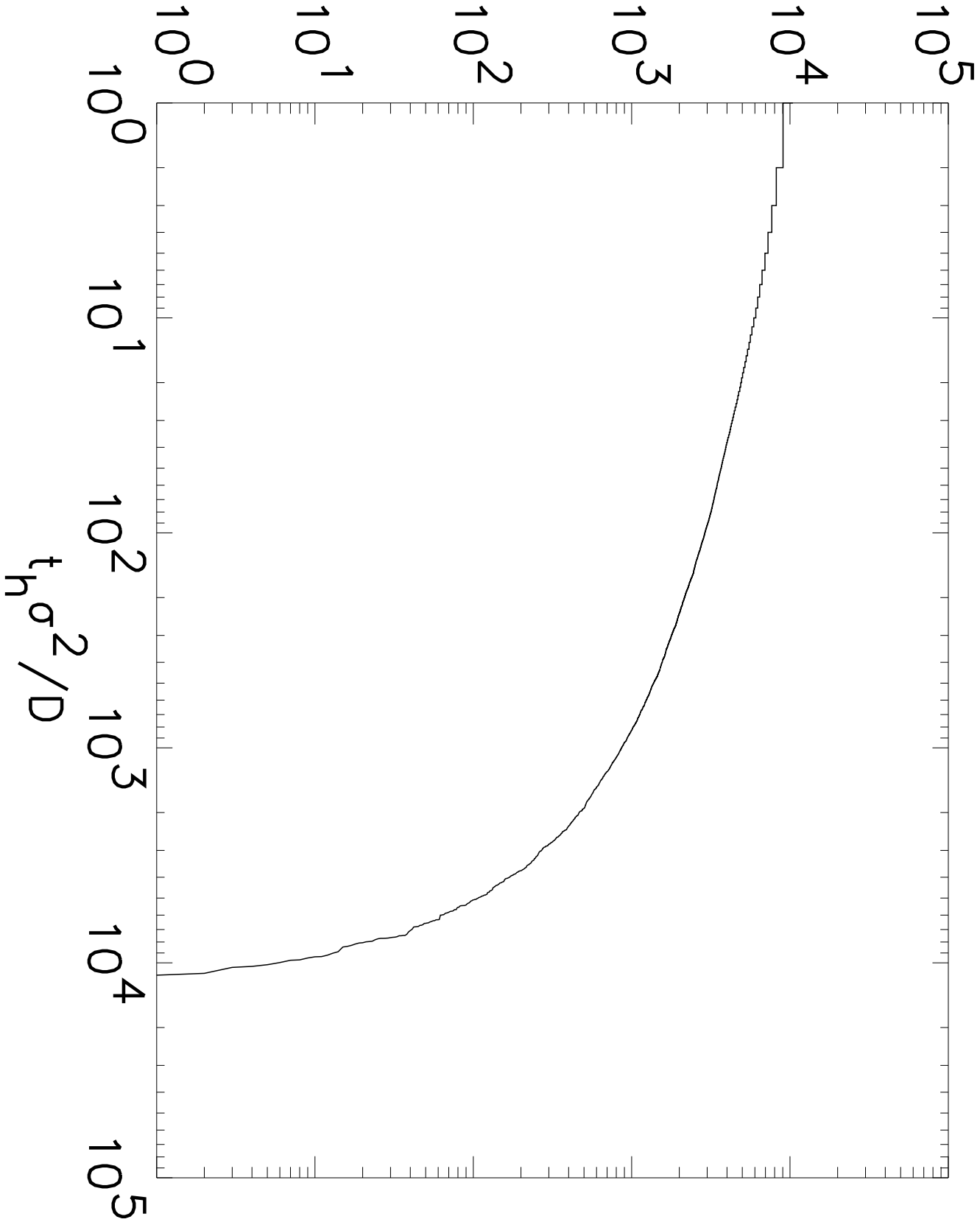
(b)

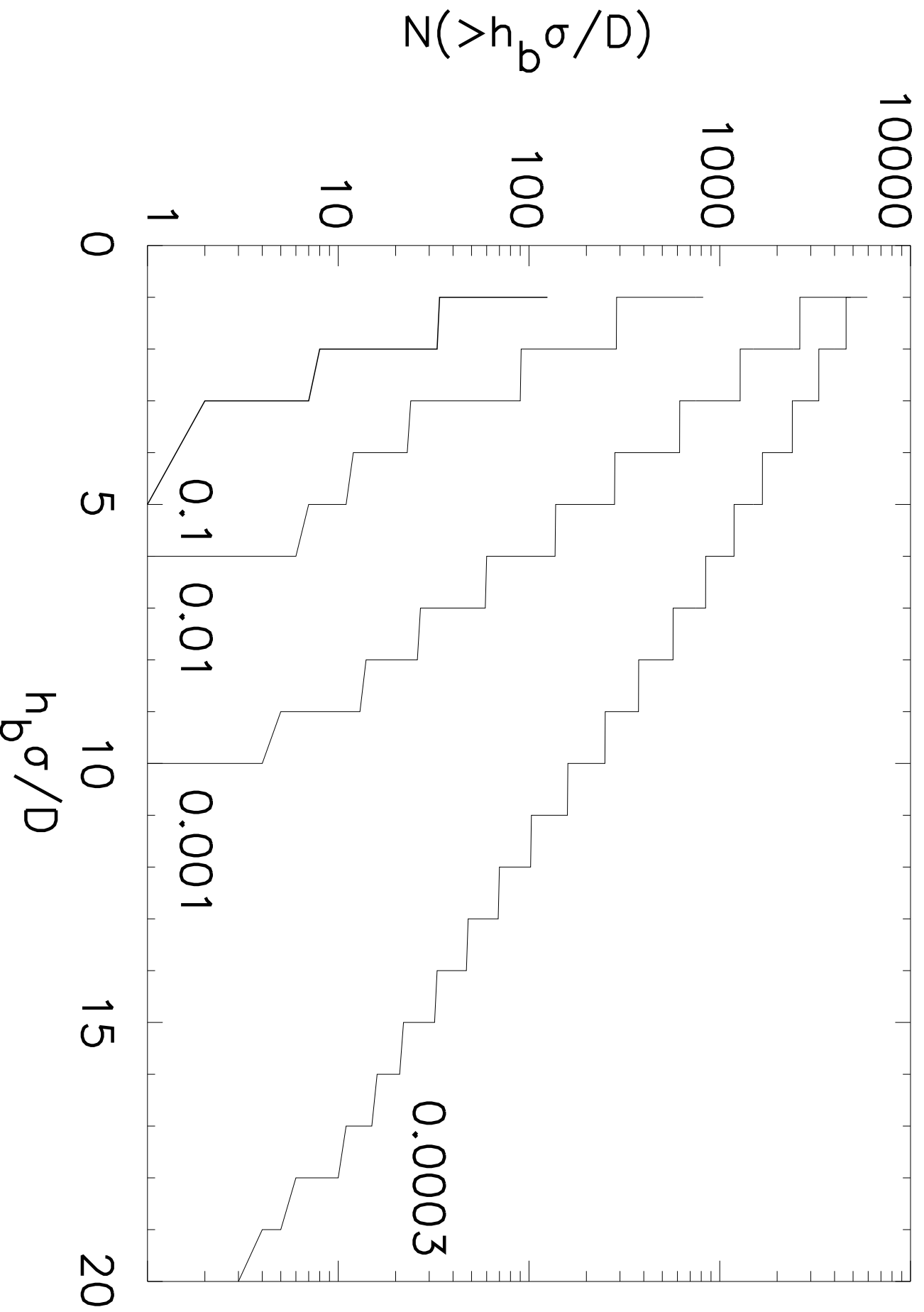
(c)

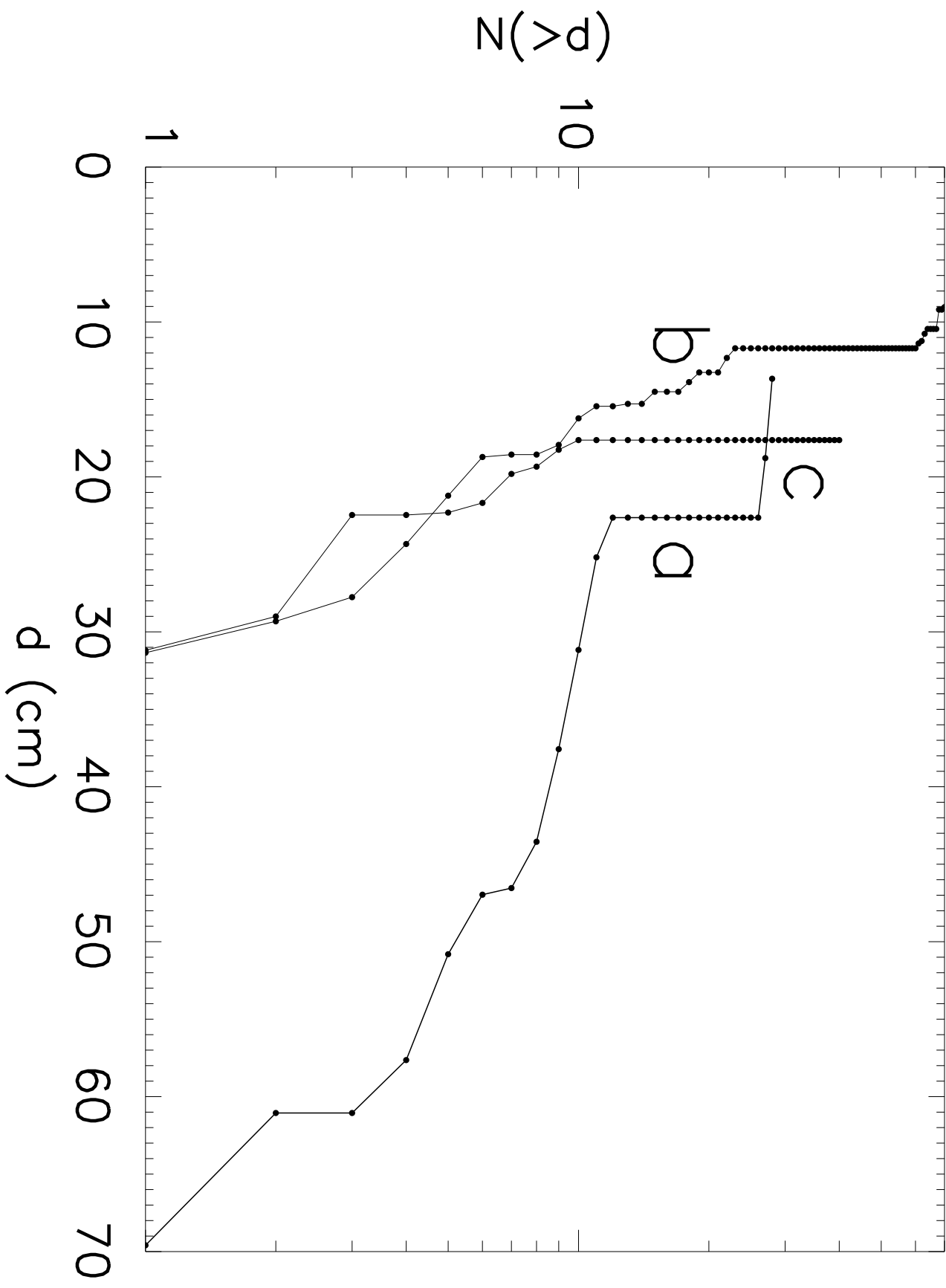




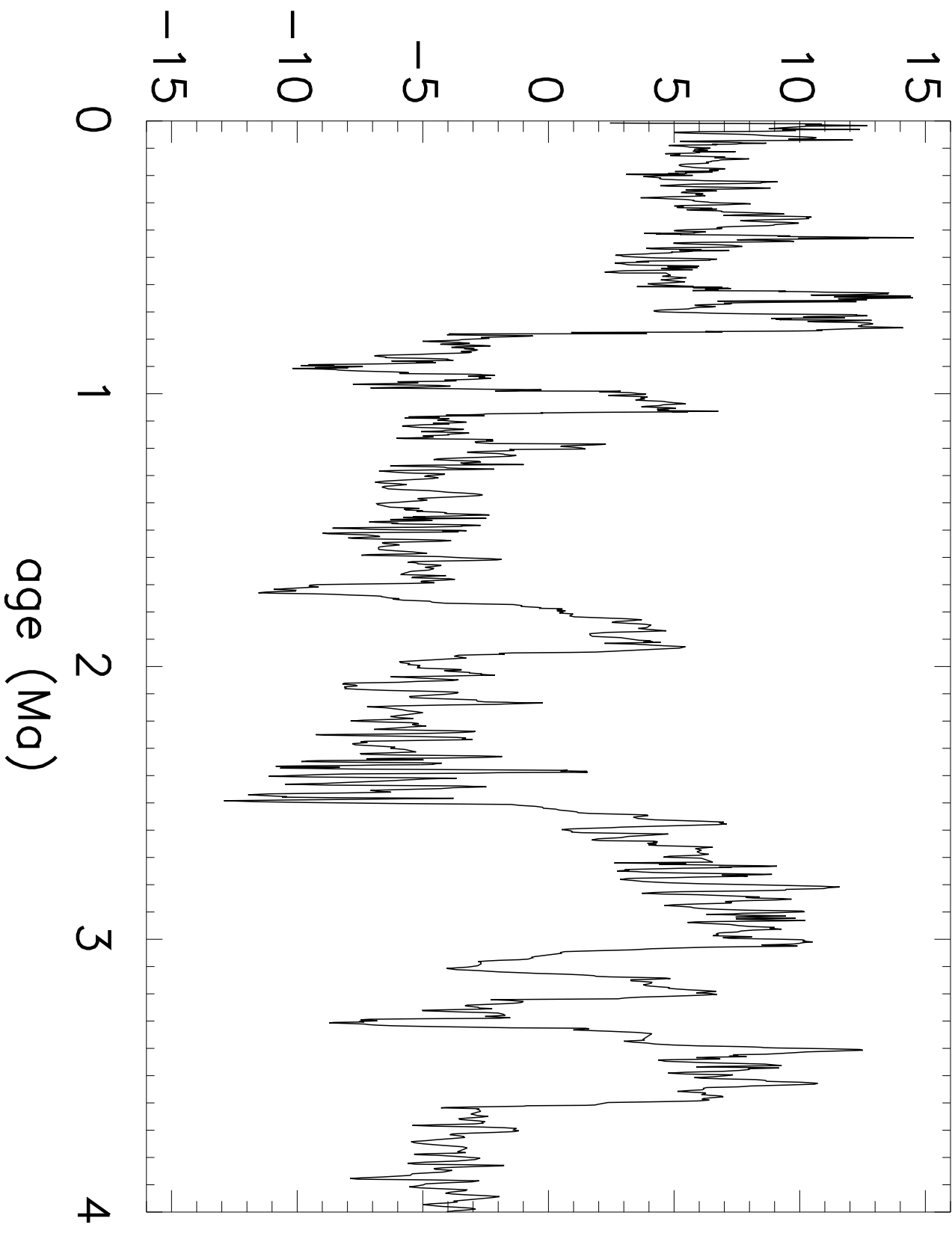
$N(>t_h\sigma^2/D)$

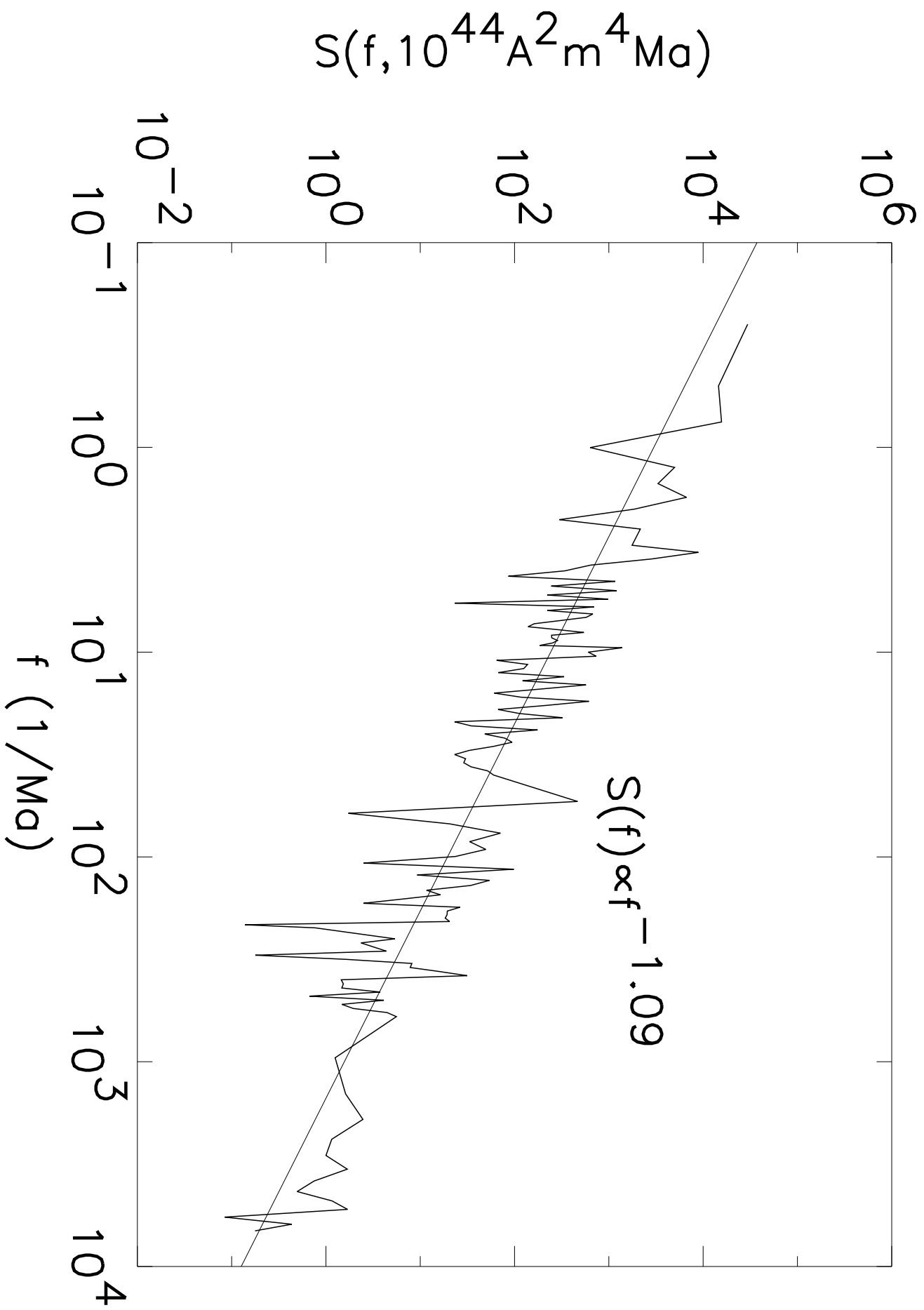




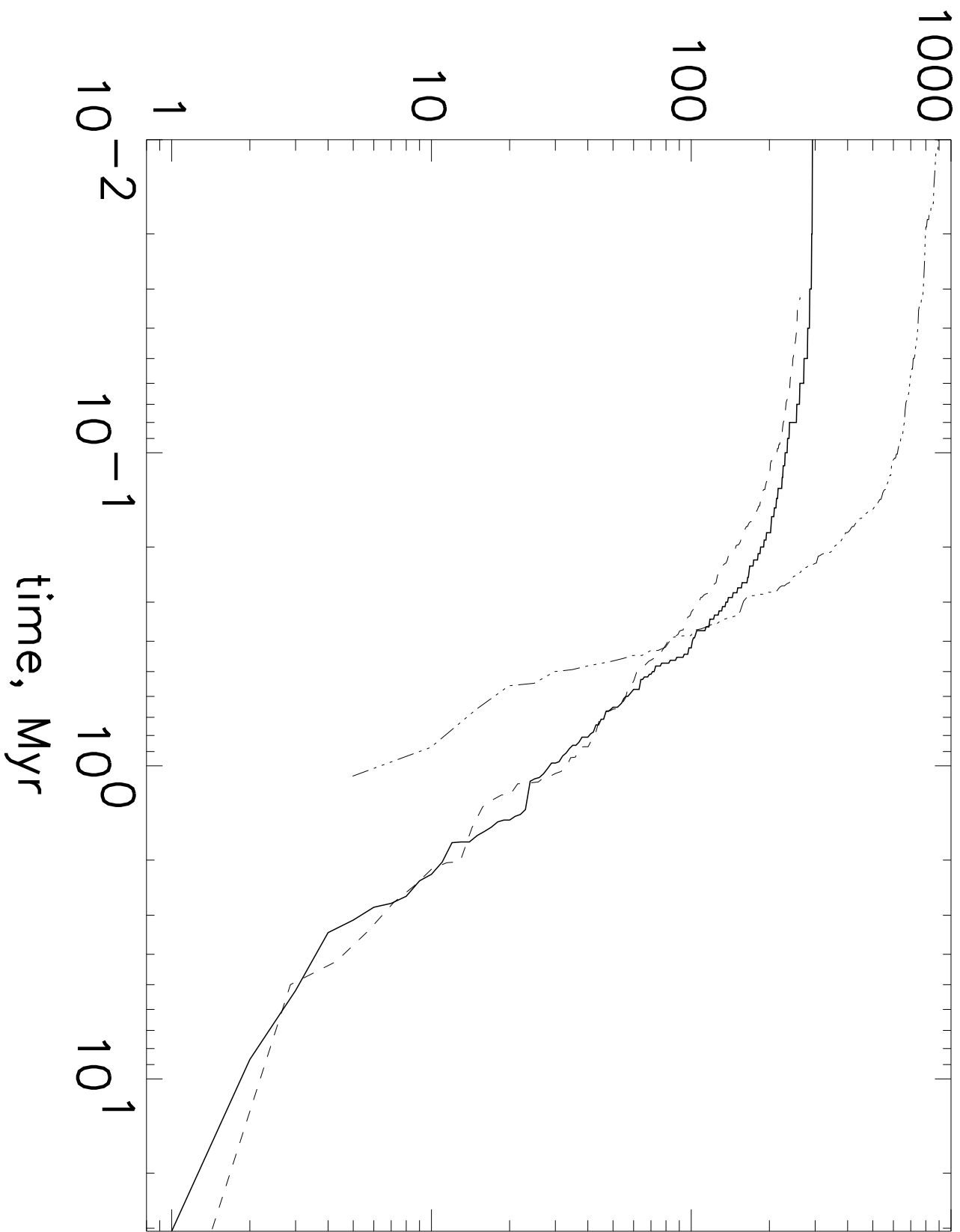


VADM (10^{22}Am^2)





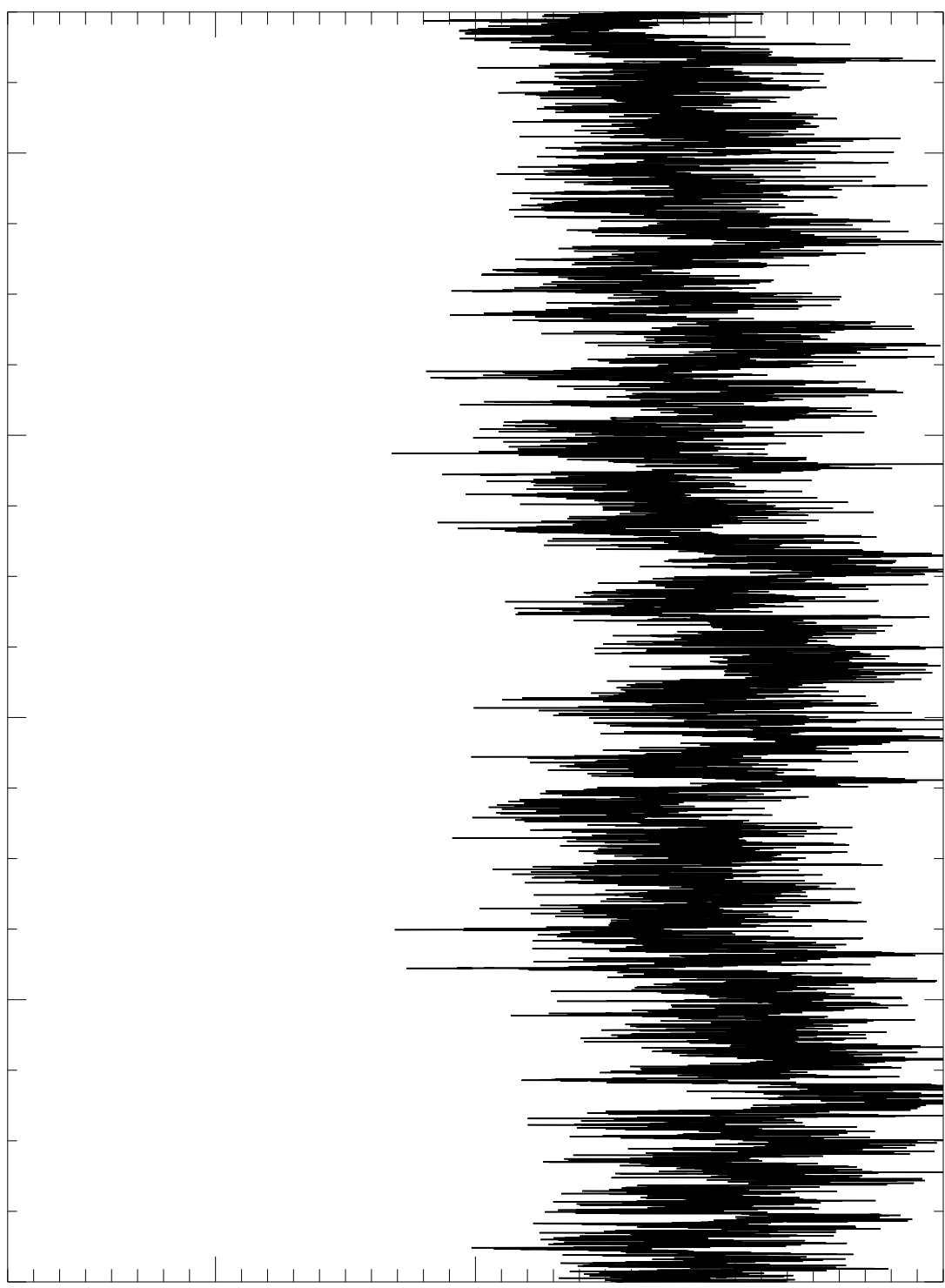
intervals > time



VADM (10^{22}Am^2)

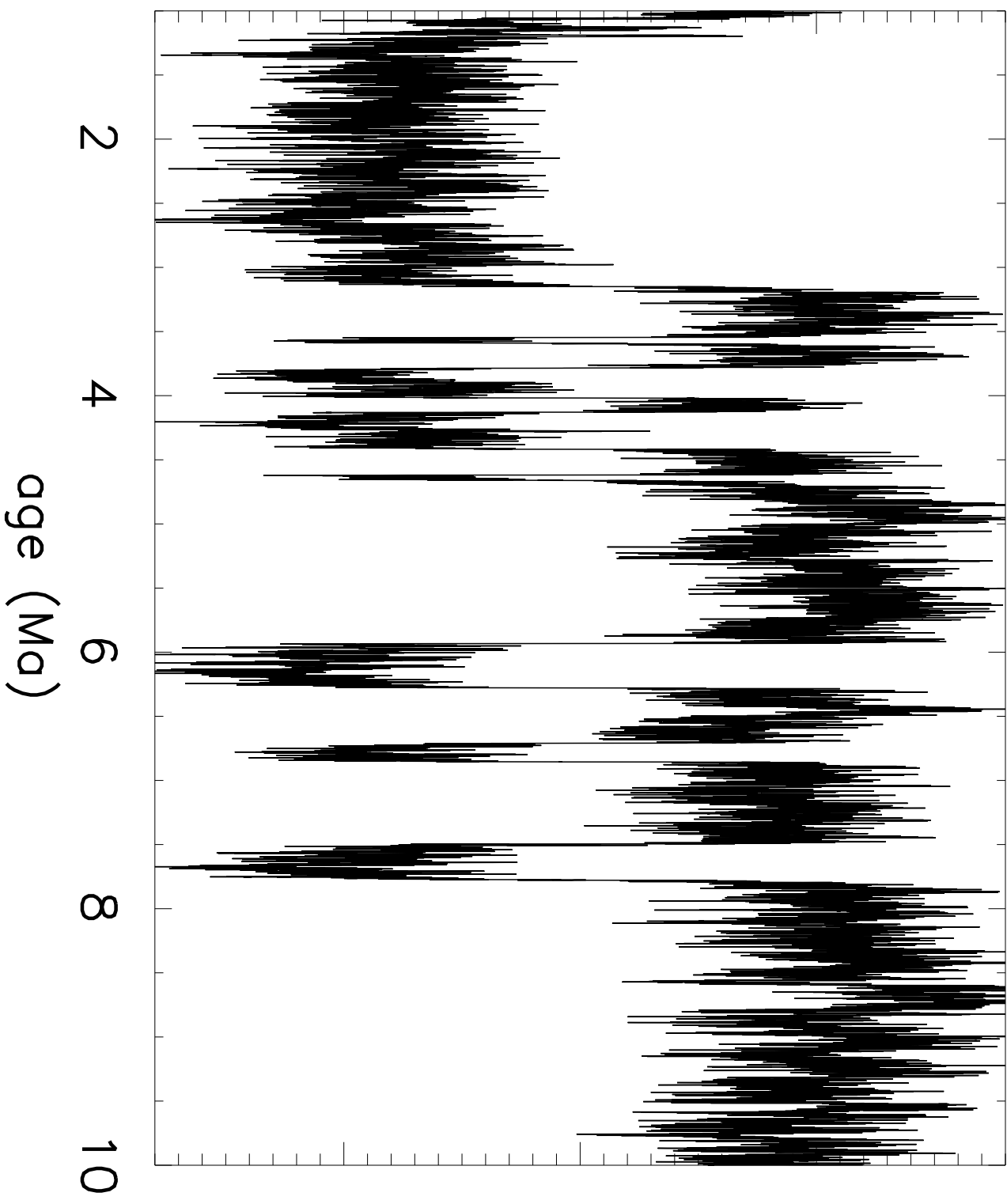
-10
0
10

2
4
6
8
10
age (Ma)

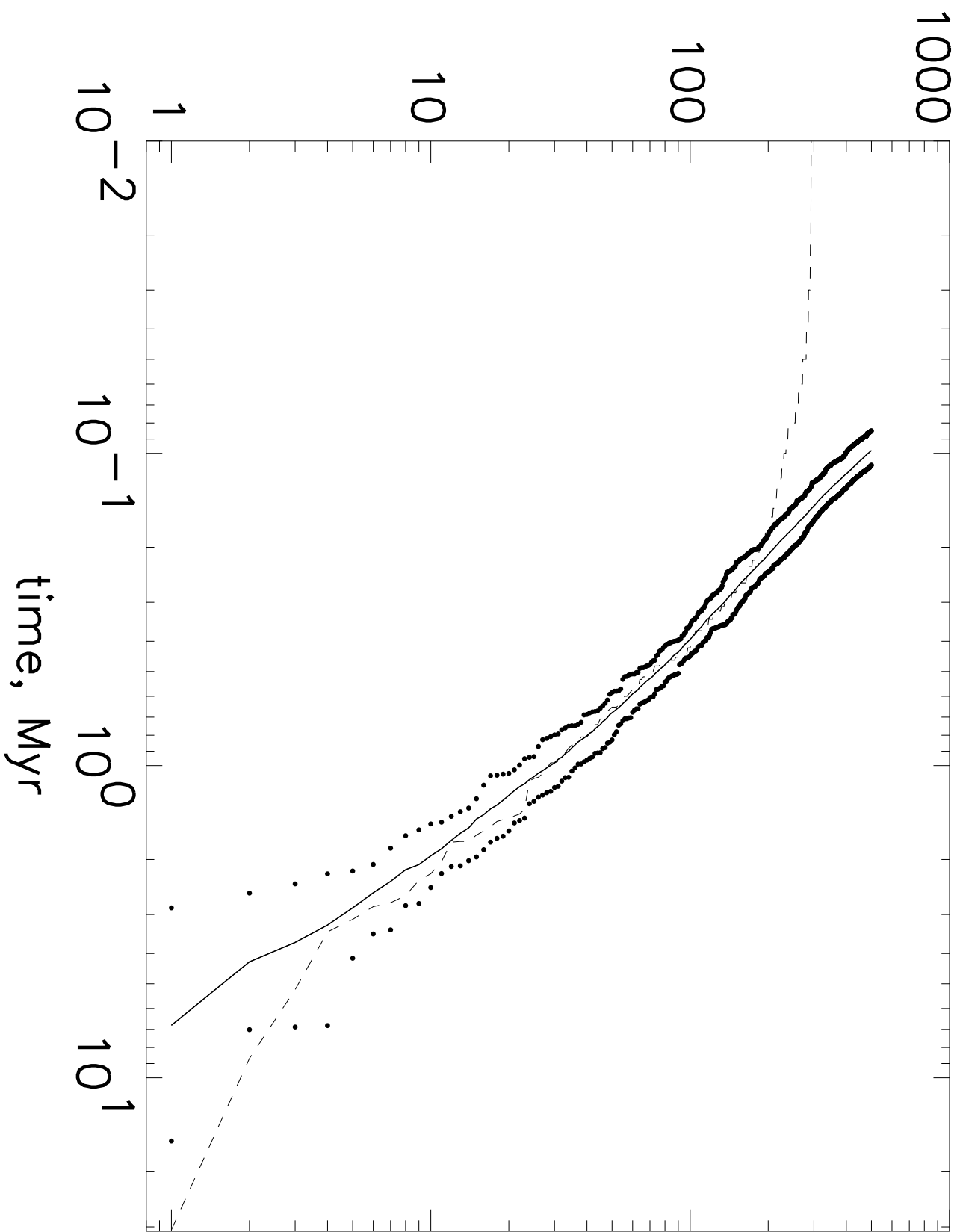


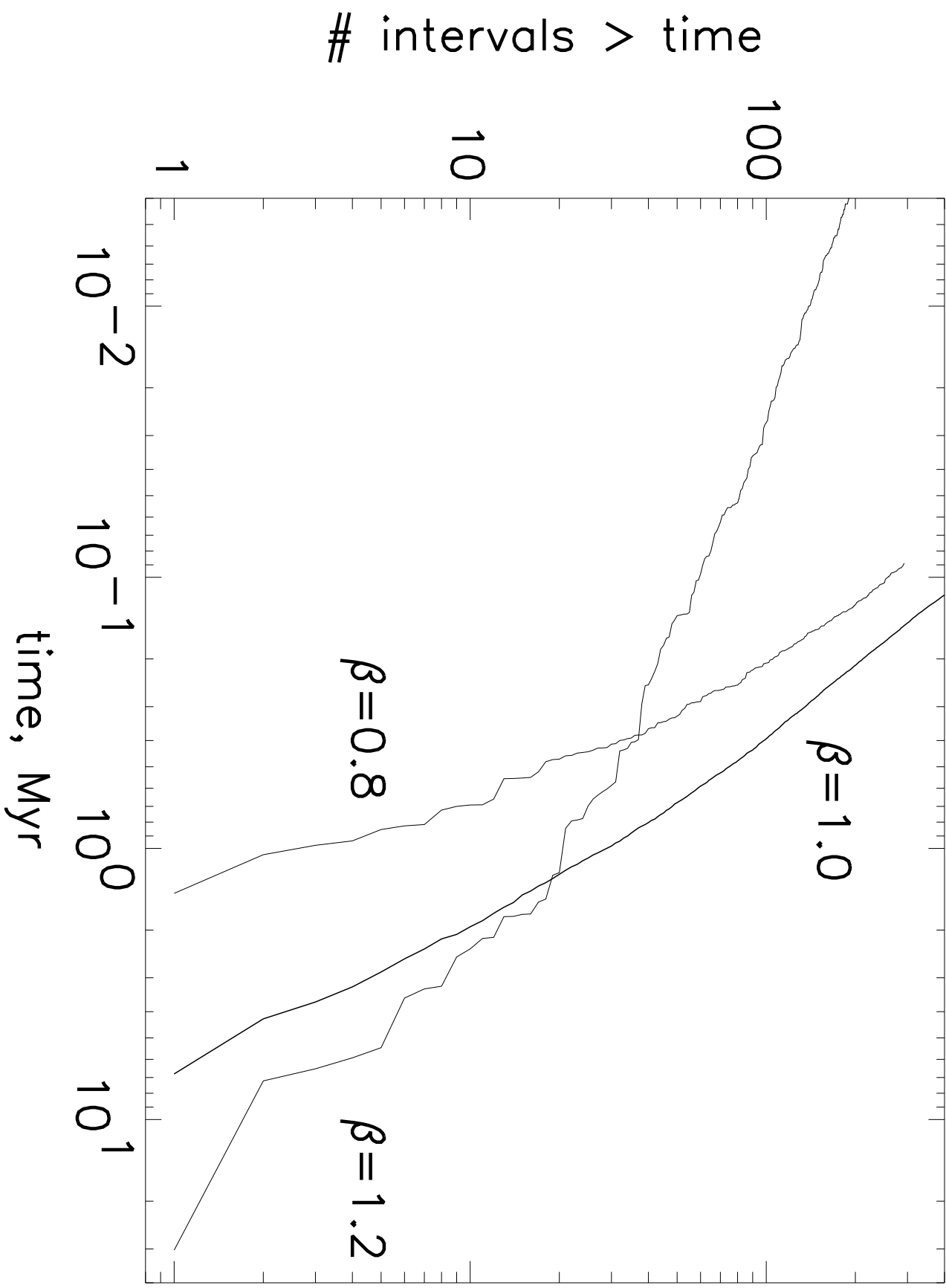
VADM (10^{22}Am^2)

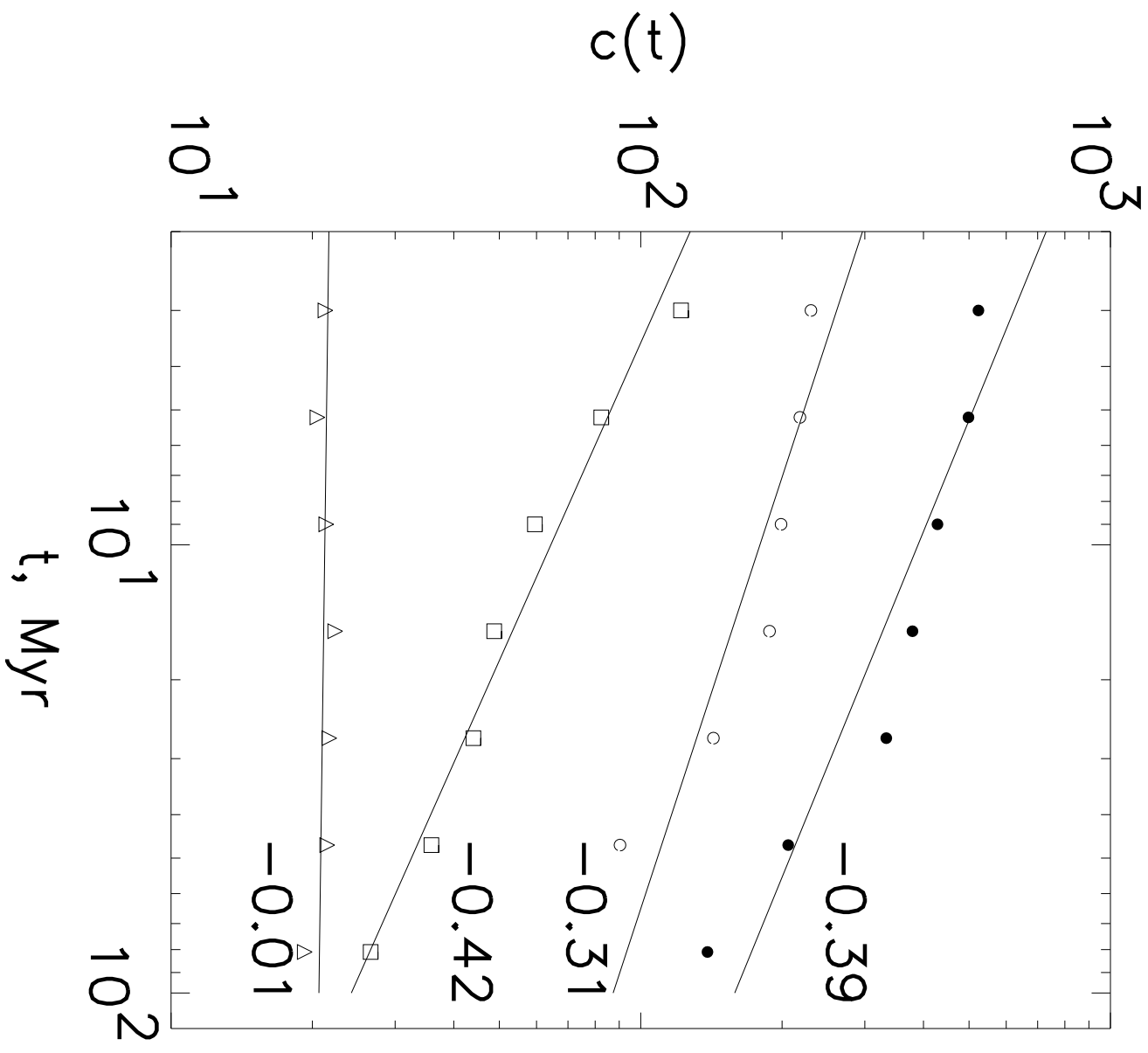
-10
0
10

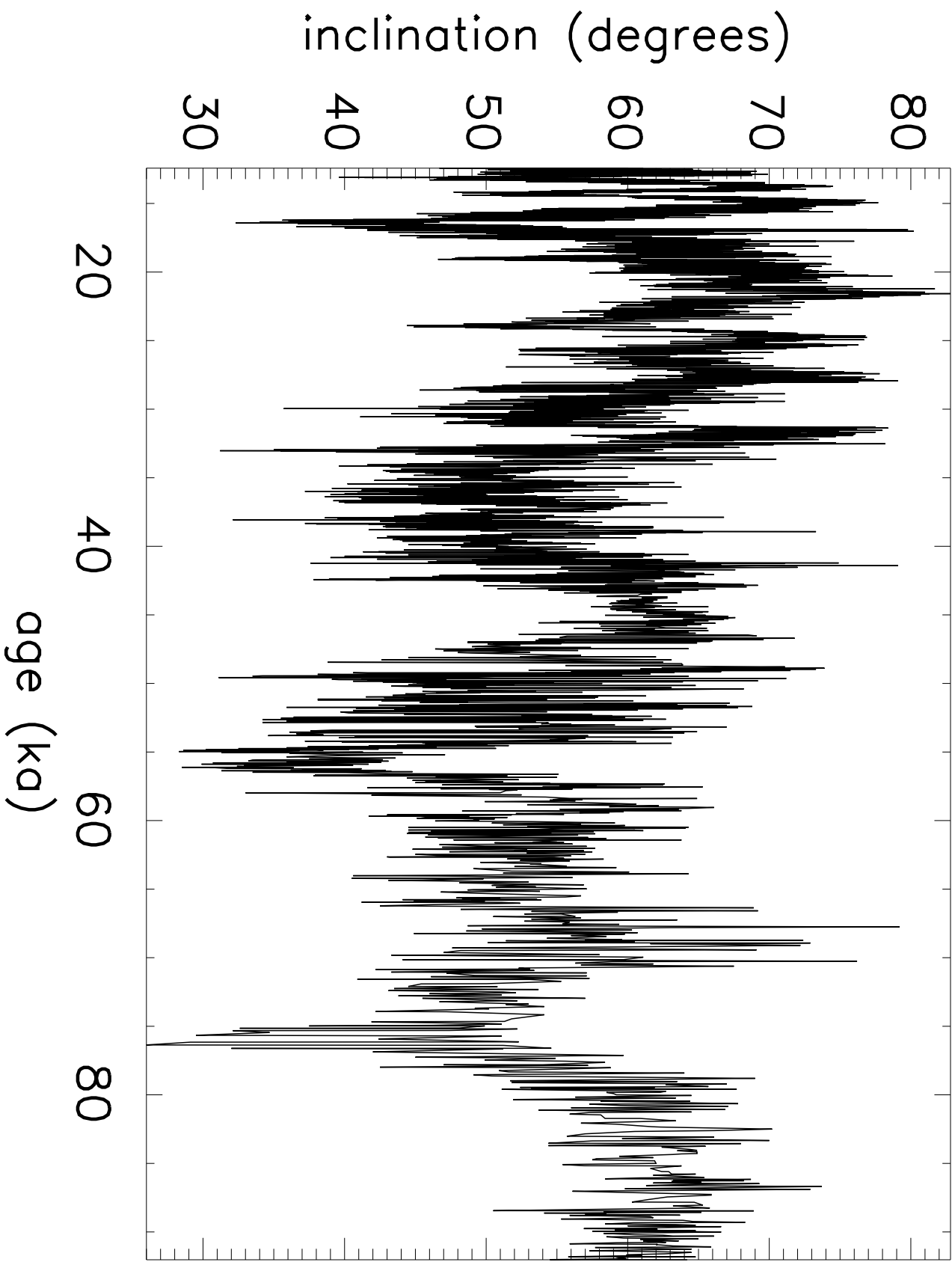


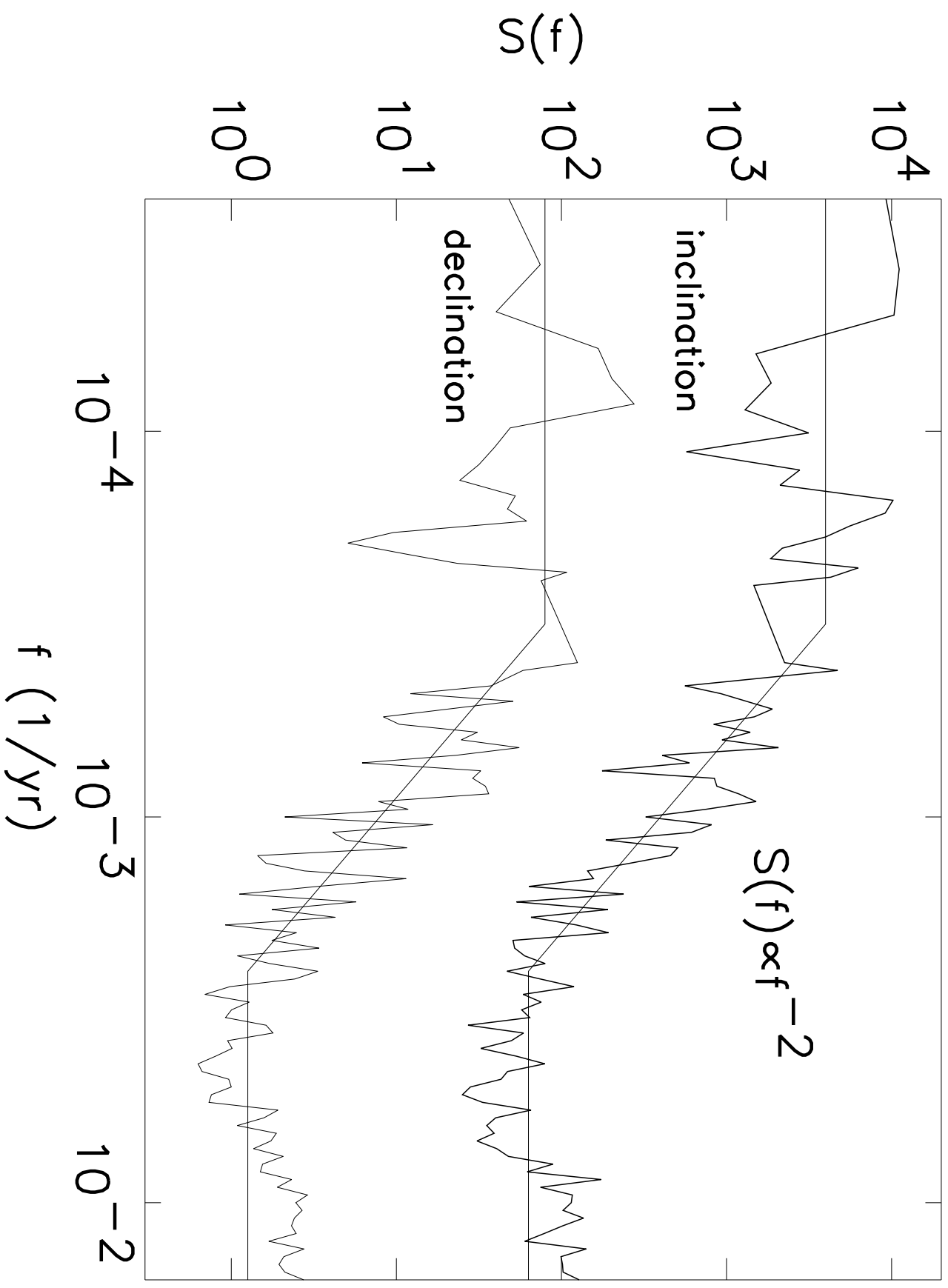
intervals > time

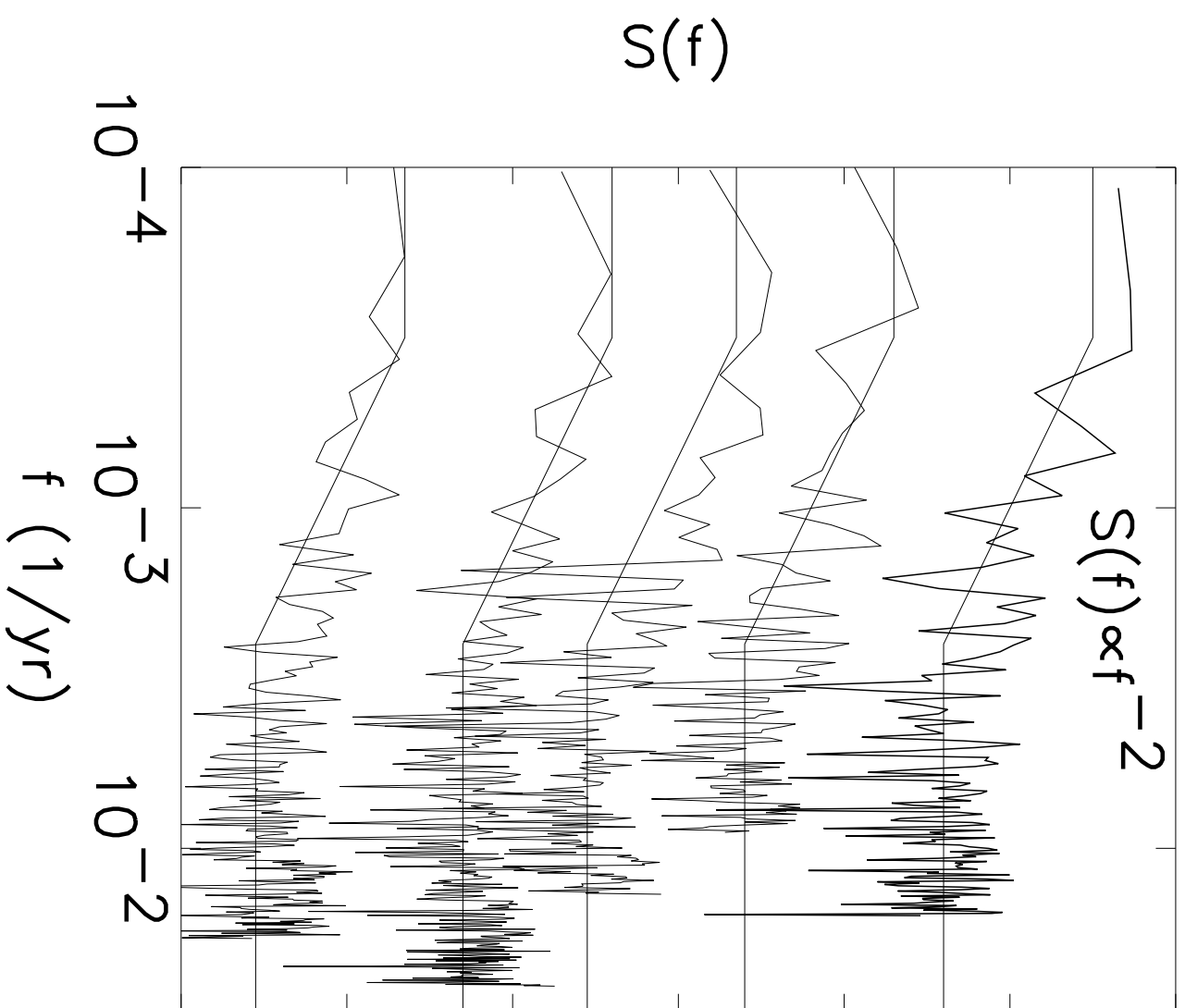


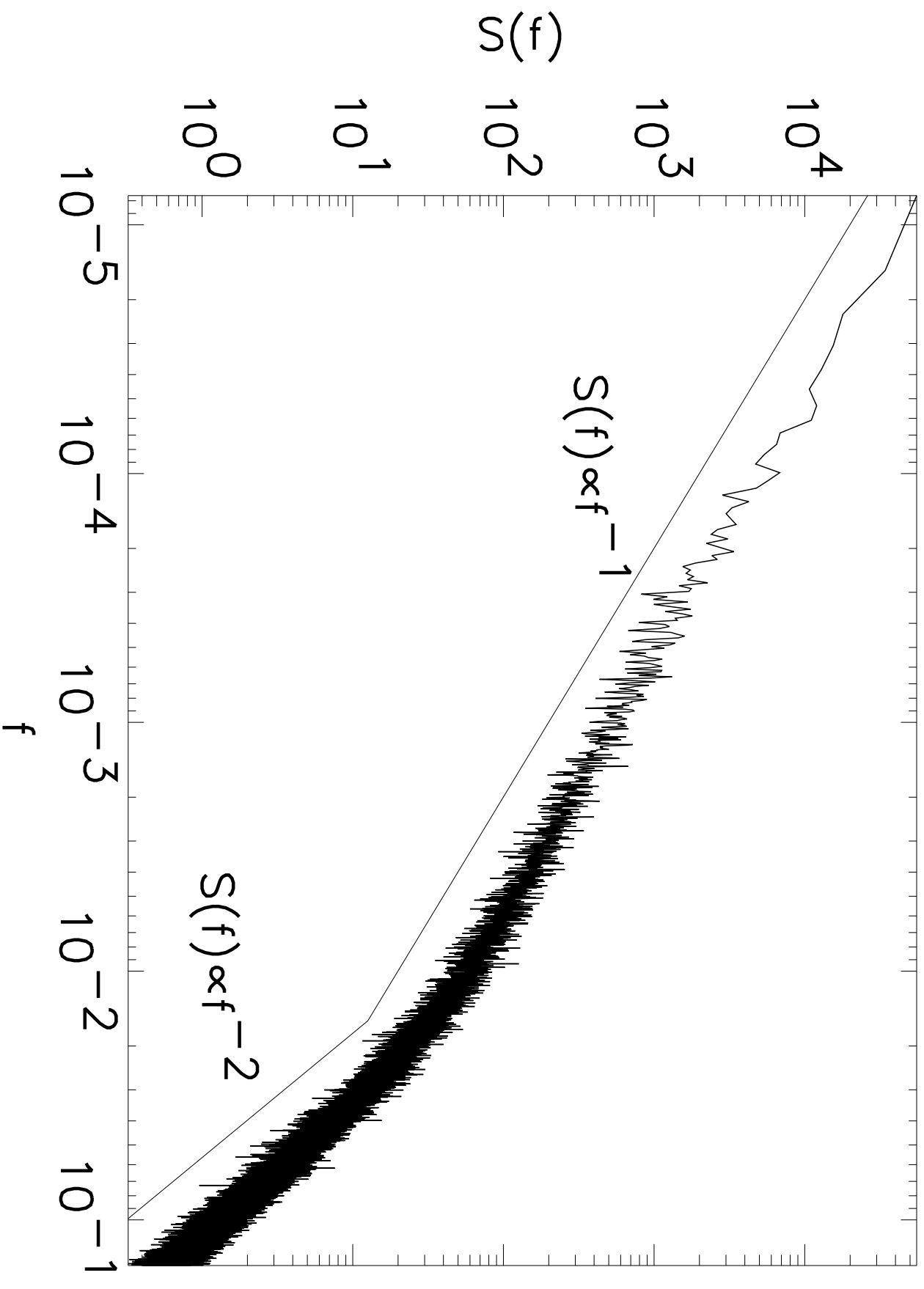












probability density function

